Circulation pathways, time scales, and water mass composition in the Arctic Ocean: Results from 25 years of tracer observations

Angelica Pasqualini

Submitted in partial fulfillment of the
requirements for the degree of
Doctor of Philosophy
under the Executive Committee
of the Graduate School of Arts and Sciences

COLUMBIA UNIVERSITY

2021

Abstract

Circulation pathways, time scales, and water mass composition in the Arctic Ocean: Results from 25 years of tracer observations

Angelica Pasqualini

The Arctic is a hotspot of global change. For example, changes caused by global warming are both amplified and are seen more rapidly in the Arctic (e.g., Serreze & Francis, 2006; Bekryaev et al., 2010; Serreze & Barry, 2011; Overland et al. 2015; Macdonald et al., 2015). Thus, the Arctic is an indicator of the state of the planet. Among the strongest changes that have been observed in the Arctic Ocean are changes in circulation regimes, hydrographic properties and freshwater content and composition. These changes have the potential of global impact through interaction with the deep-water formation regions of the North Atlantic Ocean, a major source of deep and bottom water in the global ocean. Although significant progress in understanding the signals of change in the Arctic Ocean and their causes has been made during the past decades there are still some fundamental questions unanswered. They include the stability of the circulation of the upper waters and changes in the freshwater budget and how these changes are connected to changes in the composition of the freshwater lens that covers the Arctic Ocean. In this thesis, we address these two topics using measurements of isotopes obtained during over three decades of Arctic Ocean section work.

This dissertation is composed by three parts and its structure mimics the layered vertical structure of the Arctic Ocean water column. Chapter 1 is dedicated to the Atlantic waters, Chapter 2 to the halocline waters, and Chapter 3 to the freshwater sources and their distribution and variability in the surface layer.

In the first two chapters, we present transient tracer ($^3H/^3He$) and hydrographic data from over 25 years of Arctic oceanographic campaign ranging from 1987 to 2013 to evaluate flow rates and circulation pathways in the Upper Halocline Water (UHW), Lower Halocline Water (LHW), and Atlantic Layer on a pan-Arctic scale. In agreement with previously established circulation schemes, tracer data show that the flow paths in the LHW and the Atlantic layer are typically topographically steered with the presence of a cyclonic boundary current along the continental shelf and separate circulation branches tracking major bathymetric features, such as the Lomonosov Ridge. Tracer data suggest that the general circulation of UHW is decoupled from the cyclonic regime observed in the deeper layer, and strongly influenced by surface stress forcing, such as the anticyclonic Beaufort Gyre. Within the limits of our method, tracer data show that the mean flow paths and spreading velocities have been more or less constant over the past three decades despite dramatic shifts in the Arctic system heat and freshwater balances from anthropogenic climate change over imposed to a high natural variability.

The third and final chapter discusses the water-mass composition and the distribution of freshwater sources in Canadian Basin, the western section of the Arctic Ocean. Results are produced by performing a water-mass decomposition on the water samples collected during the 2015 Arctic GEOTRACES (GN01) oceanographic expedition. Stable isotope measurements ($H_2{}^{18}O/H_2{}^{16}O$ and DHO/H_2O ratios) are used in combination with salinity and nutrients data to calculate the water-mass components for the upper 500 m Arctic Ocean (mixed layer through

Atlantic Water layer). The sources of liquid freshwater into the Arctic Ocean include Pacific water, sea ice meltwater, river discharge and net precipitation. The topmost 50 meters of Canadian Basin contain the large fraction of freshwater from sea ice meltwater and meteoric water. Pacific water dominated the freshwater budget along the 2015 GN01 transects from 100 to 250 m. These depths are also characterized by a strong brine rejection signal, reflecting an enhanced annual sea ice cycle with more ice refreezing and melting each year, and an overall loss of multiyear ice. The 2015 results are compared with the overlapping 1994 and 2005 Arctic Ocean Sections (AOS94 and AOS05) and discussed in the context of regional and temporal variability of liquid freshwater and its components distribution. Our findings show significant increases in the Canadian Basin total liquid freshwater reservoir both compared to the 1994 and 2005 transects confirming a freshwater accumulation in the Canadian Basin already established by numerous observations and modeling studies (Gilles et al., 2012; Carmack et al., 2016; Proshutinsky et al. 2019; Solomon et al., 2021). The total freshwater reservoir increased by ca. 12,500 km^3 from 1994 to 2015, of which ca. 5,000 km^3 are within the Beaufort Gyre. Meteoric and Pacific freshwater components were the largest sources of the observed freshwater accumulation in the upper 500m of the western Arctic Ocean. An intensified Ekman transport in the Beaufort Gyre and increased availability of freshwater for accumulation are the two primary drivers for freshwater accumulation in the Canadian Basin. Within the limits of our analysis, it is not possible to quantitatively estimate the relative importance of the each forcing nor to resolve the seasonal to year-to-year variability.

Table of Contents

List of Charts, Graphs, Illustrations

Acknowledgments

This project would not have been possible without the data set of tritium and helium isotope measurements produced by the Lamont-Doherty Earth Observatory Environmental Tracer Group during over three decades under the supervision of Peter Schlosser. I am particularly grateful to Charles (Chucky) McNally, Ronny Friedrich, Antony Dachille, Richard Perry, Dale Chayes, and Tobias Koffman for their contributions to the collection and analysis of the data described in this study. I thank Bob Newton for providing invaluable guidance and encouragement throughout my research, and for his help in implementing the water mass deconvolution model. I thank Bill Smethie for innumerable constructive comments and insights. I am thankful to Debbie Criscione, Jennifer Holland, and Elizabeth Allende who have been instrumental in getting my thesis to completion.

Most of all I will always be fully indebted to Peter Schlosser, my dissertation advisor, for his wisdom, vision, enthusiasm, and for pushing me to reach further than I thought I could go.

Funding for my dissertation were provided by grants from the U.S. National Science Foundation (PLR 15-04404 and OCE-1436666) awarded to P. Schlosser, R. Newton, and W. M. Jr. Smethie.

Dedication

To my research group. To Stuart. To Ellen. To Jade.

Chapter 1: Circulation pathways and spreading rates of the Atlantic Waters in the Arctic Ocean derived from three decades of Tritium/^{3}He observations

1.1 Introduction

The Arctic Ocean, which is the Earth's smallest ocean containing 3% of the total ocean area and accounting for only 1% in volume, is unique on local, regional and global scales due to its relatively high freshwater content and its perennial sea ice cover. In particular, the freshwater fluxes from the Arctic Ocean to lower latitude oceans influence the preconditioning of surface waters in the deep-water formation regions of the Greenland, Norwegian, and Icelandic seas, as well as in the North Atlantic (primarily the Labrador and Irminger Seas). Thus, understanding the basic water mass structure, circulation patterns, and rates of exchange of waters through Fram Strait, Bering Strait and the Canadian Archipelago are of fundamental importance.

Due to its harsh environmental conditions resulting in much sparser data coverage compared to the low latitude oceans, the Arctic Ocean is still not as well understood as the low- and mid-latitude oceans. At the same time the Arctic Ocean is more vulnerable to global change. The observed warming rate of the Arctic air temperature has been consistently more than double the rate of the global mean: between 0.1°C and 0.3°C per decade for the period between 1984 and 2012 (e.g., Serreze et al., 2009; Meredith et al., 2019). The enhanced rate of temperature increase experienced in the Arctic, a phenomenon referred to as Arctic Amplification, is of particular interest as the Arctic Ocean can respond rapidly to changes in atmospheric conditions (Serreze et al., 2000; 2011; Polyakov et al., 2002).

As a consequence of environmental change, the hydrography of the Arctic Ocean has changed significantly during recent decades (Morison et al., 2000; Murray et al., 2010; Morison et al., 2012). The most dramatic changes are found in the mixed layer, the halocline, and the Atlantic Water (AW) which, taken together, cover the upper ca. 500 meters of the Arctic Ocean, and include modifications in water mass properties, freshwater content and composition, and location of fronts such as that between the Eurasian and Canadian domains of the Arctic Ocean (Steele et al., 1995; 2004; Serreze et al., 2000; 2003; 2007). For example, during the past two decades a notable temperature increase has been observed in the AW layer and the stratification in halocline has weakened (Quadfasel et al., 1991; Polyakov et al., 2005; Polyakov et al., 2012). It has also been reported that the temperature along some branches of the circulation has relaxed back towards earlier climatology (e.g., Morison et al., 2000; Morison et al., 2012).

As a consequence of the warming Arctic sea ice mass has progressively turned younger, more unstable, and thinner. Since satellite monitoring began in 1979, Arctic sea ice extent (area of ocean where ice concentration is at least 15%) declined by 40%, with the more pronounced loss observed at the end of the melting season (late summer) (Overpeck et al., (2005); Mahlstein & Knutti, (2012); Stroeve et al., 2014). Mean sea ice thickness decreased from ca. 3m to ca. 1.5m accounting for a 75% decline in arctic summer sea ice volume since the 1970s (Kwok & Rothrock, 2009). Generally older ice is thicker, brighter, and more resilient to summer melt than first-year ice. In March 2019 multiyear ice (>4 years old) accounted for less than 2% of the Arctic Ocean ice pack and first-year ice for approximately 70%; compared to 33% and 35-50% as measured in 1985 (Perovich et al., 2019). The dominance of seasonal sea ice raises the likelihood of ice-free summer (Stroeve et al., 2014). The observed decline in minimum sea ice extent has been accompanied by changes in the thermohaline structure of the Arctic Ocean

including a warmer and shallower Atlantic core Layer and a weaker stratification across the halocline in the Eurasian Basin (Polyakov et al., 2010; Polyakov et al., 2017). Model results indicate that these changes in the water column structure alone can account for an increase in the upward heat transfer of the AW through the Eurasian Basin halocline of 0.5–1.0 Wm^{-2}, over an annual average O(1-2) W m^{-2}, (data from 1990s relative to the 1970s) further enhancing the sea ice loss (ca. 30 cm in 50 years, 1 Wm^{-2} is equivalent to 10 cm of ice loss) (Polyakov et al., 2010; Polyakov et al., 2013). Winter AW upward heat fluxes are 3 to 4 times larger than the annual average and have a direct impact of local sea ice formation/growth. Changes in the eastern Eurasian Basin stratification can lead to a deeper winter ventilation, enhanced seasonal release of oceanic heat, and reduced ice growth. Polyakov et al. (2017) found a 2- to 4-fold increase in the winter upward AW heat flux since 2007/2008.

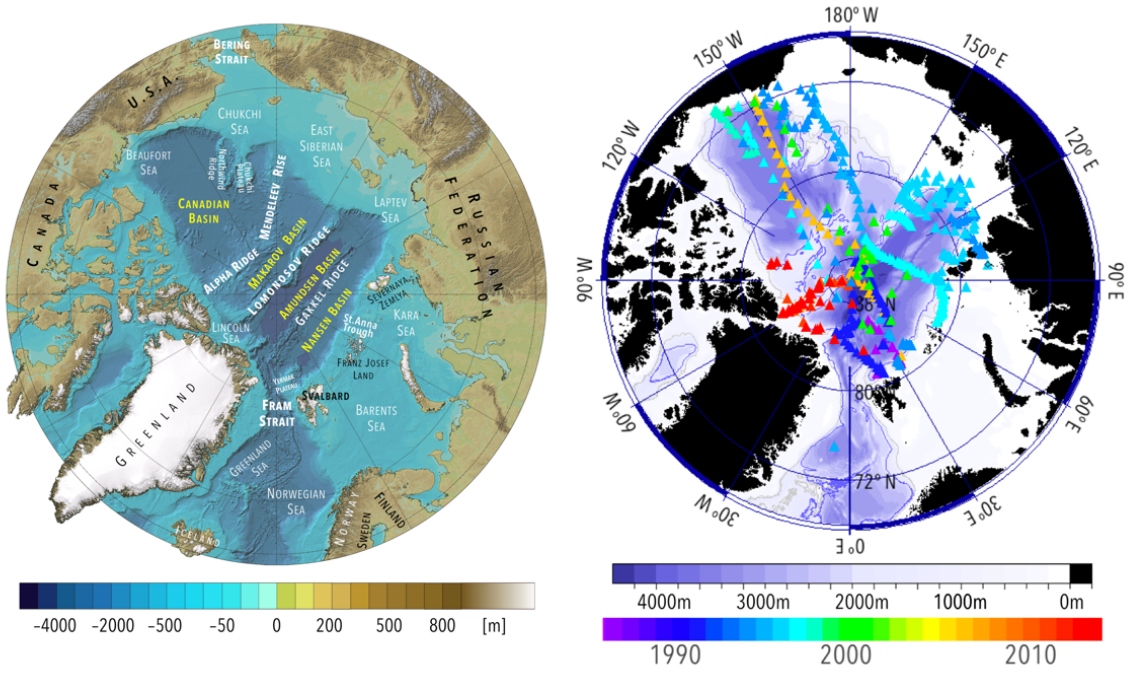

Figure 1: Left panel: Arctic Ocean map showing the main seafloor features and geographical locations of the studied areas. Modified from Geology.com. Right panel: geographical location of the hydrograhic stations occupied between 1987 and 2013 and used in this study. The colors correspond to the sample year.

The pace of observed changes in the Arctic Ocean water mass properties, distribution, and circulation as part of pan-Arctic system-scale environmental change adds urgency to improving our understanding of the fundamental impacts of the AW on the Arctic Ocean circulation and its impact on the sea ice cover through upward heat flux (Serreze et al., 2000; Serreze et al., 2007; Polyakov et al., 2017; 2020).

Mauldin et al. (2010) used transient tracer data ($^3H/^3He$ and CFCs) and a leaky pipe model (Spall, 2013) to estimate the mean spreading rates and mixing time scales of the Barents Sea Branch Water (BSBW) along two of its circulation branches, from the St. Anna Trough to the southern Canada Basin. Here, we expand that study to both branches of the Atlantic water, Fram Strait Branch Water (FSBW) and BSBW, and geographically to the entire Arctic Ocean. To this end, we use a data set of tritium and helium isotope ($^3H/^3He$) measurements collected during 21 Arctic Ocean cruises between 1987 and 2013 to delineate the spreading patterns and average spreading velocity of FSBW and BSBW, as well as the long-term stability of the AW circulation patterns.

1.2 Hydrology

The Arctic Ocean is nearly completely enclosed by the continental shelves of Eurasia, North America and Greenland. Large estuaries and shallow (<300m) marginal shelf seas occupy its boundaries to the south, covering more than 1/3 of the Arctic Ocean surface. The major Arctic shelf seas are the Barents Sea, the Kara Sea, and the Laptev Sea in the Eurasian Basin, and the East Siberian Sea, the Chukchi Sea, and the Lincoln Sea in the Canadian Basin. The Arctic Ocean connects with the northern Atlantic Ocean via Fram Strait and the Barents Sea, and the Pacific Ocean via the Bering Strait (Coachman et al., 1963; Stigebrandt, 1984; Rudels et al., 1994). Approximately 11% of the global estuarine discharge inflows into the Arctic Ocean from

North America, Mackenzie and Yukon, and Siberia, Ob, Yenisey, and Lena (McClelland et al., 2012).

Water masses in the upper 1200 m of the Arctic Ocean are mainly of Atlantic origin (Rudels, 2009). The Arctic Ocean is supplied by Atlantic water (AW) along two pathways: Fram Strait and the St. Anna Trough. The former carries the warm and saline FSBW, and the latter BSBW. FSBW enters the Arctic Ocean north of Svalbard. At the point of entry into the Arctic Ocean, FSBW has a core depth of 200m and 500m, a mean temperature of 3ºC, and an average salinity of 34.96 (Schauer et al., 1997). The BSBW reaches the Arctic Ocean between Fran Josef Land and the Severnaya Zemlya archipelago at depths between 600–1200m with temperatures between 0–2ºC and salinities between 34.86–34.91 (Schauer et al., 1997). The two-branch hypothesis was initially proposed by Rudels et al. (1994) and further elaborated on by other studies (e.g., Schauer et al., 1997; McLaughlin et al., 2002; Rudels et al., 2013).

The flow structure and transport across Fram Strait are complex and involve local recirculation, large seasonal variability, and strong current shear between the West Spitsbergen Current and the East Greenland Current (Mauritzen et al., 2011; Beszczynska-Möller et al., 2012; Marnela et al., 2013; de Steur et al., 2014). The mean northward transport of AW in the West Spitsbergen Current ranges from 2 to 5 Sv (Beszczynska-Möller et al., 2012; Mauritzen et al. 2011). Roughly half of this AW recirculates within Fram Strait and flows southward as a component of the East Greenland Current (Schauer et al., 2004; Marnela et al., 2013). The remaining AW, (3.0 ± 0.2 Sv), continues north through Fram Strait Branch and flows eastward along the continental slope as FSBW (Beszczynska-Möller et al., 2012). The average BSBW inflow into the Nansen Basin ranges from 1.3 to 2 Sv (Smedsrud et al., 2010; Skagseth et al., 2011).

Since the opening of the Bering Strait at the end of the last ice age, Pacific water has passed through the Arctic into the north Atlantic. A constant steric height gradient between the Bering Sea and the Canadian Basin drives a Pacific inflow of 0.7–1.1 Sv into the Arctic Ocean through Bering Strait (Woodgate et al., 2012).

Outflows from the Arctic basins are all towards the Atlantic Ocean; PW primarily exits via the Canadian Arctic Archipelago (ca.1–2 Sv) (Münchow et al., 2007) and modified and recirculated AW via Fram Strait (ca. 4.1 ± 0.8 Sv measured at 78.83ºN) (de Steur et al., 2014). About 1.5 to 2.2 Sv of this flux is contributed by recirculated AW (Mauritzen et al., 2011; de Steur et al., 2014).

The Arctic Ocean receives on average 0.3 ± 0.02 Sv of freshwater annually (relative to a salinity of 34.8; mean based on the period between 2000 and 2010) (Haine et al., 2015). Although volumetrically small, this input is a determinant factor in the upper water column stratification, thus constraining the heat flux from the AW into the mixed layer and sea ice cover (e.g., Polyakov et al., 2017; Schauer & Beszczynska-Möller, 2009). River runoff is the largest freshwater component, accounting for approximately 45 ± 10% (0.13 ± 0.01 Sv); Pacific waters add annually ca. 0.08 +-0.003 Sv, or 28 ± 4% of the total freshwater input; and net precipitation accounts for 23 ± 10% of the annual flux (0.07 ± 0.01 Sv) (Haine et al., 2015). The seasonal sea ice cycle of freezing and melting also affects the freshwater budget, essentially separating seawater into its freshwater and brine (Aagaard et al., 1989; Carmack et al., 2016).

Density stratification in the Arctic Ocean water column is almost solely a function of salinity and the strongest density gradients are observed in the surface and halocline layers (upper 150-200m). A well-mixed surface layer of cold and fresh water occupies the uppermost part of the Arctic Ocean. This buoyant layer contains a large fraction of the freshwater anomaly

content in the water column. It varies seasonally from less than 10 to several tens of meters thickness and closely interacts with wind and the sea ice cover. Typically, the polar mixed layer is 5 to 10 meters thick in ice-covered regions and near river outflows in summer, and twice as deep in ice-free regions where the wind-driven mixing is stronger. In the fall sea-ice formation releases brine that can cause overturning down to 40 or 50 meters depth. The surface water has four principal components: meteoric water, sea ice melt-water, relatively fresh Pacific water, and relatively salty Atlantic water (e.g., Ekwurzel et al., 2001; Newton et al., 2008).

Below the mixed layer a steep halocline separates the warm Atlantic Water from the surface. Arctic halocline waters typically can be divided into upper halocline waters (UHW) and lower halocline waters (LHW) and show significant spatial and temporal (seasonal and inter-annual) variability. Different processes are responsible for maintaining this strongly stratified layer in the eastern and western Arctic basins. The UHW is of Pacific origin is primarily constrained to the Canadian Basin sometimes extending into the Amundsen Basin at depths between 60 and 220 m (Steele et al., 2004; Bluhm et al., 2015). LHW waters derive from the North Atlantic (Rudels et al., 2004).

UHW is characterized by salinities around 33.1, near-freezing temperatures, and marked nutrient maxima associated with the Pacific inflow and nutrient regeneration over the Chukchi Shelf (Jones & Anderson, 1986; Anderson et al., 1994). The lower halocline is characterized by increasing temperatures and salinities with depth until they match Atlantic Water values (Rudels et al., 1991). This layer has a mean salinity of approximately 34.2 ± 0.3 and is associated with minimum values in conservative nutrient-based tracer NO ($NO = O_2 + 9\ NO_3^-$ (Broecker,1974)).

Below the halocline, a layer of Atlantic Water forms a temperature maximum at salinities around 34.85 at depths around 200-500m (Timofeyev et al., 1961; Coachman & Barnes, 1974;

Swift & Aagaard, 1981; Aagaard et al., 1985; Carmack, 1990; Pfirman et al., 1994). Intermediate and deep waters found below the Atlantic layer are colder and saltier than waters above, and effectively isolated from the surface. They are remarkably homogeneous and hundreds of years old (Schlosser et al., 1999). Despite the lack of topographic obstructions above 1,200 meters, intermediate water hydrographic properties are not uniform between the two main Arctic Ocean basins but show a clear front above the Lomonosov Ridge, with the Makarov Basin being warmer than the Amundsen Basin by ca. 0.25 ºC.

The classification of the Atlantic water inflows in the Arctic Ocean has been extensively addressed since the onset of scientific Arctic exploration (e.g., Nansen, 1902; Coachman & Barnes (1963); Carmack, 1990; Swift & Aagaard, 1981; Aagaard et al., 1985) and continues to be investigated (Pfirman et al., 1994; Rudels et al., 2004; Woodgate et al., 2007; Schauer et al., 2008; Newton et al., 2013; Rudels et al., 2013; Polyakov et al., 2017). In this study, we define the water masses for upper (FSBW) and lower (BSBW) branches of the Atlantic layer in terms of potential density anomaly σ_0-surfaces. Specifically, we set the potential density ranges to be 0.07 kg m^{-3} (i.e., $\overline{\sigma}_0 \pm 0.035$ kg m^{-3} (Frank et al., 1998; Mauldin et al., 2010)). To determine the appropriate σ_0 −surface representing FSBW, we use an approach similar to the 'core-layer' method first described by Wüst (1935) and used by Coachman and Barnes (1963) in their classic study of the evolution and distribution of Atlantic waters in the Arctic Ocean. The most distinctive features of the FSBW are prominent potential temperature (θ) and salinity maxima. Although FSBW immediately starts being modified by shelf-basin interactions and vertical mixing as it enters the Arctic Ocean through Fram Strait, it never ceases to exhibit maxima in both temperature and salinity. Indeed, a prominent subsurface maximum is still observed in the Beaufort Sea, the southern Canada Basin,

Thus, the distribution of the temperature and salinity maxima can be used as a marker for the spreading of FSBW. To determine the isopycnal surface best representing the warm core of the Atlantic layer, we average the potential density at the depth of the maximum potential temperature (depth > 80m) for each station. This analysis produces a $\overline{\sigma}_0$ of 27.901 kg m^{-3}, which agrees with values cited in several other studies (e.g., Rudels et al., 2000; Smethie et al., 2000; Shimada et al., 2004). Thus, we define the density range of FSBW to be 27.866 kg $m^{-3} \leq \sigma_0 \leq$ 27.936 kg m^{-3}. When averaging the properties for the water samples that fall within this density range, we obtain the following values: average pressure of 289 m (100–460 m), mean salinity of 34.85 (34.78–35.02), and mean potential temperature of 1.22 ºC (0.34–2.87 ºC).

For the BSBW core, we used the density range of $27.950 \leq \sigma_0 \leq 28.020$ kg m^{-3} (27.985 ± 0.035 kg m^{-3}) using the definition previously established and confirmed by several studies (Rudels et al., 1994; Frank et al., 1998; Smethie et al., 2000; Mauldin et al., 2010). For the data part of our analysis, the mean BSBW properties are: $34.74 \leq S \leq 34.90$ (mean: 34.86) and -0.76 ºC $\leq \theta \leq$ 1.1 ºC (mean: 0.25 ºC). The BSBW layer extends between 350 and 1100 m. Here, we trace these waters from their origins, in Fram Strait and the St. Anna Trough, around and through the Arctic, to their exit points, on the northern sides of the Canadian Arctic Archipelago and Fram Strait.

1.3 Data and Method

1.3.1 Sample Collection and Measurement

This study uses the transient tracers ^{3}H (tritium, the radioactive isotope of hydrogen) and ^{3}He, the lighter isotope of helium and decay product of tritium, together with hydrographic data from 21 cruises to the Arctic Ocean (Figure 1) covering 25 years of Arctic Ocean section work.

The water samples were collected from icebreakers and submarines, as well as during aircraft-based surveys (Table 1).

With the exception of the ARK-IX/4 and ARK-XI/1 cruises, tritium and helium isotope samples were measured at the Lamont-Doherty Earth Observatory (LDEO), following procedures described by Ludin et al. (1998). Tritium and helium isotope samples from ARK-IX/4 and ARK-XI/1 were measured at the Institute for Environmental Physics at the University of Heidelberg, as described by Bayer et al. (1989). Both laboratories analyzed ^{3}H by the ^{3}He-ingrowth method. The ^{3}H measurement precision is ± 1–2% or 0.01–0.02 TU, whichever is larger. Helium isotopes are reported as $\delta^{3}He$, the percent deviation of the measured $^{3}He/^{4}He$ in a sample from the atmospheric air standard, $R_{atm} = 1.386\ 10^{-6}$ (Clarke et al., 1976).

Table 1: Oceanographic cruises that suplied data for this study.

Cruise Name	Vessel	Years
ARK-IV/1	R/V Polarstern	Jul–Aug 1987
Oden1991	I/B Oden	Aug–Oct 1991
ARCRAD	U.S.G.S. Polar Star	Jul–Aug 1993
ARK-IX/4	R/V Polarstern	Aug–Sep 1993
SCICEX-93	U.S.S. Pargo	Aug–Sep 1993
AOS 94	C.C.G.S. Louis S. St-Laurent	Jul–Aug 1994
ARK-XI/1	R/V Polarstern	Jul–Sep 1995
SCICEX-96	U.S.S. Pogy	Sep–Oct 1996
ARK-XII	R/V Polarstern	Jul–Sep 1996
JOIS4	C.C.G.S. Louis S. St Laurent	Sep–Oct 1997
SCICEX-99	U.S.S. Hawkbill	Sep–Oct 1999
Oden 2005	I/B Oden	Aug–Sep 2005
Switchyard 2005–2013	Aircrafts	Apr–May 2005-2013

Measurement precision for $\delta^{3}He$ is ± 0.2–0.3%, and that for ^{4}He ±1–2%. Typically, the uncertainties of the tritium and helium measurements result in errors of the $^{3}H/^{3}He$ ages of less than 1.0 years for ages lower than ca. 25 years and up to ca. 2 years for ages above 25 years. The

two laboratories have been intercalibrated, with measurement differences for ^{3}H and He isotope data typically falling into the range of the analytical errors.

Our database comprises 11,676 individual samples obtained at 476 stations (for geographical locations, see Figure 1). Of those, 1312 fall within the FSBW potential density range defined for this study. A total of 431 ^{3}H/^{3}He ages from 242 stations are used in our analysis of the FSBW layer, and for the BSBW layer we used 414 ^{3}H/^{3}He ages from 191 stations. Out of the total hydrographic stations that are part of our analysis, ca. 60% are located within the Eurasian Basin, 20% in the Makarov Basin, and 20% in the Canada Basin.

1.3.2 Tritium Helium Dating Method

Tritium (^{3}H) is the radioactive isotope of hydrogen and decays into the noble gas isotope ^{3}He by beta decay with a half-life of 12.32 ± 0.02 years (Lucas & Unterweger, 2000). Naturally occurring tritium is extremely rare, with a global inventory of only a few kilograms. Thermonuclear weapons testing released several hundred kilograms of tritium into the environment – mainly the stratosphere – resulting in a concentration peak in precipitation in 1963. The concentration of ^{3}H in Arctic precipitation and river runoff reached several thousand TU (Tritium Unit; 1 TU is a tritium to hydrogen ratio of 10^{-18}), ca. three orders of magnitude above the natural background level (Östlund, 1982)

The ^{3}H/^{3}He age is defined as the time elapsed since a water parcel has been isolated from gas exchange with the atmosphere. During that time ^{3}He is accumulated from radioactive decay of ^{3}H, and the apparent age can be calculated from the ^{3}H/^{3}He ratio (Eq. 1).

$$\tau = \frac{12.32 \text{ years}}{\ln 2} \ln\left[1+\frac{^3\text{He}_{\text{tritiogenic}}}{[^3\text{H}]}\right] \quad (1a)$$

where τ is the ^{3}H/^{3}He age (years), $[^3\text{He}_{\text{tritiogenic}}]$ is the ^{3}He from radioactive (TU), and ^{3}H is the tritium concentration measured in the sample (TU). ^{3}H/^{3}He data are routinely used to

estimate the mean spreading rates of ocean water masses (e.g., Jenkins & Clarke, 1976; Schlosser et al., 1995; Smethie et al., 2000; Mauldin et al., 2010).

In addition to uncertainties introduced during sampling and measurement, there are several sources of systematic errors intrinsic to $^{3}H/^{3}He$ age estimates: loss of ^{3}He due to gas exchange with the atmosphere, (partial) dissolution of air bubbles, mixing, and terrigenic ^{3}He (e.g., Schlosser et al., 1995; Wallace et al., 1992). Transient tracers, such as $^{3}H/^{3}He$, are not conservative with respect to mixing, as both their absolute concentrations and age signature (relative ratios) change with time. Apparent spreading rates inferred from $^{3}H/^{3}He$ age data are typically lower than the corrected velocity because they don't account for the mixing between the recently renewed waters at the boundary and the older waters of the interior.

1.4 Results

1.4.1 Hydrography

For each section, we identify the samples that represent the two distinct Atlantic Water cores. Hydrographic properties falling within the potential densities of FSBW (27.866 and 27.936) and BSBW (27.950 and 28.020) are averaged at each station (Figure 2). The distributions of potential temperature and salinity are mapped in Figures 3a and 3b, and the isopycnal surfaces are displayed in Figure 3c. Despite interannual variability in the properties and transport of water flowing through Fram Strait and Barents Sea into the Arctic Ocean (Loeng et al., 1997; Grotefendt et al., 1998) there are well defined patterns in the distribution of the hydrographic properties. At Fram Strait, salinity and temperature are at their maximum values which then decrease monotonically along the pathways around the Arctic Ocean basins as already pointed out by Coachman and Barnes (1963). As FSBW travels away from its injection point in Fram Strait, it is progressively modified by lateral intrusions of shelf water and vertical mixing with the overlying halocline and the deeper BSBW. Overall, the core of the modified FSBW that exits the Arctic Ocean flowing southward through Fram Strait is ca. 2ºC colder, ca. 0.2 fresher, and 200-300m deeper than the Atlantic inflow. Conversely, the lower BSBW component is initially colder and fresher and then becomes warmer and saltier *en route* along its pathway through the Arctic Ocean on the isopycnal surface $\sigma_0 = 28.0$.

More specifically, as it enters the Nansen Basin from the Greenland-Norwegian Sea, FSBW shows a prominent potential temperature maximum (2.5–3.0 ºC) and a salinity maximum (34.95–35.00) between 100 m and 200 m depth (Figures 2a, 2b, and 2c). Within 500 km of Fram Strait, the FSBW flows at shallow depths and interacts with the polar surface water, as well as with different types of modified Atlantic waters that have either completed the whole circumpolar

boundary current or have recirculated southward following a shorter pathway. This water mass modification produces a cold, less saline surface layer that eventually thickens and becomes more homogenous due to freezing and winter convection and is the source of the halocline in the Eurasian Basin (Rudels et al., 1995). The average potential temperature for the hydrographic stations located between the regions north of Svalbard and the Santa Anna Trough within a boundary approximately 50 km wide, is 1.89 ± 0.2 ºC, the corresponding mean salinity is 34.91 ± 0.02, and the mean depth is 240 m.

North of the Severnaya Zemlya, FSBW encounters BSBW, a cold, saline wedge sinking down the St. Anna Trough. The two branches interact before continuing eastward along the Eurasian continental slope as part of the same boundary current system (Schauer et al., 2002; 2004). This interaction results in a larger local variability in both temperature and salinity for individual hydrographic stations with salinities ranging from 34.75 to 34.95 and potential temperature from 0.5–2.5 ºC. North of the Kara Sea, the average temperature maximum is 1.73ºC, (S: 34.89) at depths between 220–250 m. Along the continental slope north of the Laptev Sea, about 2,000 km downstream from Fram Strait, the subsurface temperature maximum has been reduced to 1.6 ± 0.1ºC and is found at depths between 250 m and 270 m. The mean salinity of these waters is 34.87.

A well-defined horizontal front in potential temperature and salinity is positioned along the Lomonosov Ridge on a cross section of ca. 150 km, with warmer, saltier water in the Amundsen Basin compared to the Makarov Basin (Figures 2a and 2b). The mean potential temperature gradient across the Lomonosov Ridge is 0.5 ºC and the salinity gradient is 0.05 psu.

Data also show progressive cooling and freshening of the FSBW along the ridge crest, from the Laptev Sea shelf (off the New Siberian Island at longitude 145ºE) to 88ºN and 60ºW. Farther

along the Ridge, toward Greenland from this point the parameter fields become less homogenous, signaling the presence of small-scale frontal features and temporal shifts in the positions of those fronts. Along this section on the Eurasian flank of the Lomonosov Ridge, FSBW mean potential temperature starts at ca. 1.7 ºC off the continental slope, decreases to 1.4 ºC at the North Pole, and 1.2 ºC at 88 ºN and 60 ºW. Along the western side of the ridge, the FSBW mean temperature decrease from 1.3–1.4 ºC at the junction with the East Siberian shelf to 0.7–0.9 ºC at 88 ºN and 60 ºW (ca. 1.0 ºC at the North Pole). The FSBW salinity spatial distribution is analogous to that described for temperature, with a gradual freshening occurring along the Lomonosov Ridge and a marked gradient sitting across it. On the Amundsen side FSBW mean salinity ranges from 34.87 to 34.85; and from 34.84–34.78 on the Canadian side. Within the Eurasian Basin, stations located in the Nansen Basin are significantly warmer and more saline than those in the Amundsen Basin.

Along the East Siberian continental slope, east of the Lomonosov Ridge, the FSBW continues to flow cyclonically around the continental margin and is cooled and freshened primarily by interactions with dense waters originating on the shelves and cascading down the slope. The stations in the Chukchi Abyssal Plain still show a well-defined potential temperature maximum of 0.8–1 ºC (S: 34.8) at ca. 250 m depth. The mean values of potential temperature and salinity values along the Mendeleyev Ridge are 0.7ºC and 34.78, respectively. In general, the FSBW core properties show lesser spatial gradients and are more homogeneous in the Canadian Basin than in the Eurasian Basin. Mixing along long-time scales with Canadian Basin waters contributes to homogenize the FSBW (Smethie et al., 2000). This reduced variability might also result from the fact that the FSBW core is found deeper in the water column and isolated from the surface by a thicker surface layer (polar mixed layer and halocline waters) than observed in the Eurasian

Basin. This deepening of the FSBW core is observed in the Beaufort Gyre, a surface anticyclonic cell centered in the southern Canada Basin where the Ekman signal is large (Carmack et al., 2016). The circulation of the mixed layer and upper halocline is largely driven by surface stress (wind forcing and sea ice cover). Via Ekman transport, the lateral movements of surface waters generate a vertical transport in the water column that reach the intermediate depths of the Atlantic layer (Hunkins, 1966; Pond & Pickard, 1983). The bowing of isopycnals in the Canada Basin roughly follows a two-peak seasonal cycle associated with the strength of the anticyclonic wind curl in the Beaufort Gyre and the freshwater production during the summer sea ice melt (Proshutinsky et al., 2009). On average, the FSBW core in the southern Canada Basin has a potential temperature of 0.45–0.50ºC and salinities of 34.75–34.78 at depths of 350-450m.

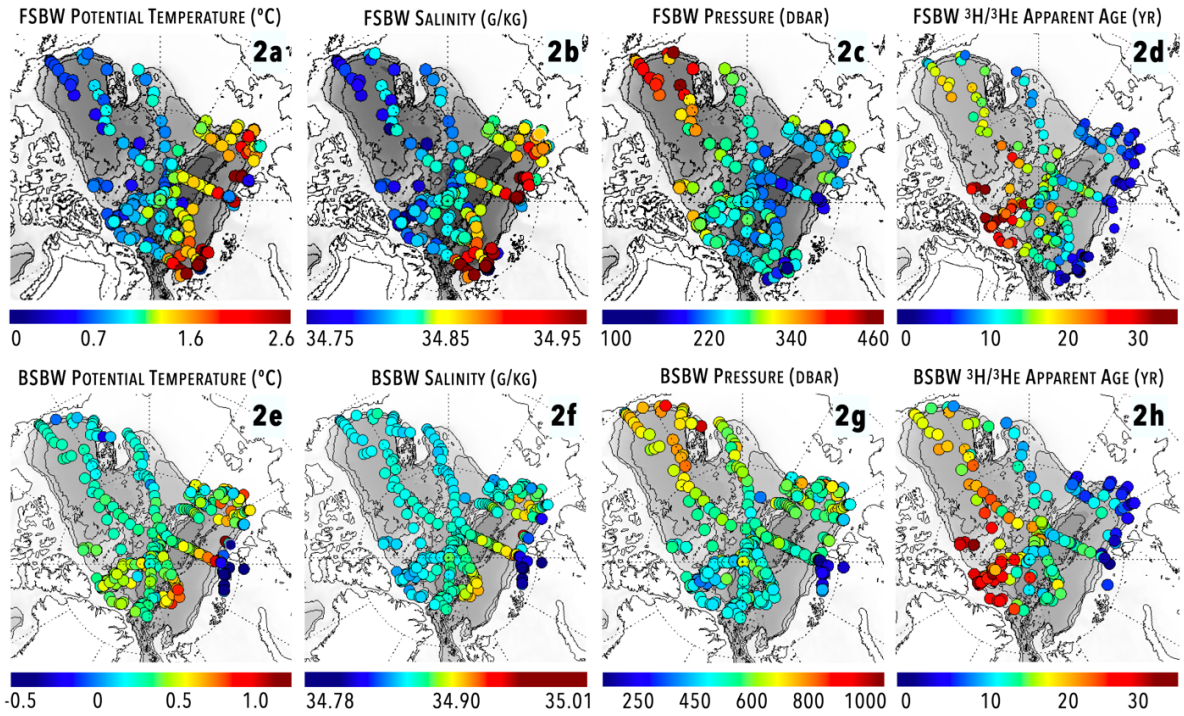

Figure 2. Maps showing the averaged properties of Fram Strait Branch Water (FSBW), top panels; and Barents Sea Branch Water (BSBW), bottom panels. Hydrographic station locations are displayed as filled circles colored according to the average Potential Temperature, Salinity, water pressure, and $^{3}H/^{3}He$ apparent ages.

In the Makarov Basin and in the Chukchi Abyssal Plains the average depth of the subsurface temperature maximum is 280-300 m (Figure 2a). In the Beaufort Sea and central Canadian Basin, the core of the FSBW deepens to its maximum values and is located at depths between 400–450 m. In the Lincoln Sea, north of the eastern Canadian Archipelago and Greenland, the average depth of the FSBW is back to 300-350 m. This area, extending up the North Pole and stretching between Cape Columbia, Canada, and Cape Morris Jesup, Greenland, was intensively sampled during the Arctic Switchyard Project, an annual hydrographic survey that took place between 2005 and 2013 (Timmermans et al., 2011; Morison et al., 2012). At stations located within the Switchyard region, FSBW has an average potential temperature of 0.50 ±0.15 ºC and a salinity of 34.79 ± 0.02.

BSBW has already been significantly modified before penetrating the Nansen Basin at the Santa Anna Trough. During its flow across the Barents Sea and Kara Sea, this Atlantic inflow is significantly cooled through heat loss to the atmosphere and its salinity modified by seasonal shelf processes such as sea ice formation and melting, or addition of meteoric water (Schauer et al., 2002).

Stations located west of Severnaya Zemlya on the northern Kara Sea shelf, still outside the Nansen Basin, have mean potential temperatures close to the freezing point (-1.0–0.8 ºC) and salinities between 34.76–34-78 at an average depth of 250 m (Figures 2e, 2f, and 2g). BSBW descends to ~600 m-depth as a series of intermittent cold plumes partially displacing and interacting with FSBW before continuing to flow eastward along a deeper isopycnal surface. The stations located along the confluence front with the FSBW, right off the Santa Anna Trough, show a larger variability in their hydrographic properties. The potential temperature ranges between -0.7 and 1.0 ºC, (mean 0.38 ºC), salinities range from 34.86 to 34.93, (mean 34.87), and

depths reach from 300 to 600 m (mean 450m). The larger variation within the BSBW density horizon in the eastern Nansen Basin and along the Gakkel Ridge result from displacement of fronts, both horizontal and vertical, intermittent vertical convection from ice formation, and strong interleaving with the warmer, upper branch (Rudels et al., 1999; 2000). North of the Laptev and East Siberian seas, the core of the BSBW has a mean potential temperature of 0.38 ± 0.15ºC, and a salinity of 34.88 ± 0.01. In this region, approximately located between 120 ºE and 150 ºE longitudes and stretching north to 85º N, the BSBW isopycnal surface has deepened to intermediate depths of 750 ± 50 m, further limiting the sources of ventilation, thus largely conserving its core properties as it continues to flow cyclonically around the Arctic Ocean. Both potential temperature and salinity along the BSBW isopycnals show minimal spatial gradients or structure across the Arctic Ocean, both within the boundary current and in basin interiors (Figures 2e, 2f, and 2g). Compared to FSBW, BSBW is quite homogeneous across the Amundsen Basin, Makarov Basin, and Canada Basin. This is due to the fact that it has limited sources of ventilation and is not exposed to mixing with the surface layer (Smethie et al., 2000). The average parameters of water samples within BSBW density range ($27.95 \leq \sigma_0 \leq 28.02$) are $0.0\ ºC \leq \theta \leq 0.4\ ºC$ and $34.86 \leq$ salinity ≤ 34.88. The average depth in these regions ranges from 550 m to 1000 m.

The BSBW at the stations located within the Amundsen Basin is consistently warmer and saltier than those in the Makarov and Canada basins. Their potential temperature and salinity are 0.33 ± 0.15 ºC and 34.88 ± 0.01, respectively. For comparison, in the Beaufort Sea we observe potential temperatures of 0.17 ± 0.14ºC and salinities of 34.86 ± 0.004. In the Lincoln Sea (southern Switchyard region) BSBW shows higher mean temperatures (mean 0.4 ºC) and lower salinities (mean 34.85) than observed in other regions of the Arctic Ocean (Figures 2e and 2f).

The average depth of BSBW shows a similar spatial structure to that of FSBW (Figure 2e). The BSBW isopycnals deepen to 850–1100 m in the southern Canada Basin and Beaufort Sea, and shoal to 550–650 m in the Switchyard Region and western Amundsen Basin.

1.4.2 Apparent $^3H/^3He$ Ages

The age spatial structures for FSBW and the BSBW are obtained as the mean of tracer age data at a particular location from water samples falling within the corresponding density horizons (Figures 2d and 2h). We estimate the apparent tracer age uncertainty at each location as the standard deviation of the values used in the average calculation, rather than the variations in tracer age from propagating the analytical error of the tritium and helium measurements through the age calculation. The uncertainty reflects variability in both space and time, since the tracer data were collected over a period of roughly three decades.

Age estimates for upper halocline waters range from 2 to 6 years and are remarkably homogeneous in both the Eurasian and Canadian basins (Ekwurzel et al., 2001). As indicated above, these values are to be considered as lower boundaries due the possible loss of tritiogenic ^3He to the atmosphere via gas exchange and the diffusion of He into sea ice. Mean apparent ages in the lower halocline span the age range between 5 and 15 years (Schlosser et al., 1999; Ekwurzel et al., 2001). In the Atlantic layer the apparent tracer ages range from a few years to decades. The apparent tracer ages generally increase from the entry point to the Arctic Ocean along the boundary flow around the Eurasian and Canadian basins and into the interior of those basins.

The youngest $^3H/^3He$ ages, ca. 3–5 years, occur at the injection points in Fram Strait (FSBW) and at the Santa Anna Trough (BSBW). The oldest apparent ages, ca. 30–35 years, are found in the Switchyard region. In general, the apparent tracer ages are somewhat higher for BSBW compared to FSBW: the $^3H/^3He$ age averages for FSBW and BSBW are 13.3 years and

18.1 years, respectively. This tracer age difference does not show a significant trend around the boundary current loop and ranges from -3 to 8 years, where the negative values indicate that BSBW is locally younger than FSBW, which occurs in the eastern Nansen Basin. The largest differences are observed in the central Canada Basin. On average, the $^{3}H/^{3}He$ ages in the Eurasian Basin are 10 years younger than those observed in the Canadian Basin.

The mean apparent tracer ages for FSBW at stations located north of Spitsbergen, east of Franz Josef Land (longitude $\lambda = 45^{o}$ E), is 3.4 ± 1.6 years. The mean $^{3}H/^{3}He$ age at the Santa Anna Trough is 5.0 ± 1.5 years and increase to 5.5 ± 0.7 years in the northern Laptev Sea. The FSBW age undergoes a partial 'reset' to younger ages as it interacts and mixes with the BSBW inflow at St. Anna Trough. The stations located at the intersections of the continental slope with the Lomonosov Ridge show ages of 8 ± 1.5 years. In the Chukchi Abyssal Plain, east of the Chukchi Plateau, the average $^{3}H/^{3}He$ is 10.8 ± 1 years and increases to 17.1 ± 3 years in the Beaufort Sea. The oldest ages for FSBW are observed on the Alpha Ridge and in the Switchyard region with an average of 28 ± 3 years.

The mean apparent tracer age for BSBW at its entry point into the Nansen Basin, north of the Santa Anna Trough is 4.3 ± 2.6 years at. Mean ages increase to 6.8 ± 0.9 years in the northern Laptev Sea, and to 10 ± 2.5 at the intersection of the Lomonosov Ridge with the East Siberian Shelf (ca. 145ºE). The observed $^{3}H/^{3}He$ ages range from 12 to 15 years for stations located in the Chukchi Abyssal Plain. On the Beaufort Sea slope the mean tracer age values increase to 21.5 ± 1.8 years. The oldest ages observed in BSBW are 31 ± 3 years and are found in the Switchyard region.

The BSBW mean ages increase linearly along the Mendeleev Ridge moving from the East Siberian Shelf to the southern extension of the Alpha Ridge from 10 ± 2 year to 26 ± 2

years. A front in the apparent tracer ages is observed along the Lomonosov Ridge, separating younger waters on the Eurasian side from older values on the Canadian side. The age difference across this deep-sea ridge is 6–10 years and occurs over a distance of ca. 200 km, with younger waters consistently on the Amundsen Basin side. This striking front in apparent tracer ages is noticeable on the isopycnal surfaces of both FSBW and BSBW. In the Eurasian Basin the oldest apparent ages are centered over the abyssal plains of the Amundsen and Nansen basins. The tracer distribution in the Eurasian Basin shows apparent ages linearly increasing along the eastern side of the Gakkel Ridge, with values ranging from 6 to 17 years. The stations with the lowest apparent tracer ages in the Canadian Basin are located within a 200km band centered over the Mendeleyev Ridge. On a section running from the East Siberian Shelf to the Alpha Ridge, apparent tracer ages increase from 10 to 20 years within the FSBW density horizon; and from 14 to 25 years on the BSBW isopycnal (Figures 2e and 2h).

1.5 Discussion

That Atlantic-origin waters move through the Arctic Ocean cyclonically along the boundaries of the deep basins and tracking the submarine ridge system has long been known and widely confirmed by hydrographic and tracer distribution (e.g., Coachman & Barnes, 1963; Aagaard, 1989; Rudels et al., 1994, 1999; 2004; Smethie et al., 2000; Schauer et al., 2002; Polyakov et al., 2005; Woodgate et al., 2007; McLaughlin et al. 2004, 2009;), direct current flow measurements (e.g., Newton & Sotirin, 1997; Woodgate et al., 2001; Dmitrenko et al., 2008; Pnyushkov et al., 2015). Indeed, at the very onset of Arctic oceanographic expeditions Norwegian explorer Fridtjof Nansen observed that the Atlantic-derived subsurface temperature maximum was flowing as a “well-defined current and in a cyclonic direction” (Nansen, 1902; Helland-Hansen & Nansen, 1912). The distributions of tritium/^{3}He ages on the isopycnal

surfaces of the FSBW and BSBW show that their flows are strongly guided by seabed topography in agreement with the schematic of Atlantic waters circulation in the Arctic Ocean firstly outlined by Rudels et al. (1994) (Figures 3a and 3c). The correlation between transient tracer age gradients and circulation paths will be discussed in detail in 5.1.

1.5.1 Pathways

We delineate pathways of the FSBW and BSBW circulation patterns by following tracer age gradients. The trajectory and distance calculations along different circulation pathways are described in detail in section 5.2.

The mean apparent tracer ages for FSBW at stations located north of Spitsbergen, east of Franz Josef Land (longitude $\lambda = 45^{o}$ E), is 3.4 ± 1.6 years. The relatively young FSBW ages observed at stations located off Fram Strait are the result of ventilation and gas exchange in the sea ice free zone outside the Arctic Ocean followed by a rapid eastward transport along the continental margin of the southern Nansen Basin (Wallace et al., 1992).

$^{3}H/^{3}He$ apparent age distribution indicates that east of the Santa Anna Trough the two branches follow the same flow paths (Smethie et al., 2000). Starting at the entry points to the Arctic Ocean we identify flow paths by following the age gradients along surfaces of constant potential density around the continental slope and parallel to the major submarine ridges of the Arctic Ocean. Applying this method, the boundary current loop along the shelf slope around the entire Arctic Ocean is clearly visible (Figure 3). This boundary current is well defined along the continental shelf of both the Eurasian Basin (EBBC) and the Canadian Basin (CBBC).

In addition, we see six more distinct branches, all strongly guided by seabed features and in agreement with previously derived flow paths (Figures 3a and 3b). Two of these are located within the Eurasian Basin and are directed towards Greenland, i.e., back towards Fram Strait. We refer to them as the Eurasian Basin Return Branch (EBRB) roughly parallel to the Gakkel Ridge

and the Lomonosov Ridge Amundsen B. Branch (LRAB), flowing along the eastern flank of the Lomonosov Ridge (eastern side).

The next two branches are here referred to as the Lomonosov Ridge Return Branch (LRRB), flowing on top of the Lomonosov Ridge, and the Mendeleyev Ridge Returning Branch (MRRB), aligned with the Mendeleyev Ridge. Both the LRRB and the MRRB are directed towards Fram Strait. The original circulation scheme of Rudels et al. (1994) outlines a full cyclonic circulation cell in the Makarov Basin, with AW flowing towards Greenland along the Alpha-Mendeleev Ridge and back to Siberia along the western flank of the Lomonosov Ridge. This study only includes the first half of this circulation cell (MRRB), as there are not enough data to fully analyze second half due to convergence of different flow paths.

The $^{3}H/^{3}He$ age distribution in the Canada Basin interior indicate that fractions/portions of the boundary current are diverted northward into the Canada Basin interior along two further pathways, off the Chukchi Plateau/Northwind Ridge and one following the Alpha Ridge into the central basin. The actual trajectories taken by Atlantic branches west of the Lomonosov Ridge, for instance over complex topography north of the Chukchi Sea, are still largely presumed (Woodgate et al., 2007).

AW cyclonically flows along the different circulation branches and eventually exits the Arctic Ocean either through the Canadian Archipelago or Fram Strait (Rudels et al., 2012; Dodd et al. 2012). Interleaving between water masses with different ventilation histories and hence $^{3}H/^{3}He$ ages can also contribute to increase the local spread of apparent tracer ages. This can be observed at the intersection of topographic features where different circulation paths converge. The junction of the Lomonosov Ridge with the continental shelves of Greenland and Canada,

where the three flow branches of LRAB, LRRB, and CBBC intersects, and Fram Strait are two examples.

The circulation pattern established on the basis of $^{3}H/^{3}He$ apparent age gradients agrees with the previously established circulation pathways using hydrographic and current meter data. This holds for both the well consolidated loops, such as the outer boundary current, and the ones that are less well established. Besides the ageing along the Arctic Ocean boundary current, the $^{3}H/^{3}He$ data also show a circulation structure that is correlated with the underlying ridge system.

Part of the FSBW never reaches the Makarov Basin but recirculates back toward the Fram Strait along the Gakkel Ridge and the Lomonosov Ridge filling the Nansen and Amundsen basins with warm and saline waters. The Eurasian Basin Return Branch (EBRB) turns north and detaches from the continental slope roughly in front of Severnaya Zemlya before flowing back towards Fram Strait along the Gakkel Ridge. Within the Eurasian Basin, stations located in the Nansen Basin are significantly warmer and more saline than those in the Amundsen Basin in accordance with the AW recirculation scheme (Figures 3a and 3b). Rudels et al. (2012; 2013) favor the hypothesis that a large fraction of FSBW recirculates in the Nansen Basin rather than reaching the Amundsen and Canadian basins. The temperature front aligned with the Gakkel Ridge (Figure 2a) is consistent with this assumption. Whereas several studies suggest the presence of an Atlantic return flow in the central Eurasian Basin, none provides quantitative data on the exact pathway and flow pattern of this branch (Rudels et al., 2000; Schauer et al., 2004; Aksenov et al., 2011). Tracer data indicate the presence of a returning branch on top of the Lomonosov Ridge (LRAB and LRRB) and confirm the presence of a faster, more structured flow on the Amundsen Basin side of the Lomonosov Ridge.

The Atlantic Water $^{3}H/^{3}He$ age distribution in the Eurasian Basin is clearly correlated with the underlying bathymetry. Higher ages are observed in the basin interior over the abyssal plains compared to the outer perimeter as defined by the shelf sea margins of the Barents, Kara, and Laptev seas in the south, and by the eastern flank of the Lomonosov Ridge in the north.

In addition, we see six more distinct branches, all strongly guided by seabed features and in agreement with previously derived flow paths (Figures 3a and 3b). Two of these are located within the Eurasian Basin and are directed towards Greenland, i.e., back towards Fram Strait. We refer to them as the Eurasian Basin Return Branch (EBRB) roughly parallel to the Gakkel Ridge and the Lomonosov Ridge Amundsen B. Branch (LRAB), flowing along the eastern flank of the Lomonosov Ridge (eastern side).

The next two branches are here referred to as the Lomonosov Ridge Return Branch (LRRB), flowing on top of the Lomonosov Ridge, and the Mendeleyev Ridge Returning Branch (MRRB), aligned with the Mendeleyev Ridge. Both the LRRB and the MRRB are directed towards Fram Strait. The original circulation scheme of Rudels et al. (1994) outlines a full cyclonic circulation cell in the Makarov Basin, with AW flowing towards Greenland along the Alpha-Mendeleev Ridge and back to Siberia along the western flank of the Lomonosov Ridge. This study only includes the first half of this circulation cell (MRRB), as there are not enough data to fully analyze second half due to convergence of different flow paths.

The $^{3}H/^{3}He$ age distribution in the Canada Basin interior indicate that fractions/portions of the boundary current are diverted northward into the Canada Basin interior along two further pathways, off the Chukchi Plateau/Northwind Ridge and one following the Alpha Ridge into the central basin. The actual trajectories taken by Atlantic branches west of the Lomonosov Ridge,

for instance over complex topography north of the Chukchi Sea, are still largely presumed (Woodgate et al., 2007).

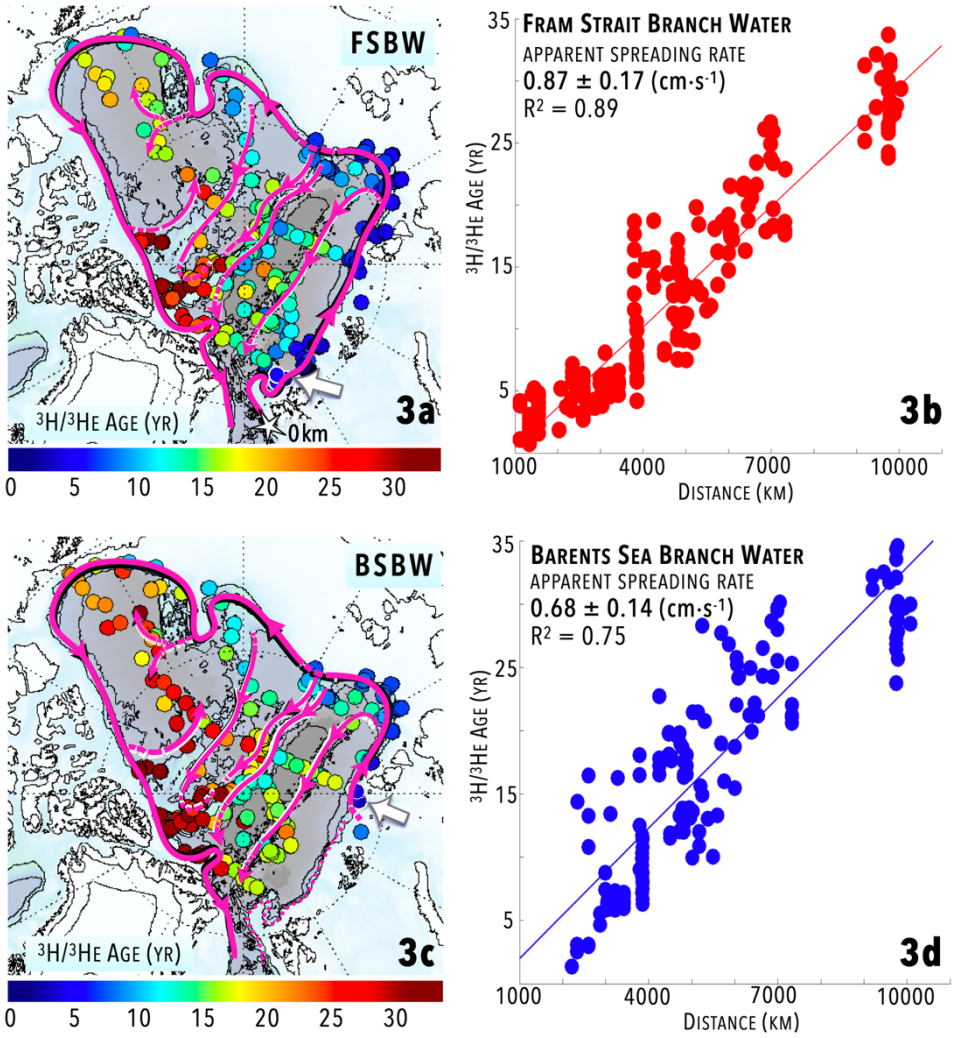

Figure 3. Schematic of Atlantic waters circulation in the Arctic Ocean after Rudels et al. (1994; 2011) displayed on top of the mean apparent ^{3}H/^{3}He ages for the FSBW, shown in 3a, and BSBW in 3c. Panels 3b and 3d: mean apparent ^{3}H/^{3}He ages plotted as a function of distance from Fram Strait. The apparent spreading rate is obtained from an non-weighted linear regression. The principal sources of scatter are the different spreading rates along different flow paths. The errors for the apparent velocities consider the ^{3}H/^{3}He age analytical error, uncertainty in the distance (± 15%), and uncertainty derived from the linear fit (based on 95% confidence bounds; mean error: ± 0.12 cm s^{-1}).

The Atlantic water flowing along the different loops of the circulation branches eventually exits the Arctic Ocean either through the Canadian Archipelago or the Fram Strait (Rudels et al., 2012). Interleaving between water masses with different ventilation histories and hence $^{3}H/^{3}He$ ages can also contribute to increase the local spread of apparent tracer ages. This can be observed at the intersection of topographic features where different circulation paths converge. The junction of the Lomonosov Ridge with the continental shelves of Greenland and Canada, where the three flow branches of LRAB, LRRB, and CBBC intersects, and Fram Strait are two examples.

The circulation pattern established on the basis of $^{3}H/^{3}He$ apparent age gradients agrees with the previously established circulation pathways using hydrographic and current meter data. This holds for both the well consolidated loops, such as the outer boundary current, and the ones that are less well established. Besides the ageing along the Arctic Ocean boundary current, the $^{3}H/^{3}He$ data also show a circulation structure that is correlated with the underlying ridge system.

Part of the FSBW never reaches the Makarov Basin but recirculates back toward the Fram Strait along the Gakkel Ridge and the Lomonosov Ridge filling the Nansen and Amundsen basins with warm and saline waters. The Eurasian Basin Return Branch (EBRB) turns north and detaches from the continental slope roughly in front of Severnaya Zemlya before flowing back towards Fram Strait along the Gakkel Ridge. Within the Eurasian Basin, stations located in the Nansen Basin are significantly warmer and more saline than those in the Amundsen Basin in accordance with the AW recirculation scheme (Figures 3a and 3b). Rudels et al. (2012; 2013) favor the hypothesis that a large fraction of FSBW recirculates in the Nansen Basin rather than reaching the Amundsen and Canadian basins. The temperature front aligned with the Gakkel Ridge (Figure 2a) is consistent with this assumption. Whereas several studies suggest the

presence of an Atlantic return flow in the central Eurasian Basin, none provides quantitative data on the exact pathway and flow pattern of this branch (Rudels et al., 2000; Schauer et al., 2004; Aksenov et al., 2011). Tracer data indicate the presence of a returning branch on top of the Lomonosov Ridge (LRAB and LRRB) and confirm the presence of a faster, more structured flow on the Amundsen Basin side of the Lomonosov Ridge.

The Atlantic Water $^{3}H/^{3}He$ age distribution in the Eurasian Basin is clearly correlated with the underlying bathymetry. Higher ages are observed in the basin interior over the abyssal plains compared to the outer perimeter as defined by the shelf sea margins of the Barents, Kara, and Laptev seas in the south, and by the eastern flank of the Lomonosov Ridge in the north.

1.5.2 Apparent Spreading Velocities

$^{3}H/^{3}He$ apparent ages not only provide a clear and independent delineation of the Atlantic water circulation patterns, but also provide time scales for the circulation of Atlantic water in Arctic Ocean. A branch of water with low$^{3}H/^{3}He$ age gradients along its pathway corresponds to a 'fast' loop, whereas the branches with higher $^{3}H/^{3}He$ age gradients have a slower velocity flow rate.

In order to determine the apparent spreading rates, we first need to estimate the distances FSBW and BSBW have traveled away from their injection points along the different flow paths. In accordance with prior work cited above and our own analysis of the hydrographic data (Mauldin et al., 2010 and this study), we measure distance along the principal currents parallel to the bathymetric isolines. Thus, we calculate the distances traveled by the Atlantic water along the individual branches based on the continental slopes, ridges, and fracture zones (Mauldin et al., 2010). The starting point (distance = 0 km) for both Atlantic branches is arbitrarily set in Fram Strait at 7.82ºE and 78.78ºN, between Spitsbergen and the Svyatogor Rise and is marked by a white star in Figure 4). The distances from this point are measured by tracing the shortest isobath

along the continental slope or other topographic features using the International Bathymetric Chart of the Arctic Ocean (IBCAO) v3 500m-resolution bathymetric data (Jakobsson et al., 2012). The center of mass of the boundary current is located above the continental slope at water depths of 1,000–2,000 m (Woodgate et al., 2001; Woodgate et al., 2007). The hydrographic stations closest to Fram Strait, northeast of Spitzbergen, are located at a distance of 1100–1300 km (ARK-IV/3, 1987; Oden, 1991; ARKIX/4, 1993) from the entry point in Fram Strait defined above. The St. Anna Trough is located at ca. 2,010–2,100 km from this entry point (e.g., ARK-XII, 1996; ARK-XI/1, 1995). The junction of the Lomonosov Ridge with the Eurasian continent stretches between 3580 km (Amundsen Basin side) and 3750 km (Makarov Basin side). Stations located on the continental slope of the southern Canada Basin/Beaufort Sea stretching from Point Barrow (ca. 158ºW) to the Amundsen Trough (130ºW), are located at 6600 km–7900 km distance from the entry point. The Switchyard Region, the farthest point from the entry location in Fram Strait for which we have data, is at approximately 10,000 km. Finally, the complete loop around the continental slope to the exit from the Arctic Ocean is ca.11000 km long. In this analysis, the end point is set in the western section of the Fram Strait, off the East Greenland Continental Shelf at 5ºW and 78.78ºN.

The boundary current circulation branches (EBBC and CBBC) are traced following the 1000 m isobath (Figure 4a and 4c). As we move further east, several bathymetric features generate uncertainties in the path length estimation. For example, as it crosses the Chukchi Borderlands, the AW branches can flow along three different trajectories (Shimada et al., 2004; Woodgate et al., 2007). First, they can loop north of the Chukchi Rise and north of the Northwind Ridge (1800-m isobath; length ca. 1200km). Next, they can flow through the Chukchi Gap, south of both the Chukchi Rise and the Northwind Ridge (following the 600-m isobath; ca.

550 km route). Lastly, they can loop north of the Chukchi Rise and south of the Northwind Ridge (following the 1000-m isobath; ca. 1,350 km route). The maximum difference is ca. 700 km (± 12%) calculated for this branch of the rim current (CBBC). In our distance calculations, we use the third, intermediate, flow path.

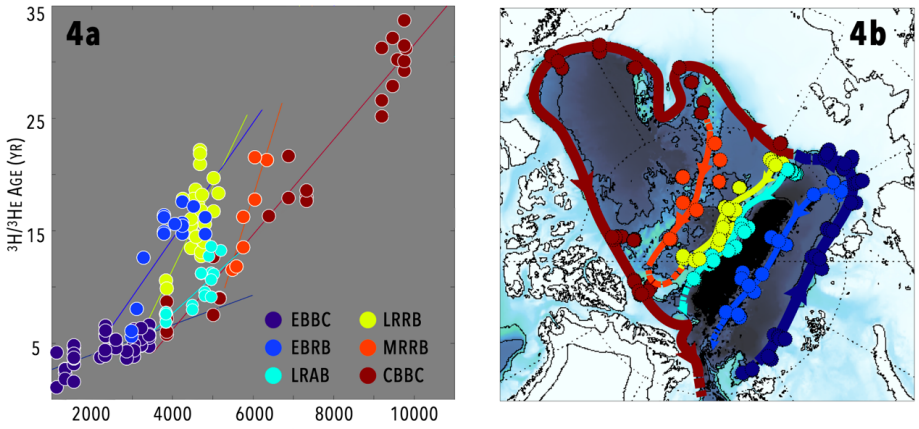

Table 2. *Apparent and corrected velocity estimates for FSBW along different circulation branches.*

Branch	Apparent Velocity	Corrected Velocity (cm s^{-1})	R^2	stn
Arctic Ocean	0.87 ± 0.17	2.42 ± 0.87	0.89	242
Arctic Ocean Boundary Current	0.88 ± 0.19	2.45 ± 0.90	0.93	75
Eurasian Basin Boundary Current (EBBC)	1.27 ± 0.50	3.53 ± 1.75	0.58	50
Canadian Basin Boundary Current (CBBC)	0.71 ± 0.18	1.97 ± 0.77	0.95	25
Eurasian Basin Return Branch (EBRB)	0.36 ± 0.19	1.00 ± 0.61	0.66	19
Lomonosov Ridge Amundsen B. Branch (LRAB)	0.61 ± 0.27	1.70 ± 0.91	0.74	20
Lomonosov Ridge Return Branch (LRRB)	0.20 ± 0.12	0.56 ± 0.37	0.47	27
Mendeleev Ridge Return Branch (MRRB)	0.26 ±0.10	0.72 ± 0.35	0.92	10

Figure 4. Geographical locations and mean apparent $^3H/^3He$ ages plotted as a function of distance for the hydrographic stations used to calculate the spreading rates for FSBW shown in Table 2. Data points in 5a and 5b are color coded by the corresponding circulation branch. The factor of 2.78 ± 0.83 cm s^{-1} used to obtain corrected current velocities is based on Mauldin et al. (2010). The errors for the apparent velocities consider the $^3H/^3He$ age analytical error, uncertainty in the distance (± 15%), and uncertainty derived from the linear fit (based on 95% confidence bounds; mean error: ± 0.10 cm s^{-1}).

Tables 2 and 3 summarize the results for the entire dataset, as well as for the individual circulation branches. Tritium/^{3}He age data from water samples included in the FSBW and BSBW water mass definitions plotted as a function of distance from Fram Strait follow a linear

trend (Figure 4b and 4d). When water samples falling within the FSBW density range and from stations along the continental rim or one of the circulation branches outlined in Figure 4a are included (242 stations), an unweighted least square fit of the data yields a slope of 275 km yr^{-1}, equivalent to an apparent velocity of 0.87 ± 0.17 cm s^{-1} (R^2 = 0.89) (Figure 4b). The same calculation for the BSBW yields a slope of 214 km yr^{-1}, equivalent to an apparent spreading velocity of 0.68 ± 0.14 cm s^{-1} (192 stations, R^2 = 0.75).

Our analysis of the pathway of the FSBW in Arctic Ocean boundary current includes 75 continental slope stations, of which 50 are located in the Eurasian Basin (EBBC) and 25 in the Makarov and Canada basins (CBBC) For the outer loop, including stations along the continental shelf from Svalbard to the Switchyard region, we estimate a mean apparent velocity is 0.88 ± 0.19 cm s^{-1} (R^2 = 0.93) (Figure 5). These stations are marked in Figure 5 by dark blue and red dots to indicate EBBC and CBBC respectively. Stations located downstream of the Lomonosov Ridge junction with the continental shelf follow different trends. They fall on a slope that is different from the one for the Eurasian Basin, with slower spreading rates obtained in the Canada Basin than in the basins upstream. The linear regression including only the data points on the Eurasian side of the Lomonosov Ridge (EBBC) yields a FSBW apparent velocity of 1.27 ± 0.50 cm s^{-1} (R^2 = 0.58). Downstream of the ridge, we estimate an apparent velocity of 0.71 ± 0.18 cm s^{-1} (R^2 = 0.95) for the FSBW. A slower boundary current transport for the core of the Atlantic layer in the Canada Basin than in the Eurasian Basin was originally proposed by Aagaard (1989) and has been confirmed by current meter data (Woodgate et al., 2001; Pnyushkov et al., 2015) and models (e.g., Aksenov et al., 2011). The decrease in the mean current flow coincides with a split in the boundary current into two separate branches at the intersection of the Lomonosov Ridge with the shelf slope, with roughly 3 ± 1 Sv flowing north along the ridge and 2 ± 1 Sv

following eastward into the Makarov Basin (Woodgate et al., 2001). Lower velocities in the eastward Canadian Basin current have been explained by the reduced PV lateral influx in the Canadian Basin compared to the Eurasian Basin (Yang et al., 2005); and by the local anticyclonic Beaufort Gyre's effect on ocean circulation extending down into the Fram Strait Branch of the Atlantic layer (McLaughlin et al., 2009; Woodgate et al., 2001; Karcher et al., 2012). We note in addition that reduced volume fluxes will carry with them a proportional decrease in the momentum (and PV) fluxes, while the dissipation of momentum along the continental slope, which is proportional to the layer thickness, is not diminished. The current then must slow to maintain a steady balance between momentum (or PV) input and dissipation.

The apparent velocity calculations for BSBW in the outer loop include data from 54 continental slope stations; out of these 22 are located in the Eurasian Basin (EBBC), and 32 east of the Lomonosov Ridge (CBBC). These stations are marked by dark blue (EBBC) and red dots (CBBC) in the map and scatter plot (Figures 6a and 6b). The mean apparent spreading rate for the entire outer loop, from the Santa Anna Trough to the Switchyard Region is 0.79 ± 0.13 cm s^{-1} ($R^2 = 0.97$). The mean apparent velocity in the EBBC is 0.67 ± 0.20 cm s^{-1} ($R^2 = 0.87$); and 0.74 ± 0.16 cm s^{-1} ($R^2 = 0.95$) along the Canadian continental slope. The slowest apparent spreading rates for FSBW and BSBW in the Eurasian Basin are observed at the returning branch along the Gakkel Ridge, EBRB, and are 0.36 ± 0.19 cm s^{-1} and 0.39 ± 0.21 cm s^{-1} respectively.

Tracer data indicate the presence of a slower current over the Lomonosov Ridge (LRRB) in addition to the returning branch in the Amundsen Basin (LRAB). The returning flow tracking the eastern flank of the Lomonosov Ridge (LRAB) is significantly faster than that for stations on top of the Lomonosov Ridge. The apparent velocities for FSBW along LRAB and LRRB are

0.61 ± 0.27 cm s^{-1} and 0.2 ± 0.12 cm s^{-1} respectively. Similarly, the LRAB and LRRB apparent velocities for BSBW are 0.89 ± 0.27 cm s^{-1} and 0.19 ± 0.10 cm s^{-1} respectively.

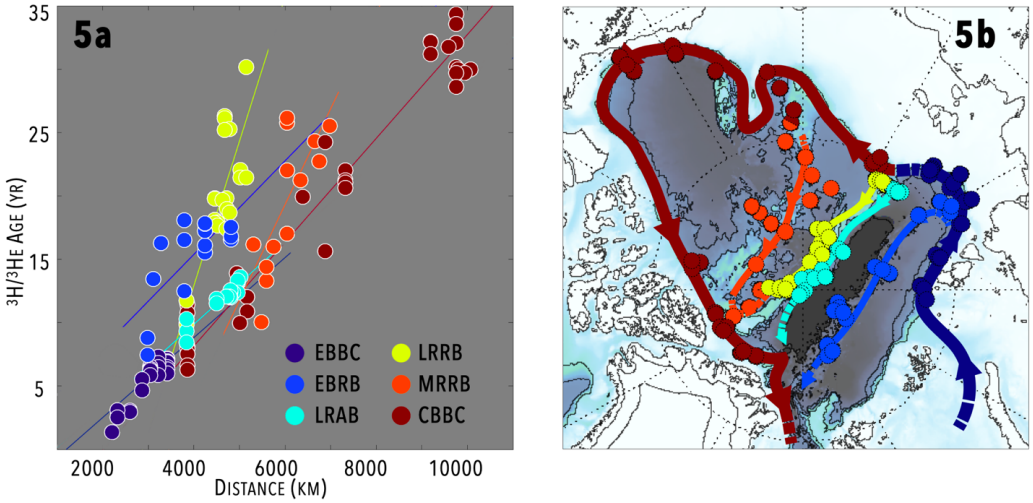

Table 3. *Apparent and corrected velocity estimates for BSBW along different circulation branches.*

Branch	Apparent Velocity	Corrected Velocity (cm s^{-1})	R^2	stn
Arctic Ocean	0.68 ± 0.14	1.89 ± 0.69	0.75	191
Arctic Ocean Boundary Current	0.79 ± 0.13	2.20 ± 0.76	0.97	56
Eurasian Basin Boundary Current (EBBC)	0.67 ± 0.20	1.85 ± 0.79	0.87	22
Canadian Basin Boundary Current (CBBC)	0.74 ± 0.16	2.06 ± 0.76	0.95	32
Eurasian Basin Return Branch (EBRB)	0.39 ± 0.21	1.08 ± 0.66	0.63	17
Lomonosov Ridge Amundsen B. Branch (LRAB)	0.89 ± 0.27	2.46 ± 1.04	0.90	17
Lomonosov Ridge Return Branch (LRRB)	0.19 ± 0.10	0.54 ± 0.32	0.70	28
Mendeleev Ridge Return Branch (MRRB)	0.27 ± 0.13	0.75 ± 0.42	0.64	21

Figure 5. Geographical locations and mean apparent $^3H/^3He$ ages plotted as a function of distance for the hydrographic stations used to compute the spreading rates for BSBW shown in Table 3. Data points in 6a and 6b are color coded by corresponding the circulation branch.

1.5.3 Correction of Apparent Spreading Velocities/Correcting for Mixing

The velocities calculated from $^3H/^3He$ ages along the Atlantic water pathways are not the same as the actual advective velocities because the tracer velocities are shifted by the effects of mixing. (Wallace et al., 1992; Schlosser et al.,1995). Entrainment of older waters from the basin interiors systematically increases the $^3H/^3He$ ages in the boundary current and major circulation

branches, which makes the apparent (tracer) velocities slower. In addition, the impacts of mixing are non-linear, so that conceptual and/or numerical modeling is required to quantify corrected velocities from the apparent ones. In this contribution, we apply a unique correction factor to the apparent velocities along the boundary current and across different circulation branches. Specifically, we refer to the correction factor derived from direct velocity measurements and model outputs (Woodgate et al., 2001; Polyakov et al., 2005; Dmitrenko et al., 2008; Mauldin et al., 2010; Polyakov et al., 2010). To correct the $^{3}H/^{3}He$ apparent velocity for the effects of mixing for the BSBW along the continental slope and the western side of the Lomonosov ridge, Mauldin et al. (2010) model the Arctic Ocean boundary current from the Santa Anna Trough as a leaky pipe. The authors found an apparent spreading rate of 0.9 ± 0.2 cm s^{-1}; and a modeled velocity of 2.5 ± 0.5 cm s^{-1}. The resulting correction factor is 2.78 ± 0.83. The error (ε_i^{corr}) for each corrected velocity (v_i^{corr}) is calculated as the square root of the sum of the fractional error of the apparent velocity ($\varepsilon_i^{app}/v_i^{app}$) and the correction factor fractional error. I.e., $\varepsilon_i^{corr} = v_i^{corr} \cdot \sqrt{\left(\varepsilon_i^{app}/v_i^{app}\right)^2 + (0.83/2.78)^2}$.

Applying the same correction factor to both branches and to circulation branches away from the continental slope is a first-order approximation: renewal and mixing rates are not constant with depths, nor are the same along the boundary current and the basin interior (Smethie et al., 2000). This correction has limits but also strength in its simplicity as it allows us to compare tracer-derived current velocities with the available direct current measurements and simulated rates. For instance, mooring measurements support that mixing in the boundary current is faster near the Lomonosov Ridge where the flow splits into two branches (Woodgate et al., 2001). The corrected velocity values for FSBW and BSBW are summarized in Tables 2 and 3. After correcting for mixing, the FSBW mean velocity along the boundary current is 2.42 ±

0.87 cm s^{-1}. The corrected velocities east and west of the Lomonosov Ridge are 3.53 ± 1.75 cm s^{-1} (EBBC) and 1.97 ± 0.77 cm s^{-1} (CBBC) respectively. The corrected spreading rate for BSBW along in the EBBC is calculated to be 1.85 ± 0.79 cm s^{-1}; and 2.06 ± 0.76 cm s^{-1} in the CBBC. Using these corrections, it takes the FSBW 14.7 ± 5.2 years to complete the entire loop along the Arctic Ocean basins following the continental slope (1000 m isobath) for ca. 10500 ± 1500 km. FSBW reaches the Laptev Sea in approximately 2.8 ± 1.4 years; and returns to Fram Strait in ca. 7.4 ± 3.0 years along the Amundsen Basin side of the Lomonosov Ridge (LRAB); and in 9.0 ± 4.4 years along the Gakkel Ridge. It takes BSBW 13.5 ± 4.6 years to complete the circumpolar boundary current loop from the Santa Anna Trough to Fram Strait (ca. 8640 ± 1100 km).

The wide spread of apparent ages at similar distances suggest that the spreading rates might vary across individual circulation branches. Thus, we separated the correlations by circulation branch. As a result, the overall age/distance correlation could be broken down into a set of distinct correlations for the individual circulation branches with different and statistically significantly slopes (Figures 5 and 6). Spreading rates for the individual circulation branches computed for FSBW and BSBW are presented in Tables 2 and 3.

1.5.4 Dynamical Considerations

The basic structure of the Atlantic Water circulation in the Arctic Ocean regime is that of a robust cyclonic boundary current following the continental shelves and submarine ridges, with faster velocities observed along the boundary currents along the continental slope. The flow is largely barotropic below the halocline with most of the vertical shear provided by the halocline slope (Spall, 2013). While flow motions of the mixed layer and upper halocline are dominantly forced by surface stress, the Atlantic Layer is too deep in the water column to be directly influenced by shear stresses generated by winds and sea ice motions. Rather, horizontal pressure gradients must drive these branch currents, either from sea-surface height gradients or from

density gradients caused by thermohaline processes, such as the salinity contrast between the saline Atlantic inflow and freshwater from a variety of sources are ultimately responsible for establishing and maintaining the circulation of FSWB and BSBW (Spall, 2013). Spall (2013) demonstrated that the Atlantic boundary current along the continental slope can be derived from addition of freshwater over the shelf seas.

Notwithstanding that the notion the Atlantic waters flowing as a topographically guided, cyclonic boundary current following the continental shelf was introduced at the onset of Arctic oceanographic expeditions and repeatedly confirmed by later studies, the understanding of the AW advective pathways in the interior and along secondary flow paths is still primitive and largely not validated by direct observations (Smethie et al., 2000; Aksenov et al., 2011). The dominating effect of the underlying topography on the Atlantic Water flow propagation in the Arctic Ocean has been reported in numerous contributions, and yet its driving forces and mechanism have not yet been fully understood (Holloway, Smethie et al., 2000; Shimada et al., 2004; Aksenov et al., 2011).

Numerous experimental and modeling studies have linked the predominantly cyclonic circulation in the Atlantic Layer around the Arctic basins to the potential vorticity (PV) influx from the surrounding shelf seas, such as the BSBW inflow at the Santa Anna Trough (e.g., Woodgate et al., 2001; Yang, 2005; Karcher et al., 2007). Holloway (1987) identifies the eddy-topography interactions as a major source of PV and a driver of the boundary current mean flow, with a strength comparable to wind or thermohaline forcing (Nazarenko et al., 1998; Polyakov, 2001; Holloway, 2004). It is postulated that in a semi-enclosed ocean, such as the Arctic Ocean, the balance between the net PV inflow and its dissipation along the boundary current determines the direction of rotation of the flow (Yang, 2005). According to the principle of conservation of

potential vorticity, signals are advected along contours with a constant ratio between the Coriolis parameter and water depth. In the Arctic Ocean it is safe to assume the Coriolis parameter to be constant. Thus, the principle of conservation of potential vorticity provides a first-order dynamical explanation of fact that the flow at all depth levels is directed parallel to bathymetric contours, so that 'rim' currents appear, following slopes and ridges. While balance of lateral potential vorticity influx and dissipation by cyclonic boundary currents in the Eurasian Basin can explain a large part of the flow regime, other factors, external and internal, can play a role for the Atlantic Water circulation in the Arctic Ocean. For instance, seasonal winds can move the center of the boundary current both toward and away from the continental shelf (Dmitrenko et al., 2008). Several studies have postulated a partial coupling/interaction between the Beaufort Gyre and the Atlantic flow in the Canada Basin (Karcher et al., 2012). According to this theory, an intensified (weaker) anti-cyclonic flow in the Beaufort Gyre, tends to weaken (intensify) the cyclonic Atlantic flow (Karcher et al., 2007).

Vertical mixing is another physical parameter that can significantly affect the Arctic Ocean boundary current by changing the water stratification which in turn affects the PV of inflowing waters. Zhang and Steele (2007) examine the relevance of vertical mixing in affecting the direction of rotation of the AW by altering the vertical distribution of salinity and ultimately the strength of local stratification. The authors use an ice-ocean model from the AOMIP sets to study how different vertical mixing schemes in numerical models generate diverging circulation scenarios for the Atlantic Layer.

1.5.5 Comparison with Previous Studies

We discuss our tracer-derived velocities in the context of mooring-based data from current meters and profiling devices (Woodgate et al., 2001; Pnyushkov et al., 2015; Nikolopoulos et al., 2009; Newton & Sotirin, 1997), estimates from propagation of warm

temperature anomalies and hydrographic fronts (Polyakov et al., 2005; Dmitrenko et al., 2008; Shimada et al., 2004; Woodgate et al., 2007), and model-generated flow speeds along the boundary current (Karcher et al., 2003; Holloway et al., 2007; Aksenov et al., 2011; Karcher et al., 2012; Pnyushkov et al., 2013) (Table 4). When comparing the tracer-derived velocities with other direct observations and anomaly propagation estimates, it is important to consider that these methods capture different components of the flow. Transient tracers and anomaly propagations can be represented as dye-release experiments (Lagrangian measurements) with a large number of drifting elements without identifiers (molecules). Current meters and profilers provide time series of the velocity at fixed geographic locations (Eulerian measurements).

Direct Observations and Anomaly Propagations

First, we compare the tracer-derived spreading rates with previously published velocity data at the continental slope of the Eurasian and Canadian Basins and along the Amundsen Basin returning branch off the Lomonosov Ridge (Figure 7). The mooring data used in this contribution were collected between 1995 and 1997 (Woodgate et al., 2001; Newton & Sotirin, 1997) and from 2002 to 2011 (Dmitrenko et al., 2008; Pnyushkov et al., 2015; Nikolopoulos et al., 2009). Along-slope velocity data from direct measurements are expressed as long-term mean current flows derived by averaging time series of the Atlantic core (FSBW) properties and produced by a variety of instruments: (1) Acoustic Doppler Current Profilers (ADCPs); (2) Acoustic Travel-Time Current Meters (ACMs); (3) McLane Moored Profilers (MMPs), and (4) Recording Current Meters (RCMs). Standard errors of mean current speeds among all the instruments range from 0.3 to 1 cm s^{-1}; and uncertainty in current direction is ca. ± 2º to 3º. The majority of the available velocity observations were obtained along Eurasian Basin margin: out of the 11 moorings used in our comparisons only 3 are located in the Canadian Basin and two

away from the continental slope and along the Lomonosov Ridge. Thus, we restrict the comparisons to the FSBW flow in the boundary current and the returning flow along the Lomonosov Ridge, corresponding to the following circulation branches: EBBC, CBBC, and LRAB.

The intensity of the Atlantic boundary current experiences large variability at seasonal, inter-annual, and decadal time scales. In our comparison, it is necessary to consider that a strong seasonal signal and year-to-year modulation introduce uncertainty to the mean current speeds used in our velocity comparisons. In the Eurasian Basin the seasonal cycle amplitude ranges from ca. 10 cm s^{-1} northeast of Fram Strait to ca. 3 cm s^{-1} at the Laptev Sea slope, where it accounts for 70% of the measured mean current speed (Pnyushkov et al., 2015). For instance, two 1-year long records for the FSBW velocity measured at the same location on the Laptev Sea slope (79.9 ºN and 142.35 ºE) during the periods of September 2004–2005 and September 2005–2006 ranged from 3 to 6 cm s^{-1} (Dmitrenko et al., 2008; Pnyushkov et al., 2015).

Typical velocities measured in the Atlantic Layer of the Arctic Ocean are of the order of 2–5 cm s^{-1} (e.g., Woodgate et al. 2001, 2007; Pnyushkov et al., 2015). Current velocities above 20 cm s^{-1} are observed at the two sites close to the injection point into the Eurasian Basin. They are the result of strong density gradients across the eastern flanks of Fram Strait and the St. Anna Trough. Mooring-based observations from Fram Strait and Svalbard show a much stronger current intensity with maximum speeds of O (22–24 cm s^{-1} at 220–250 m) (Ivanov et al., 2009; Pnyushkov et al., 2015). Similarly, there is evidence of velocities of O (17–22) cm s^{-1} for BSBW inflow at the Santa Anna Through (Dmitrenko et al., 2015). Repeated measurements support an FSBW velocity decreases by more than 5-fold from north of Fram Strait to the Laptev Sea, from 22 ± 2 cm s^{-1} to 4 ± 2.5 cm s^{-1} (Pnyushkov et al., 2015). The sharpest reduction in FSBW

velocity occurs between Svalbard and Franz Joseph Land, where the measured current slows from ca. 20 cm s^{-1} to 8 cm s^{-1} over less than 1000 km. This weakening of the FSWB flow has been addressed by several studies that have correlated it to an increase of the baroclinic component of the flow in the boundary current (Pnyushkov et al., 2015) and to the notion of a progressive propagation speed decrease at higher latitudes (Swift et al., 1997), but it is outside the scope of this contribution.

Direct velocity measurements at the Laptev Sea slope, spanning a distance of roughly 1500 km, range from 2.2 to 6.0 cm s^{-1}. When calculating the average all the available mooring-based data for the Eurasian boundary current (EBBC), from Franz Joseph Land to the eastern Laptev Sea, we obtain a mean velocity of 4.45 ± 1.9 cm s^{-1} (12 ± 2.4 cm s^{-1} if including velocity data from Fram Strait and Svalbard). This is in reasonable agreement with our results of 3.53 ± 1.75 cm s^{-1}.

Along the Canadian Basin continental shelf, the mooring sites are sparser with only three locations: from west to east, the first one is located off the eastern flank of the Lomonosov Ridge (JAS 1995–1996, Woodgate et al., 2001), the next along the southern Canada Basin slope (July 2002–September 2004, Nikolopoulos et al., 2009), and the last in the Switchyard Region (April 1991–Apr 1992, Newton and Sotirin, 1997). Besides providing observational evidence for the mean along-slope current velocity, current meter measurements along the Canadian Shelf support the presence of a well-structured, cyclonic boundary current that is continuous around the Arctic Ocean basins.

Current meter velocity data for the AW along the Canadian Basin Boundary Current (CBBC), range from 2.7 to 4 cm s^{-1}, corresponding to a mean along-slope velocity of 3.2 ± 1.9 cm s^{-1} (Woodgate et al., 2001; Nikolopoulos et al., 2009; Newton & Sotirin, 1997). The tracer-

derived velocity for the CBBC is 1.97 ± 0.95 cm s^{-1}. Overall, the averaged velocity from direct measurements along the Arctic Ocean circumpolar boundary current, from Franz Joseph Land to the Switchyard Region is 3.4 ± 2.5 cm s^{-1}. This compares reasonably well with our value of 2.45 ± 0.90 cm s^{-1}. Lastly, the mean velocity from moorings data at the eastern side of the Lomonosov Ridge is 1.6 ± 0.9 cm s^{-1} (Pnyushkov et al., 2015; Woodgate et al., 2001). This compares favorably the tracer-derived speed of 1.7 ± 0.91 cm s^{-1}. Notably, our results are in agreement with direct measurements in supporting lower velocities in the Canadian Basin than in the Eurasian Basin. Woodgate et al. (2001) observed that velocities in the boundary current slow down after the current bifurcation at the junction of the Lomonosov Ridge with the continental margin. In the 20th Century the AW inflow at Fram Strait into the Arctic Ocean has exhibited large decadal variability, with alternating warming and cooling periods recorded in the 1930s-40s and 1960s-70s, respectively (Polyakov et al., 2004). During the early 1990s and mid 2000s, positive temperature anomalies of up to 1.7 ºC (compared to the 1970s climatology) were measured in the West Spitzbergen Current in the Norwegian Sea, in the branch crossing Fram Strait, and later observed further east along the Eurasian and Canadian Basin slopes (Quadfasel et al., 1991; Morison et al., 1998; Polyakov et al., 2005; Ivanov et al., 2009; Polyakov et al., 2010). Swift et al. (1997) propose that the warm anomalies in the AW which penetrate the Arctic Ocean through Fram Strait can be treated as tracers advected along the boundary current. Numerous studies obtained velocity estimates for the boundary current from tracking AW warm pulses propagating eastward along the continental margins of the Eurasian and Canadian Basins (e.g., Frank et al., 1998; Shimada et al., 2004; Polyakov et al., 2005; Dmitrenko et al., 2008).

Polyakov et al. (2005) estimate a travel time of 4.5 to 5 years for the 1990s warm temperature anomaly from Fram Strait to the western side of the Lomonosov Ridge. These travel

times for the FSBW compares favorably with the mean FSBW $^{3}H/^{3}He$ age differences calculated from stations in the same region of 5.2 years (range: 4–6.4 years). Dmitrenko et al. (2008) calculated that the early 2000s Atlantic Water warm pulse penetration rate between two moorings at the Laptev Sea slope margins (ca. 400 km apart) was ca. 2.2–2.7 cm s^{-1}, significantly faster than the 1.5 ± 0.6 cm s^{-1} estimated by Polyakov et al. (2005). Both results are consistent with the EBBC speed of 3.52 ± 2.13 cm s^{-1} we obtain.

Table 4. Comparison of Atlantic Layer velocity estimates from this and different studies.

Study	Velocity (cm s-1)	Water Mass	Methods	Circulation Branch	Region
This study	3.52 ± 1; {1.97 ± 1}	FSBW	Transient tracers	EBBC; {CBBC}	Arctic Ocean Boundary Current
This study	1.85 ± 1; {2.08 ± 1}	BSBW	Transient tracers	EBBC; {CBBC}	Arctic Ocean Boundary Current
Frank et al. (1998)	1	FSBW	Transient tracers	EBBC	Laptev Sea
Frank et al. (1998)	2	BSBW	Transient tracers	EBBC	Laptev Sea
Mauldin et al. (2010)	2.5 ± 0.5	BSBW	Transient tracers	EBBC/LRRB	Santa Ana Trough to Chukchi Sea
Pnyushkov et al. (2015)	20–22	FSBW	Current meters	EBBC	Fram Strait - Svalbard
Pnyushkov et al. (2015)	10 ± 1	FSBW	Current meters	EBBC	Franz Josef Land
Pnyushkov et al. (2015)	4 ± 1	FSBW	Current meters	EBBC	Laptev Sea
Woodgate et al. (2001)	5.4 ± 0.6	FSBW	Current meters	EBBC	Laptev Sea
Dmitrenko et al. (2008)	3.3 ± 0.7	FSBW	Current meters	EBBC	Laptev Sea
Pnyushkov et al. (2015)	5 ± 1	FSBW	Current meters	EBBC	Laptev Sea
Woodgate et al. (2001)	2.7 ± 0.7	FSBW	Current meters	CBBC	Continental slope east of Lomonosov Ridge
Woodgate et al. (2001)	1.3 ±0.9	FSBW	Current meters	LRRB	Lomonosov Ridge -Western flank
Pnyushkov et al. (2015)	2 ± 0.3	FSBW	Current meters	LRRB	North Pole
Nikolopoulos et al. (2009)	3 ± 1	FSBW	Current meters	CBBC	Beaufort Sea
Newton and Sotirin (1997)	4 ± 1	FSBW	Current meters	CBBC	Lincoln Sea
Shimada et al. (2004)	2.1 ± .6	FSBW	Anomaly propagation	AOBC	Fran Strait to Canadian Slope
Polyakov et al. (2005)	1.5 ± 0.5	AW	Anomaly propagation	EBBC	Fran Strait to Laptev Sea
Woodgate et al. (2007)	1.5 ± 0.25	AW	Hydrogr. front advection	CBBC	Chukchi Borderland
Dmitrenko et al. (2008)	2.4 ± 0.2	AW	Anomaly propagation	EBBC	Laptev Sea to East Siberian Sea
Aksenov et al. (2011)	2–10	AW	OCCAM[a]	EBBC	Fram Strait to Lomonosov Ridge
Aksenov et al. (2011)	4–6	AW	OCCAM[a]	CBBC	Lomonosov Ridge to Lincoln Sea
Karcher et al. (2002)	1.0	AW	OPYC[b]	EBBC	Nansen Basin
Karcher et al. (2007)	2.4–2.8	AW	AWI[c]	AOBC	Arctic Ocean Boundary Current
Karcher et al. (2007)	1.4–2.2	AW	LANL[d]	AOBC	Arctic Ocean Boundary Current

[a]Ocean Circulation and Climate Advanced Model (OCCAM) (Killworth et al., 1991).[b]Ocean Isopycnic Model (OPYC) (Oberhuber, 1993). [c]Regional NAOSIM developed at the Alfred Wegener Institute (Gerdes et al., 2003).[d]Global version of the POP−CICE model developed at the Los Alamos National Laboratory (Hunke and Holland, 2007).

Tracking the penetration of the 1990s warm pulse into the Canadian Basin, Shimada et al. (2004) estimate a period of ca. 10–13 years for the warmer FSBW to reach the Canadian slope, east of the Chukchi Borderlands, approximately equivalent to a speed of ca. 1.8–2.2 cm s^{-1}. This is in reasonable agreement with the mean tracer apparent age of 14.7 (range: 10.3–17.4) years we derive from our data. As discussed in a previous section, there are several possible pathways the Atlantic Water can follow around and south of the Chukchi Plateau, namely through the Chukchi Gap or north of the Chukchi Plateau and the Northwind Ridge. This introduces additional uncertainty in the spreading rates estimates due to the difference in time scales along the different pathways. Woodgate et al. (2007) estimate an average current speed of 1.5 ± 1 cm s^{-1} for Atlantic Water flow by tracking thermohaline intrusions over the regions of the Mendeleev Ridge and Chukchi Borderland. Shimada et al. (2004) estimate a propagation time of 10 to 13 years for the 1990's warm temperature anomalies to penetrate to the eastern Canadian Basin, east of the Northwind Ridge, along the continental ridge. The CBBC velocity estimate obtained from this travel time is 1.8–2.2 cm s^{-1}. Both results are in good agreement with our CBBC velocity estimate of 1.97 ± 0.77 cm s^{-1}.

Models

Most models can consistently simulate the major features of the Arctic Ocean circulation, such as the continuous cyclonic boundary current along the continental margins of the Eurasian and Canadian Basins (e.g., Holland et al., 1996; Karcher & Oberhuber, 2002; Karcher et al., 2003; Karcher et al., 2007; Aksenov et al., 2011). Yet, they still cannot realistically reproduce the finer structure of the returning circulation branches tracking the Gakkel and Alpha-Mendeleev Ridges, nor can they provide information on the different time scales along these secondary pathways. There still are discrepancies among model outputs, as well as between

model and observations (Holloway et al., 2007; Karcher et al., 2012). Different physical parametrizations are a contributing factor in these discrepancies. For instance, there are substantial differences in boundary current strength and large-scale sense between outputs generated by models implementing the traditional 'frictional' eddy parameterization and those from models adopting the 'Neptune Effect' (Holloway, 1996; 2004). According to the 'Neptune Effect', eddies act to propel the mean flow in correspondence of relatively steep topography, rather than to damp it (the mean flow) as assumed in the traditional friction parametrization (Nazarenko et al., 1998; Holloway, 2004). The PV-induced boundary current flow is further enhanced by the 'Neptune effect' parameterization (Holloway et al., 2007; Holloway & Wang, 2009). 'Neptune' models generate faster, more structured cyclonic boundary currents, that are consistently cyclonic in the Eurasian and Canadian Basins in agreement with the Rudels' cyclonic gyres and our results.

As shown by the Arctic Ocean Model Intercomparison Project (AOMIP) experiments, even models implementing identical forcing ensembles produce significantly different pictures of the Arctic Ocean mean hydrographic properties and circulation structure (Karcher et al., 2007; Holloway et al., 2007). AOMIP models apply the same forcing fields but differ in model grid spacing/resolution. An important parameter to consider in the context of ocean simulations is the ratio between the model resolution to the local Rossby radius, which determines the average eddy size. As a general rule, to properly resolve eddies the ratio needs to be less than or equal to 0.5 (e.g., a minimum of two grid points per eddy); and between 0.5 and 1 to permit them (Hecht & Smith, 2008). For reference, the typical best resolution in oceanic general circulation models (OGCMs) is ca.10 km (or 1/10º). Eddy-resolving models do no longer need parameterization thus further improving consistency across simulations (Hallberg, 2013). In the Arctic Ocean, the

Rossby radius ranges from ca. 5 km in the Nansen Basin to ca. 15 km in the interior of the Canadian Basin, and it is typically 7 km at the continental slope (Nurser & Bacon, 2014). Therefore, a 1/12º (ca. 9 km) model can resolve eddies in large regions of the Arctic Ocean, but not everywhere. This might explain why numerical simulations are able to capture the cyclonic boundary current at the continental slope and to partly replicate the basin-wide cyclonic gyres, such as the returning circulation branch along the Lomonosov Ridge, but not the smaller scale flow along submarine ridges. Experiments indicate that eddy-resolving models produce more realistic simulations of the Arctic circulation not only than coarser-resolution 1º models can but also than eddy-permitting (1/4º) models (Merryfield & Scott, 2007; Maslowski et al., 2008; Aksenov et al., 2011).

Given the topographically-guided nature of the AW circulation in the Arctic Ocean and the notion that eddy–topography interactions effectively enhance the boundary current, the quality and resolution of the input bathymetric data are crucial to improve the model skills. Unfortunately, there are still large observational gaps in our knowledge of the AO bathymetric features. Using a high-resolution (1/12^{o}) global Ocean Circulation and Climate Advanced Model (OCCAM: Killworth et al., 1991) Aksenov et al. (2011) replicate the continuous cyclonic flow around the whole Arctic periphery and calculate velocities in good agreement with direct measurements. The modeled velocities in the Eurasian Basin range from 14 to 4 cm s^{-1}, with the fastest currents (8–14 cm s^{-1}) close to of Svalbard and the slowest values (4–6 cm s^{-1}) at the Siberian Shelf, (Table 4).

Over the Canadian Basin, the simulated velocities range from 4 to 7 cm s^{-1}. The study also estimates a seasonal cycle of 2 to 4 cm s^{-1}, with stronger flow during the winter months. The FSBW potential temperature distribution derived by Aksenov et al. (2011) shows remarkable

similarities to our results, presented in Figure 3a. It captures the upper branch progressive cooling downstream Fram Strait along continental slope, a marked temperature gradient across the Lomonosov Ridge, as well as a warmer tongue in the central Eurasian Basin indicating recirculation and the current branching at the Lomonosov Ridge. The modeled temperature structure for the BSBW displays a sharp temperature difference between the Eurasian and Canadian Basins, in disagreement with our multi-year average that indicates a much more uniform distribution/weaker modifications for the deeper Atlantic branch. The authors also present a picture of the general circulation pathways derived from a novel application of Montgomery function analysis. Notably they are able to represent the interactions with the underlying bathymetry around the Chukchi Plateau and partly capture the branching of the boundary current at the Lomonosov Ridge, Alpha-Mendeleev Ridge.

Spall (2013) shows that the large-scale characteristics of the Atlantic Water cyclonic boundary current can be predicted by a numerical model only using the density gradients between the Atlantic Water and the freshwater coming off the Arctic shelves. The study produces a modeled velocity for the AW inflow at Fram Strait (eastern side) of 4–10 cm s^{-1} and is associated with a net northward transport of 5.6 Sv (Spall, 2013).

Kelly et al. (2018) use a high resolution ocean model (1/12º Nucleus for European Modelling of the Ocean NEMO, Madec (2014)) combined with a Lagrangian particle-tracking experiment to study the advective trajectories and time scales of a potential pollutant release/oil spill in the Arctic Ocean. Interestingly, the simulation not only confirm the well-known circulation pattern of a narrow well-structure eastward boundary current, but also replicate the flow branching at the Lomonosov Ridge and produce advective rates along the Eurasian shelf break (Severnaya Zemlya, Laptev Sea, New Siberian Island) approximately twice as fast as those along the

Canadian continental slope (East Siberian Sea-Chukchi Shelf). The velocities obtained from the modeled distances traveled by the Lagrangian particles in two years range from 1.13 ± 0.64 cm s^{-1} (Canadian Basin) to 2.16 ± 1.52 cm s^{-1} (Eurasian Basin) (Kelly et al., 2018). For comparison, the velocities along the CBBC and EBBC calculated in this study are 1.97 ± 0.77 cm s^{-1} and 3.53 ± 1.75 cm s^{-1} respectively.

1.6 Conclusions

In our analysis we combined $^{3}H/^{3}He$ age data collected between 1987 and 2013 to address circulation patterns and mean spreading rates of Atlantic waters in the Arctic Ocean. The ages reveal new information on AW circulation patterns and spreading velocities, independently corroborating the previously estimated circulation schemes, and adding a time dimension to the analysis of the circulation patterns. Tracer data suggest that the Atlantic waters follow topographic slopes cyclonically (anticlockwise) around the continental slope and along the ocean ridges, with the core of the current lying between the ~500-1000 m isobaths. Mean spreading velocities differ considerably between the individual branches of the overall circulation pattern.

The average apparent spreading velocity for the FSBW calculated from the $^{3}H/^{3}He$ data is 0.87 ± 0.17 cm s^{-1} (R^2 = 0.89), with a range of ca. 0.2 to 1.3 cm s^{-1} depending on the individual branch of the circulation pattern. The average apparent spreading velocity for the deeper branch, BSBW, is 0.68 ± 0.14 cm s^{-1} (R^2 = 0.75) and varies from ca. 0.2 to 0.9 cm s^{-1} across the different circulation pathways. Our data indicate that the general circulation patterns and mean spreading velocities of the Atlantic inflow/branch waters have been relatively stable between 1987 and 2013 despite observational evidence of dramatic changes in the upper Arctic Ocean over the same period. Preliminary analysis of transient tracer data from the 2015 U.S. Arctic GEOTRACES (GN01) reoccupations of the Oden section in 2005 and the Arctic Ocean Section

in 1994 of the Canadian Basin indicates a shift towards longer residence times (i.e., the mean $^{3}H/^{3}He$ apparent ages are 9 to 12 years older in 2015) in the Atlantic layer at stations along the boundary current but no significant changes away from the continental shelf (e.g., at the North Pole and along the Alpha Mendeleev Ridge. Manuscript in preparation). Future measurements will show if this deviation is an anomaly or a long-term trend.

Chapter 2: Circulation Pathways and Spreading Rates of the Halocline Waters in the Arctic Ocean Derived from Three Decades of Tritium/^{3}He Observations

2.1 Introduction

Because of the large river discharge entering the Arctic Ocean, its surface is characterized by a thin layer of fresh, cold waters. Below this well-mixed layer, salinity steeply increases from ca. 32 to eventually match the AW values. This is the halocline: a strongly stratified layer effectively constrains the vertical heat flux between the Atlantic layer and the surface sea ice (Rudels et al., 1996). Although about one order of magnitude less than the atmospheric heat, the oceanic heat advected by Atlantic waters would be enough to melt the current Arctic sea ice without the insulation barrier effected by the halocline (McPhee et al., 2003; Polyakov et al., 2017). This heat source has not been considered a major driver of sea ice reduction, as a stably stratified halocline has so far prevented ventilation of the Atlantic layer, effectively separating it from the sea ice cover, and restricting the heat flux to the sea ice cover to ca. 3 to 5 W m^{-2} (Aagaard et al.,1981).

We present ^{3}H/^{3}He and hydrographic data from 21 expeditions spanning 26 years of Arctic Ocean section work (1987 and 2013). The temporal extent of our dataset is particularly valuable as it provides us with a tool to investigate whether there are observable changes in the Arctic Ocean stratification, general circulation patterns, and spreading rates in halocline layer, a critical heat flux barrier between the AW and the sea ice.

Transient tracer data are used to independently establish circulation pathways and estimate the apparent spreading velocities and mean residence times for the upper halocline

water (UHW) and the lower halocline water (LHW). The results are discussed in the context of the temporal stability of the circulation, stratification stability, and water mass composition in the Arctic Ocean, as well as regional variability of spreading velocities along individual branches of the circulation pattern due to topographic and dynamic forcing.

2.2 Hydrography

Both the northern Atlantic and Pacific Oceans are connected and exchange waters with the Arctic Ocean, which acts as a passage between the two major oceans. These fluxes are of great importance for the oceanic heat, freshwater, and nutrients budgets and distributions in the Arctic. Atlantic waters enter the Eurasian Basin as two separate branches from the Greenland Sea via the Fram Strait (2-3 Sv) and the Barents Sea through the Santa Anna Trough (1-3 Sv) (e.g., Rudels et al., 1994; 1996). The North Atlantic Ocean is the major source of oceanic heat into the Arctic Ocean with an annual net heat inflow via Fram Strait averaging 40 TW (relative to the reference temperature of 0 ºC; Beszczynska-Möller et al., 2012). The heat carried by the Atlantic layer into the Arctic Ocean would be sufficient to melt several meters of Arctic sea ice if it reached the surface (Rudels et al., 1996, 2004; Steele and Boyd, 1998; Polyakov et al., 2020).

The Pacific inflow into the Arctic Ocean occurs via Bering Strait and is driven by a constant steric height gradient (ca. 0.7 m) with the Northern Pacific (Aagaard et al., 2006). This input is highly seasonal, vary on an interannual timescale, and ranges between 0.7 and 1.2 Sv (Woodgate et al., 2018). Pacific waters (PW) are both significantly fresher (PW: S ~ 32.5; AW: S ~ 34.92) and richer in nutrients than the Atlantic originated waters thus playing an important role in defining the Arctic water column stratification and its biological activity (e.g., Codispoti et al., 2013). Pacific inflow carries a substantial amount of oceanic heat, 13 TW; contributes to ca. 30% of the total freshwater influx, (2500-3250 km^3 yr^{-1}) (Haine et al., 2015; Carmack et al.,

2016); and provides the major nutrient input to the polar regions (Walsh et al., 1989; Woodgate and Aagaard, 2005). Asides from these two oceanic inflows, the other inputs to the Arctic are volumetrically small but account for 70% of the total freshwater inflow: riverine discharge (4200 ± 420 km^3 yr^{-1}) and net precipitation (2200 ± 220 km^3 yr^{-1}) (Haine et al., 2015).

The Arctic Ocean stratification primarily controlled/determined by salinity, is quite stable and mostly constrained to the upper 500 meters. A surface, well-mixed layer of cold freshwater occupies the 10 to 20 meters of the Arctic Ocean. This buoyant, thin layer contains a up to 25% of the total water column freshwater content, is largely wind-driven and closely correlated to river runoff signal and sea ice dynamics. Its mean thickness and salinity show a strong seasonal cycle and vary considerably across the Arctic Ocean basins. Typically, the surface mixed layer is twice as deep in ice-free regions compared to sea ice covered areas. Its depth is also correlated to the strong seasonality of the discharge of freshwater into the Arctic Ocean from the Russian and Northern American rivers. Throughout the Arctic, a steep salinity-driven pycnocline insulates the surface from the warm Atlantic layer. This is the Arctic haloclines. The halocline is roughly three times as thick as the polar mixed layer and extends to ca. 250 m depth (Rudels et al., 2004). The upper halocline is centered at the salinity surface of 33.1 and is characterized by a nutrient maximum and temperatures close to the freezing point (Anderson et al., 1994). In the lower halocline nutrient concentrations reach a minimum, salinity increases to 34.2 ± 0.1, and temperatures rise well above the freezing point (Anderson et al., 1994). Halocline sources vary across the Arctic Ocean. In the Canadian Basin, fresh Pacific waters are found below the mixed layer. Below the Pacific layer, Atlantic Waters form a temperature maximum (up to ~ 1-1.2ºC) at depths of around 200-400m. In Eurasian basin, where the Pacific waters are virtually absent, the Atlantic layer is separated from the surface by a cold, halocline layer, which is formed by either

brine-rejection-driven convection or injection of cold salty shelf waters. Intermediate, deep waters found below the Atlantic layer are colder and saltier than waters above, and virtually isolated from the surface. They are remarkably homogeneous and hundreds of years old (Schlosser et al., 1999). Despite the lack of topographic obstructions, intermediate water hydrographic properties are not uniform between the two basins but show a clear front at the Lomonosov Ridge. This feature can be explained by different exchange rates between the intermediate and Atlantic waters and faster ventilation occurring in the Eurasian Basin.

The circulation of the surface Arctic Ocean is characterized by three major circulation patterns: thew Trans-Polar Drift stream, the Beaufort Gyre, and the Arctic Ocean circumpolar boundary current. The first two are driven by horizontal gradients of wind stress and affect the surface layers thus playing a major role in organizing the freshwater distribution and export (e.g., Hunkins & Whitehead, 1992; Newton et al., 2006, 2008; Jahn et al., 2010; 2012). The last one is the predominant cyclonic flow observed in the Atlantic layer.

On average, a horizontal sea-level pressure difference is observed between the western and east1ern Arctic Ocean, with a region of high pressure centered over the Canadian Basin and low pressures found over the Eurasian Basin. The resulting surface wind fields control the long-term, large-scale average sea ice transport and surface layer currents: an anticyclonic circulation cell, the Beaufort Gyre, and a cyclonic circulation in the Siberian Arctic which converges off the East Siberian Sea to form the Trans-Polar Drift, a stream of sea ice and freshwater directed toward Fram Strait (Rudels et al., 2012). After crossing Bering Strait Pacific waters follow three primary flow paths: (1) eastward along the Alaskan continental slope as a cyclonic boundary current;(2) northward toward Siberia and then to Fram Strait across the central Arctic parallel to

the Trans-polar Drift; (3) and the anti-cyclonic flow around the Beaufort Gyre (Jones et al., 1998; Steele et al., 2004; Aksenov et al., 2016).

The pathway of the Atlantic layer as a cyclonic boundary current is well established and documented by current meter measurements, hydrographic and tracer data (e.g., Timofeyev, 1957; Coachman and Barnes, 1963; Rudels et al., 1994). Atlantic waters flow cyclonically along the continental slope and major submarine ridges of the Arctic Ocean as a persistent, topographically steered circumpolar boundary current before exiting via Fram Strait (Timofeyev, 1957; Coachman and Barnes, 1963; Rudels et al., 1999; Woodgate et al., 2001). Holloway (1987) identifies the eddy-topography interactions developing at sloping bathymetric surfaces as the primary driver of the boundary current mean flow and compares its strength to that of surface stress or thermohaline forcing.

While modified Atlantic waters are traced in every Arctic basin, mainly along the continental slope and the eastern flanks of submarine ridges, Pacific Waters are largely constrained to the Canadian Basin. Indeed, the presence or absence of Pacific waters is the major difference between upper waters of the western/eastern Arctic basins (Jones et al.,2003; Woodgate et al., 2005;). Several studies linked the location of the front separating Atlantic and Pacific waters with that of the Transpolar Drift stream (e.g., Morison et al., 1998, 2012). Historically the Atlantic/Pacific front has shift moved between an alignment with the Lomonosov Ridge and one with the Mendeleyev Ridge.

Apart from the difference in their average salinity ranges the UHW and LHW can also be differentiated by their principal ventilation sources with the former being primarily derived from Pacific waters and the latter from Atlantic-origin waters (Coachman & Barnes, 1961; Jones & Anderson, 1986; Rudels et al., 2004). Rudels et al. (2004) conclude that a substantial fraction of

lower halocline waters in the Canadian Basin derive from modifications of Atlantic-origin waters. With the influence of FSBW being more pronounced in the in Makarov Basin and that of the BSWB dominating between the Mendeleyev Ridge and the Chukchi Cap. Since Pacific waters are significantly fresher than the Atlantic-origin waters, they flow on top of the Atlantic layer (300 m), feeding the upper halocline layer and strengthening the density insulation from the heat flux in the Canadian Basin.

The mean residence times of the different Arctic water masses can be estimated by using selected combinations of tracers. $^{3}H/^{3}He$ ages and CFC data are used to determine the residence times of surface and intermediate waters (e.g., Wallace et al., 1987, 1992; Schlosser et al., 1994, 1995; 1999; Frank et al., 1998; Smethie et al.,1999; Mauldin et al., 2010). Below 2000 m the $^{3}H/^{3}He$ ages and CFC $^{3}H/^{3}He$ dating methods lose their efficacy, thus ^{14}C and ^{39}Ar data are used to determine the residence time for the deep and bottom (e.g., Östlund et al., 1982; Schlosser et al., 1994). The mean residence time of surface waters has been estimated to range from 2 to 5 years and to show small lateral variability across the Arctic Ocean basins. The mean residence times of halocline waters can vary from 5 to 15 years (Schlosser et al., 1999; Ekwurzel et al., 2001). The mean residence time in the Atlantic layer ranges from years to decades depending on the location. Finally, residence times of the deep and bottom waters have been determined to range from 50 years within the Eurasian Basin to 450 years within the Canadian Basin.

2.3 Data and Method

2.3.1 Sample Collection and Measurement

The findings presented in this section are derived from the same dataset and analytical methods used in the study the Atlantic layer and summarized in Chapter 1. Here we constrain the

analysis to samples located within the halocline layer, found immediately above the FSBW and identified on average salinity ranges.

2.3.2 Water Mass Definition

We based our water mass classifications for the UHW and LHW on salinity surfaces found the literature. We define the salinity ranges for lower and upper halocline waters as $33.9 \leq S \leq 34.5$ (or 34.2 ± 0.3); and $32.8 \leq S \leq 33.5$ (or 33.1 ± 0.4), respectively (Jones & Anderson, 1986; Anderson et al., 1994). The corresponding mean density surfaces for the UHW and LHW are $\overline{\sigma}_0 = 26.5 \pm 0.1$ kg m^{-3} and 27.5 ± 0.1 kg m^{-3} respectively (Figure 7).

A total of 550 ^{3}H/^{3}He ages from 285 stations fall within the LHW salinity range and are used in our analysis. Results for the UHW are derived from 316 ^{3}H/^{3}He age data from 130 stations. Hydrographic properties and ^{3}H/^{3}He apparent ages representing the average values of the samples within these density ranges are shown in the surface maps in Figure 8.

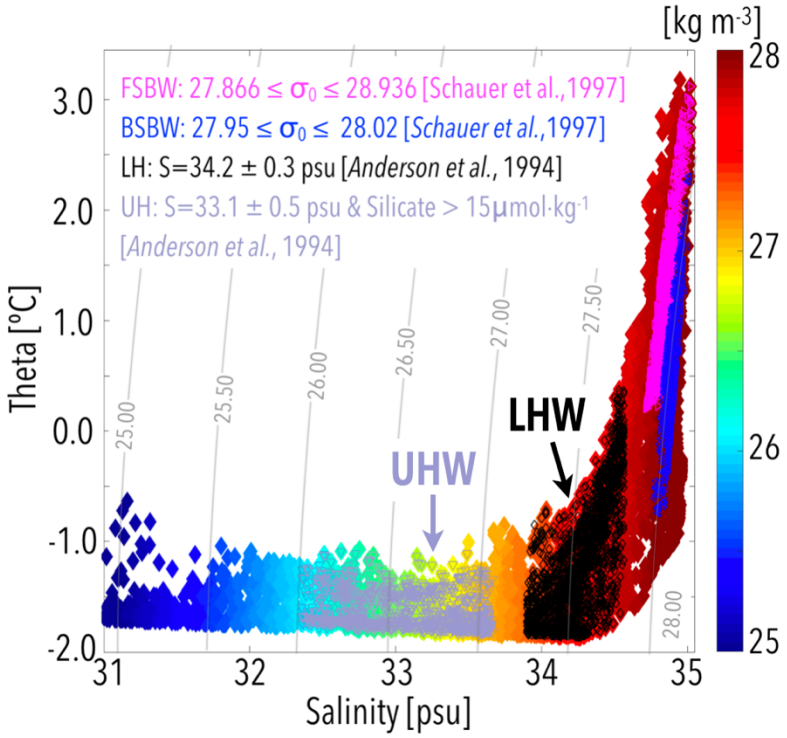

Figure 6. Selected water mass definition from previous studies (Jones and Anderson, 1986; Anderson et al., 1994; Schauer et al., 1997). The diamonds are water samples from our data base collected from 1987 to 2013 and color coded by $\overline{\sigma}_0$.

2.4 Results

We identify the water samples falling within the UHW and LHW definitions and compute the mean pressure, potential temperature and apparent age at the hydrographic station where data are available. Figures 7 and 8 show the distribution of the hydrographic parameters and $^{3}H/^{3}He$ apparent ages averaged over the study period and over the Arctic Ocean basins for the LHW and UHW layers. Despite the large-scale interannual variability affects water mass characteristic to these water masses from the hydrographic properties and tracer distribution. The contrast in the mean halocline properties between the Eurasian and Canadian Basins Halocline are clearly captured. Signals from seasonal to interannual processes such as winter convection and changes correlated to atmospheric forcing are filtered out by the 27-year average.

2.4.1 Lower Halocline Water

The LHW layer is on average shallower and colder in the Eurasian Basin than east of the Lomonosov Ridge. The LHW mean depth and potential temperature in the eastern basins are 90m ± 30m and -1.2ºC ± 0.4 ºC respectively. In the Canadian Basin the LHW mean depth is 160m ± 50m and its average potential temperature is 0.8ºC ± 0.3ºC. These modifications are in agreement with the assumption that FSBW and BSBW make the largest contributions/ventilation sources for this water mass. As it flows around the Arctic Ocean, Atlantic layer gets progressively deeper and loses parts of its heat to the water mass above, the LHW.

The LHW shallowest depths are observed north of Fram Strait and the Santa Anna Trough the LHW mean pressure range from 30m to 70m. In the central Eurasian Basin and near the Laptev and Kara Seas shelves the average depth ranges from 90m to 110m. In the western section of the Amundsen Basin, north of Greenland, the LHW layer is centered at ca. 130m. In the Makarov Basin and in the Switchyard region the mean depth ranges from 120 m to 165 m.

The LHW core is found at the deepest level in the Canada Basin: 200 m to 260 m, with the larger values found in correspondence of the Beaufort Gyre. The spatial variability of the LHW depth is correlated to the presence or absence of the Pacific-derived UHW layer. In Eurasian Basin the halocline layer is thinner as the overlying UHW are not present: here, the temperature and salinity stay almost constant in the surface layer until they both rapidly increase to match the characteristic values of the Atlantic layer (Rudels et al., 2004). On average the LHW potential temperature along the continental shelves ($-1.4^{\circ}C \leq \theta \leq -1.2^{\circ}C$) of the Eurasian Basin is 0.8 ºC colder than in the southern Canada Basin ($-0.9^{\circ}C \leq \theta \leq 0.6^{\circ}C$). The Makarov Basin displays average temperatures that are in between these two limits.

The LHW youngest apparent $^{3}H/^{3}He$ ages (0-9 years) are found in the Nansen Basin, at the continental slope between Fram Strait and shelves of the Laptev Seas. In this region the tracer distribution show is quite homogenous and shows no significant gradient. The oldest apparent ages are located in the Switchyard region (22-25 years). The $^{3}H/^{3}He$ ages in the Canada Basin range from 15 years to 21 years with the oldest values clustered in southern section at the Beaufort Sea. Stations located in the Makarov Basin and over the Lomonosov Ridge have mean $^{3}H/^{3}He$ ages between 9 years and 12 years. The western quadrant of the Eurasian Basin, from Greenland to the North Pole display a large variability, with ages ranging from 9 to 22 years within a 300-500km radius. The presence of such steep gradients can be explained by the

confluence of different circulation branches and will be discussed in the following sections.

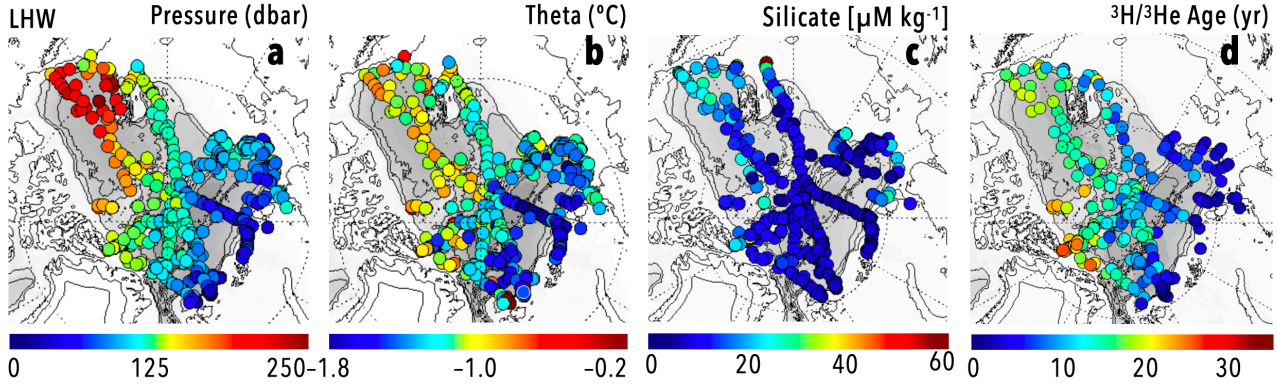

Figure 7. Maps showing the averaged properties of the Lower Halocline Water (LHW). Hydrographic station locations are displayed as filled circles colored according to the average water pressure, potential temperature, and 3H/3He apparent ages.

2.4.2 Upper Halocline Water

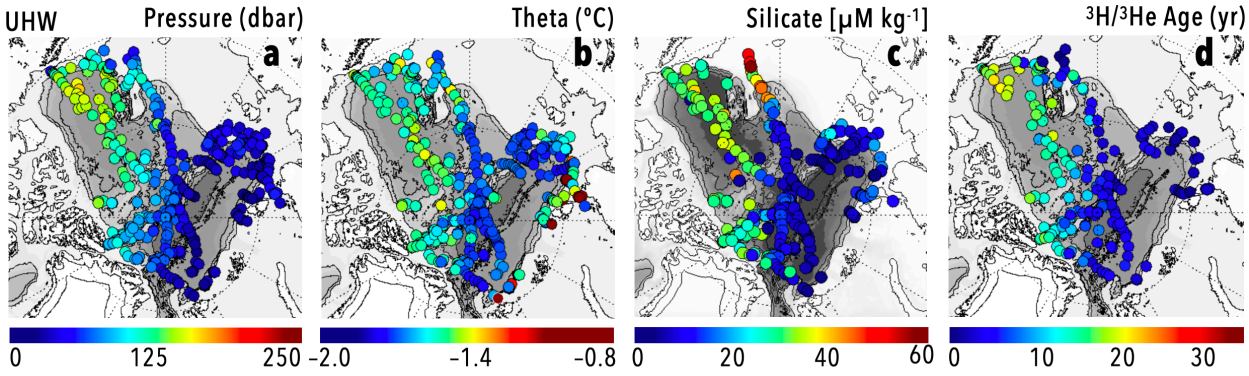

Figure 8. Maps showing the averaged properties of the Upper Halocline Water (LHW). Hydrographic station locations are displayed as filled circles colored according to the average water pressure, potential temperature, and $^{3}H/^{3}He$ apparent ages.

2.5 Discussion

The basin-wide structure of the halocline water circulation is still largely unclear. Halocline waters have several ventilation sources and are more exposed to vertical mixing and detrainment from the continental shelves than the Atlantic layer (Aagaard et al., 1981; Smethie et

al., 2000). Jones (2001) hypothesizes that the general halocline layer pathways resemble those of its ventilation sources: with the LHW flowing in cyclonic, topographically-driven boundary currents in similar fashion to Atlantic waters; and the Pacific-derived UHW spreading northward into the Canada Basin and following either the Beaufort Gyre or the Transpolar Drift stream before exiting the Arctic Ocean via the Canadian Archipelago and Fram Strait (Steele et al., 2004; Falck et al., 2005; Dodd et al., 2012). Tracer data are used to delineate the LHW and UHW circulation patterns independently from hydrographic data and direct measurements and to add temporal information to the circulation of the halocline waters in the Arctic Ocean.

2.5.1 Lower Halocline Water

Tracer distribution along the LHW surface shows age gradients that are agreement with the schematics of Atlantic waters circulation in the Arctic Ocean firstly outlined by Rudels et al. (1994) (Figure 9). Firstly, $^{3}H/^{3}He$ apparent ages monotonically increase from the western Nansen Basin to the Switchyard region along the continental slope confirming that the LHW flows as cyclonic boundary current. Secondly, age gradients closely match the underlying bathymetry at the Gakkel, Lomonosov, and Alpha-Mendeleev Ridge supporting the presence of returning circulation branches in the Eurasians and Canadian Basins.

The mean apparent tracer ages for LHW at stations located between Fram Strait and Santa Anna Through is 2.2 years, ranges from 0.5 and 4.8 years, and displays no significant aging between the two locations. This large range in apparent age at Fram Strait reflects the complex flow structure and transport across and north of Fram Strait where different types of modified Atlantic waters that have either completed the whole circumpolar boundary current or have recirculated southward following shorter pathways interact and mix (Mauritzen et al., 2011; Beszczynska-Möller et al., 2012). Marnela et al. (2013) estimate that half of the northward flowing AW recirculates within Fram Strait and flows southward as a component of the East

Greenland Current. In a similar fashion to what observed for FSBW, ages undergo a partial 'reset' to younger ages north of the Santa Anna Trough where the two Atlantic branch water pathways converge. Moving east along of the continental slope (1000 isobath) from the Laptev Sea to intersection with the Lomonosov Ridge the mean $^{3}H/^{3}He$ ages is 3.9 years and ranges from 2.5 to 6.4 years. At stations located west of the Chukchi Plateau the mean apparent age is 11.7 ± 1.9 years; it increases to 15.4 ± 4.3 years at stations sitting east of the highlands. Along the Alaskan slope the average apparent age is 17.8 ± 3.2 years and varies between 10.9 years and 20.8 years. The LWH oldest ages are observed near the southern extension of the Alpha Ridge and in the Switchyard region with an average of 24.4 ± 1.9 years.

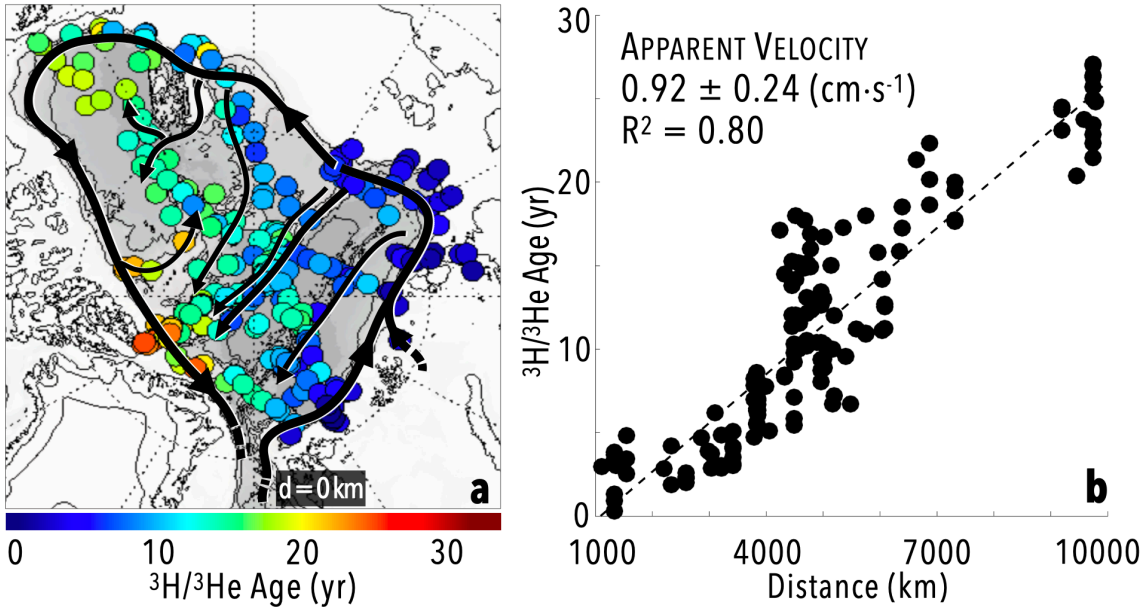

Figure 9. Schematic of intermediate waters circulation in the Arctic Ocean after Rudels et al. (1994) displayed on top of the mean apparent $^{3}H/^{3}He$ ages for the LHW (panel a). Mean LHW apparent $^{3}H/^{3}He$ ages plotted as a function of distance from Fram Strait. The apparent spreading rate is obtained from a non-weighted linear regression (panel b).

Although the LHW is primarily formed by modified Atlantic branch waters in the Eurasian Basin (Rudels et al., 2004), it is also partially exposed to interactions with the overlying layer (e.g., brine injection, winter mixing) and to detrainment from the continental shelves

(Aagaard et al., 1981;). This contributes to expand the age spread observed at each location. Mclaughlin et al. (2004) suggest that water originated from the East Siberian Sea also feed the LHW in the Canadian Basin, between the Mendeleyev Abyssal Plain and northern Chukchi Plateau.

The highest age values in the Eurasian Basin are found in the central region, over the Gakkel Ridge at 60 ºE (14.5–17 years) and in its western quadrant between Morris Jesup Ridge and Yermak Plateau (13.5–15.8 years). In the Canadian Basin, the youngest ages are constrained to the Makarov Basin section between the Mendeleev Ridge and the Lomonosov Ridge (7–10 years); the oldest ages are found in southern Canada Basin (18.8–20.8 years). The latter age range is significantly higher than the residence time previously estimated for the lower halocline layer (Schlosser et al., 1999; Ekwurzel et al., 2001). An additional new finding is that the LHW residence time is not uniform across the Arctic Ocean but there is a gradient of ca. 10 years between the LHW mean age in the Eurasian Basin and in the Canadian Basin. Ekwurzel et al. (2001) estimate the lower halocline mean residence across the Arctic Ocean to be 9.6 ± 4.6 years, in agreement with our result of 11.7 ± 5.3 years.

2.5.1.1 Apparent Spreading Rates

Following the same approach used in Chapter 1, we identify six pathways by following the age gradients along the salinity surface of 34.2 ± 0.3 along the continental margin and other major topographic features of the Arctic Ocean basins. All the circulation branches are strongly guided by seabed features and in agreement with previously established circulation schemes for the Atlantic layer.

Applying this method, the boundary current loop along the shelf slope around the entire Arctic Ocean is clearly visible (Figure 10). The Arctic Ocean boundary current is further split

into the Eurasian Basin (EBBC) and the Canadian Basin (CBBC) (Figure 6). Two additional flow paths are located in the Eurasian Basin and are directed towards Greenland: the Eurasian Basin Return Branch (EBRB), roughly parallel to Nansen Basin flank of the Gakkel Ridge; and the Lomonosov Ridge-Amundsen Basin Branch (LRAB), flowing along the eastern flank of the Lomonosov Ridge (eastern side). The next two branches are located in the Canadian Basin: the Lomonosov Ridge Return Branch (LRRB), flowing on top of the Lomonosov Ridge; and the Mendeleyev Ridge Returning Branch (MRRB), aligned with the Mendeleyev Ridge. Both the LRRB and the MRRB are northward bifurcation of the boundary current and are directed towards Fram Strait. The original circulation scheme of Rudels et al. (1994) outlines a cyclonic gyre in the Makarov Basin, with AW flowing towards Greenland along the Alpha-Mendeleev Ridge and back to Siberia along the western flank of the Lomonosov Ridge. This study only includes the first half of this circulation cell (MRRB), as there are not enough data to fully analyze second half due to convergence of different flow paths.

The $^{3}H/^{3}He$ age distribution in the Canada Basin interior indicate that fractions/portions of the boundary current are diverted northward into the Canada Basin interior along two further pathways, off the Chukchi Plateau/Northwind Ridge and one following the Alpha Ridge into the central basin. The actual trajectories taken by Atlantic branches west of the Lomonosov Ridge, for instance over complex topography north of the Chukchi Sea, are still largely presumed (Woodgate et al., 2007).

The apparent velocities calculated from $^{3}H/^{3}He$ ages along the LHW pathways (Table 5) differ from the actual advective velocities because the tracer-derived values are skewed by the effect of mixing (Wallace et al., 1992; Schlosser et al.,1995). The primary source if this offset is the entrainment of older waters from the basin interiors systematically increases the $^{3}H/^{3}He$ ages

in the boundary current and major circulation branches, which makes the apparent velocities on average slower than the actual speeds.

An important result from this contribution is that the LHW flow paths closely resemble that of the Atlantic Layer in agreement with what hypothesized by Jones (2001) and the circulation schematics outlined by Rudels et al. (2004). In our analysis, we apply a model-derived correction factor of 2.78 ± 0.83 to the LWH apparent velocities along the boundary current and across different circulation branches. This correction factor is based on the findings of Mauldin et al. (2010) and was derived for the lower branch water Barents Sea Branch Water circulation at the continental slope and the western side of the Lomonosov ridge. The error (ε_i^{corr}) for each corrected velocity (v_i^{corr}) is calculated as the square root of the sum of the fractional error of the apparent velocity ($\varepsilon_i^{app}/v_i^{app}$) and the correction factor fractional error. I.e., $\varepsilon_i^{corr} = v_i^{corr} \cdot \sqrt{\left(\varepsilon_i^{app}/v_i^{app}\right)^2 + (0.83/2.78)^2}$.

Applying a correction factor originally inferred for a deeper, more isolated water mass circulation along the boundary current is a first-order approximation but provides a way to compare tracer-derived current velocities with the few available direct current measurements and modeled rates. The corrected velocity values for LHW are summarized in Table 5. After correcting for mixing, the overall LHW mean velocity is 2.56 ± 0.83 cm s^{-1} (R^2 = 0.80). The corrected velocity along the boundary current, from Fram Strait to Switchyard is 2.76 ± 0.84 cm s^{-1} (R^2 = 0.94). The fastest loop is the Eurasian Basin boundary current (EBBC), where the mean velocity is and 3.40 ± 2.07 cm s^{-1} (R^2 = 0.33); the poor correlation of this fit is likely due to the strong mixing at Fram Strait and the Santa Anna Trough. West of the Lomonosov Ridge (CBBC) the velocity decreases to 2.61 ± 0.87 cm s^{-1} (R^2 = 0.85). The returning branch following the western flank of the Gakkel Ridge (EBRB) has a corrected velocity of 1.38 ± 0.73 cm s^{-1} (R^2 =

0.61); a slightly faster rate than that calculated along the Amundsen Basin side of the Lomonosov Ridge Returning Branch (LRRB), 1.26 ± 0.71 cm s^{-1} (R^2 = 0.61). The slowest velocity is along the branch that turns northward at the Mendeleev Ridge and is 0.68 ± 0.45 cm s^{-1} (R^2 = 0.56) after the correction.

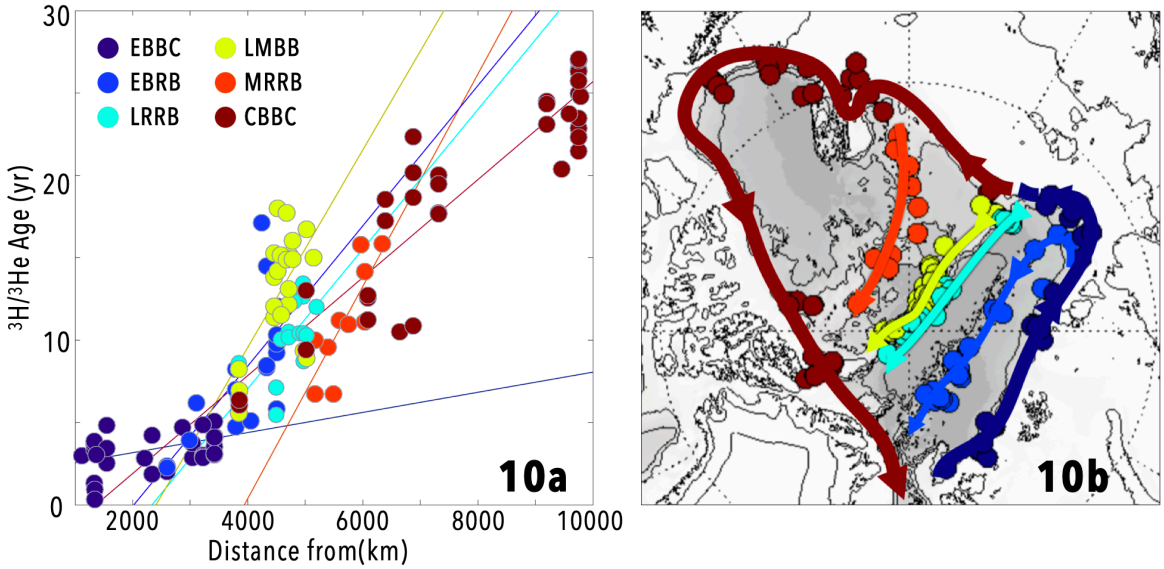

Table 5. *Apparent and corrected velocity estimates for Lower Halocline Water along different circulation branches.*

Branch	Apparent Velocity (cm s^{-1})	Corrected Velocity (cm s^{-1})	R-square	stn
Arctic Ocean	0.92 ± 0.24	2.56 ± 0.83	0.80	152
Arctic Ocean Boundary Current	0.99 ± 0.20	2.76 ± 0.84	0.94	65
Eurasian Basin Boundary Current (EBBC)	1.22 ± 0.81	3.40 ± 2.07	0.33	31
Canadian Basin Boundary Current (CBBC)	0.94 ± 0.27	2.62 ± 0.87	0.85	34
Eurasian Basin Return Branch (EBRB)	0.50 ± 0.28	1.38 ± 0.73	0.61	14
Lomonosov Ridge Return Branch (LRRB)	0.45 ± 0.28	1.26 ± 0.71	0.61	13
Lomonosov R. Makarov B. Branch (LMBB)	0.27 ± 0.12	0.75 ± 0.32	0.70	26
Mendeleev Ridge Return Branch (MRRB)	0.24 ±0.18	0.68 ± 0.45	0.56	10

Figure 10. Locations and mean apparent 3H/3He ages plotted as a function of distance for the hydrographic stations used to calculate the spreading rates for the LHW circulation branches shown in Table 2. Data points in Figure 6a are color coded by the corresponding circulation branch displayed in Figure 6b. The factor of 2.78 ± 0.83 cm s-1 is applied to obtain corrected velocities is following Mauldin et al. (2010).

2.5.1.2 Comparison with the Atlantic Layer

Although the general circulation patterns of the Lower Halocline layer closely resemble those defined for the Atlantic Layer the mean apparent ages and velocities differ across the two water masses. The age offset between the LHW and the FSBW increases moving away from Fram Strait along the boundary current. In the Eurasian Basin, where the Atlantic layer core is located at 250 ± 50 m and that of the LHW at 80 ± 20 m, there is no significant age difference between the two layers. Along the Alaskan continental slope, the LHW core is on average 5 years younger and 200 m shallower than the Atlantic layer core. The age offset reaches its maximum the Switchyard region (ca. 8 years). The mean velocity calculated for the LHW over the entire Arctic Ocean is 0.14 cm s^{-1} faster than that obtained for the Atlantic layer. Along the Arctic Ocean boundary current the LHW is on average 0.11 cm s^{-1} faster than the FSBW. East of the Lomonosov Ridge along the EBBC, the difference in flow speed between the two layers is one order of magnitude smaller than the error (FSWB is 0.05 cm s^{-1} faster than the overlying LHW); for stations west of the Lomonosov Ridge along the CBBC branch the velocity difference increases to 0.23 cm s^{-1}. The variance in tracer-derived velocities across water masses is not significant but it can partly explain why the age difference across the two water masses increases moving cyclonically along the

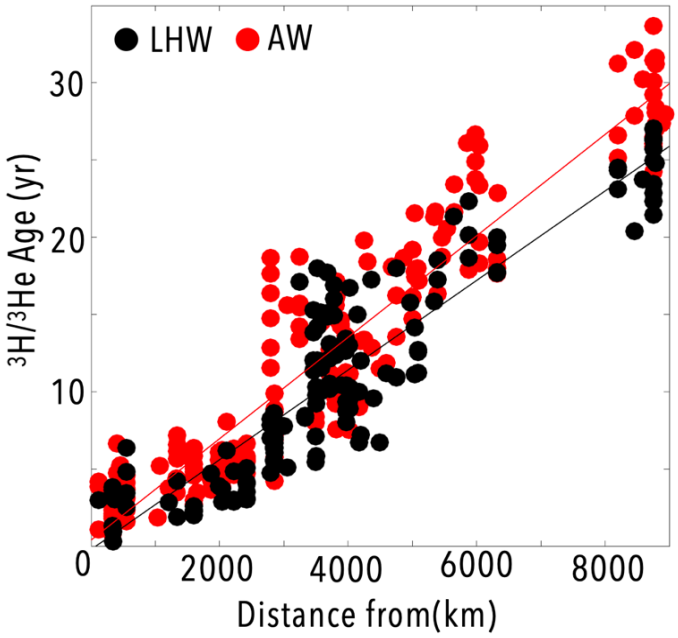

Figure 11. Mean Fram Strait Branch Water (AW) and lower halocline water (LHW) apparent 3H/3He ages plotted as a function of distance from Fram Strait and displayed as red and black dots respectively.

boundary current route. In a similar fashion to what observed for the Atlantic layer, the LHW fastest rates are along the boundary current; and the slowest loops are the LMRR and the MRRB. The EBBC is faster and has a lower correlation fit than the CBBC along the LHW and the Atlantic layer. The EBRB is slower than the LRRB along the lower halocline surface, but the opposite is true in the Atlantic Layer.

2.5.2 Upper Halocline Water

After cross Bering Strait Pacific-origin waters flow into the Canadian Basin along three major branches (Steele et al., 2004; Timmermans et al., 2014). The first flows through Barrow Canyon and continues as eastward boundary current along the Alaskan continental slope. Along the second branch Pacific waters are channeled into Herald Canyon and spread northward along the continental slope of the East Siberian Sea into the Transpolar Drift stream. The third branch flows over the central Chukchi and becomes entrained into the Beaufort Gyre. The volume transport, velocity, and location of each pathway are temporally variable and depend on atmospheric forcing. Changes in the intensity and geographical alignment of the Beaufort Gyre and TPD have significant consequences on the lateral distribution and the residence times for Arctic surface, halocline, and Atlantic waters (Maslowski et al., 2000; Karcher et al., 2006; Newton et al., 2008). Periods of anticyclonic or cyclonic regimes over the Canada Basin are correlated with the Arctic Ocean Oscillation index (Proshutinsky & Johnson, 1997; Steele et al. 2004; Proshutinsky et al., 2015).

This study uses the Pacific water circulation schemes outlined by Steele et al. (2004). In their analysis the authors identify three components of the Pacific-derived halocline water: the Alaskan Coastal Water (ACW), summer Bering Sea Water (sBSW), and winter Bering Sea Water (wBSW); and explain that the relative proportions of these waters at any locations and circulation branch vary in time and space and is linked to climate forcing. They suggest that

during low AO index years, the geographical separation of these water masses is reduced. In our tracer-based analysis of flow paths and residence times we don't distinguish between the three types of Pacific Water but only to the Pacific-influenced halocline water. We constrain our UHW analysis to the region corresponding to lateral extent of Pacific waters into the Canadian Basin as defined by the mean silicate distribution (Figure 8). Closely, only $^{3}H/^{3}He$ apparent ages of water samples with silicate concentrations above 25 μM kg^{-1} are included.

Four main findings on the UHW general circulation patterns and residence times can be derived from the mean apparent age structure shown in Figure 8.

(1) Along Alaskan slope, near Barrow Canyon, the $^{3}H/^{3}He$ apparent ages display a large range and vary from 3 years to 16.2 years within a distance of ca. 30–40 km. This spread signals the confluence of relatively young waters flowing directly from Bering Strait along Barrow Canyon (eastward boundary current) with waters that have become entrained into the Beaufort Gyre. (2) Tracer ages progressively increase along the anti-cyclonic circulation branch of the Beaufort Gyre: from 0.5–3.1 years over the Chukchi Sea, to 14.4–15 years at the northern limb the gyre, to 17–22.7 years along the southern limb near the continental slope (approximately between 140ºW to 150ºW). This result indicates that the UHW circulation pattern differs from that established for the underlying layers, is driven by surface stresses, and is predominantly anti-cyclonic. The relatively high $^{3}H/^{3}He$ apparent ages observed in southern Beaufort Sea suggest that the presence of waters that have become entrained into the reduced Beaufort Gyre and completed at least one full rotation around the gyre. (3) The UHW mean residence times of 20–23 years observed in Beaufort Sea are significantly longer than those previously estimated for this water mass and indicates a slow ventilation rate for a relatively shallow layer. Transient tracer-derived estimates for halocline layer (UHW and LWH) residence times range from 5 to 15

years (Schlosser et al., 1999; Ekwurzel et al., 2001; Karcher et al., 2010). Ekwurzel et al. (2001) assess the mean residence times of the upper halocline waters to be 4.3 ± 1.7 years, a significantly lower value that what we estimate. When comparing the UHW residence times it is important to note that authors include water samples from both the Eurasian Basin and Canadian Basin in their upper halocline water calculations, and that the majority of water sample used are from stations in the western Eurasian Basin. We found the UHW mean residence time to be 3.4 ± 2 years in the Eurasian Basin; and 14.7 ± 5.7 years in the Canada Basin.

(4) The Transpolar Drift flow branch draws Pacific waters directly from the Chukchi Sea to north of Ellesmere Island (Switchyard region). The $^{3}H/^{3}He$ age gradients increase along the Transpolar Drift flow, from 4 ± 1.7 off the Chukchi shelf, to years to 12 ± 1.3 years roughly in the central Alpha-Mendeleev Ridge, to 15 ± 1.3 years north of Ellesmere Island. The aging along the second half of this flow path is quite small and could indicate an accelerating spreading rate.

The Transpolar Drift stream redirects sea ice, river runoff, and other surface waters to the Fram Strait and further south into the East Greenland Current.

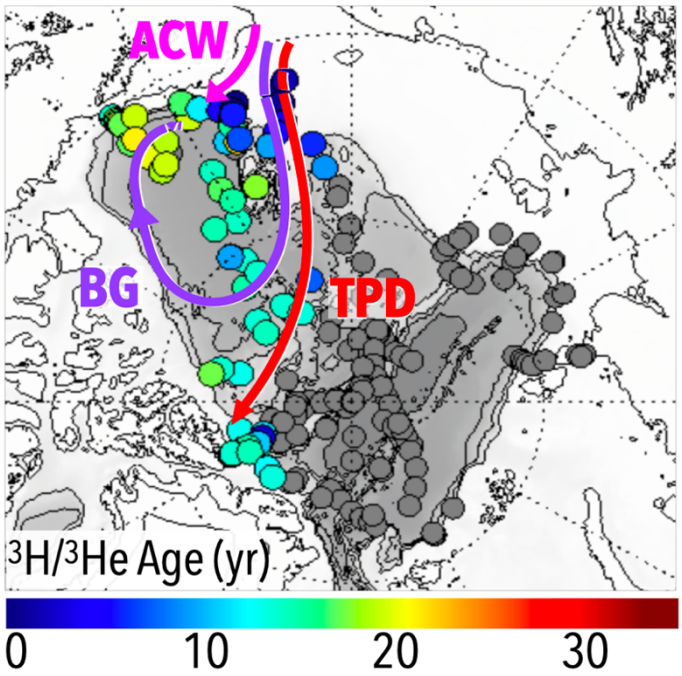

Although its intensity changes with climate forcing, the transport times along the Transpolar Drift are swift. Travel times for Pacific waters to reach the Switchyard region from the Chukchi Sea are estimated to be 3–5 years (Steele et al., 2004). Given the complex recirculation in the Switchyard region, these data points are not included in the spreading rate calculation (Figure 13). Despite the large variability affecting the UHW, the picture emerging from our 3-decade-average tracer distribution is one providing clear and new information on the general circulation patterns, spreading velocities, and residence times of the Pacific-derived UHW in the Canada Basin.

Figure 12. Schematic circulation of Pacific UHW based on Steele et al. (2004) displayed on top of the mean apparent 3H/3He ages. The three flow pathways are labeled as: ACW, Alaskan Coastal Water. BG, Beaufort Gyre. TPD, Transpolar Drift stream.

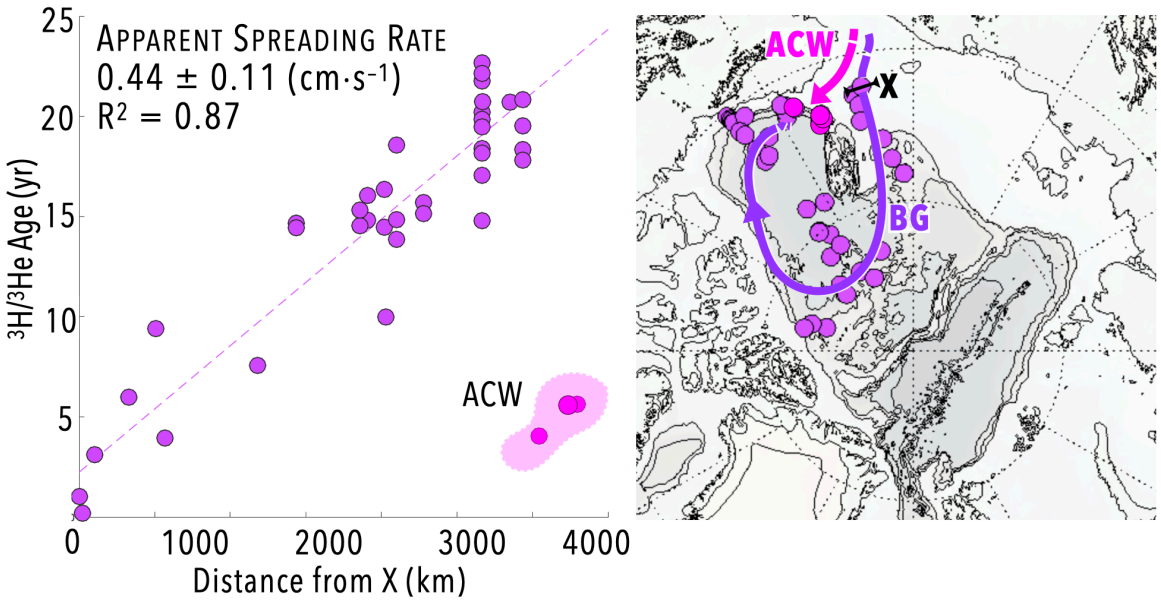

Figure 13. Locations and mean apparent $^3H/^3He$ ages plotted as a function of the distance from the Chucky Sea (point X in Figure 13b) for the hydrographic stations used to estimate the spreading rate along the Beaufort Gyre. The apparent spreading rate is obtained from a non-weighted linear regression. Note: the datapoints highlighted in magenta are not included in the fit calculation as they are considered to belong to the Alaskan Boundary Current (ABC) branch.

2.6 Conclusions

Tracer data show that LHW flow as a cyclonic boundary current along the continental shelf and the major ocean ridges, is topographically steered, and closely resembles that of the underlying Atlantic layer. The mean $^3H/^3He$ apparent age measured in the LHW is 6.9 ± 4.3 years in the Eurasian Basin and 16.4 ± 6.4 years in the Canadian Basin. The average apparent spreading velocity for the LHW calculated from the $^3H/^3He$ data is 0.92 cm s^{-1} (R^2 = 0.80) and ranges from 0.24 to 1.22 cm s^{-1}, depending on the individual circulation branch. The velocity decreases with depth along the Arctic Ocean boundary current. Differences in the flow regimes primarily explained this gradient. Additionally, shallower layers are progressively more exposed to mixing with the younger surface waters. The boundary current apparent velocities are 0.99 ±

0.20 cm s^{-1}, 0.88± 0.19 cm s^{-1}, and 0.79 ± 0.13 cm s^{-1} for the UHW, FSBW, and BSBW respectively.

Tracer data suggest that the circulation of Pacific UHW is decoupled from the cyclonic flow of the lower halocline and Atlantic layers and is primarily driven by surface stress forcing with a well-established anti-cyclonic flow around the Beaufort Gyre. The UHW mean $^{3}H/^{3}He$ apparent ages of ca. 20 years in the Beaufort Sea is significantly higher than what observed in any other region of the Arctic Ocean and previously estimated.

Chapter 3: Freshwater components in the Canadian Basin: Distribution, sources, and variability

3.1 Introduction

The oceanic freshwater cycle plays a fundamental role in the climate and biological systems. Although the Arctic Ocean covers only 3 % of the surface of the world's oceans, it contains about 10 per cent of its freshwater and receives 11 % of global river runoff (Dai & Trenberth, 2002). Thus, the freshwater balance of the Arctic Ocean and its exchange with lower latitudes are important elements of the global climate system and the biology of the world ocean.

The Arctic, including its ocean, are presently undergoing rapid environmental change. One of the most pronounced features of this change is the retreat of the Arctic sea ice cover with consequences for the circulation of the near surface waters and the freshwater balance.

Changes in the hydrography compared to the climatology derived from the Environmental Working Group data set have already been observed during recent decades (e.g., Morison et al., 2012). The most dramatic hydrographic changes are found in the upper parts of the water column: the mixed layer, the halocline, and the Atlantic layer. Vertical density gradients between surface and halocline waters control the flux of heat from the Atlantic layer to the surface and are a key factor in sea-ice extent and thickness (e.g., Serreze et al., 2006). In the polar oceans, these gradients are largely controlled by the distribution of salinity, and we need to understand the dynamics controlling changes in the atmosphere and oceanic circulation and their impact on the freshwater distribution in order to project the local, regional and global consequences of ongoing changes.

Stratification in the Arctic Ocean upper water column is subject to strong variability due to internal and external forcing factors. For instance, the freshwater content undergoes significant

variations in both inventories and fluxes due to temporal and spatial variability in the distribution and spreading pathways of sea ice and liquid freshwater, as well as properties and volumes of the inflows from the Atlantic and Pacific waters (Polyakov et al., 2008). There are several external sources of freshwater and low salinity waters into the Arctic Ocean. River runoff accounts for roughly 40%, Pacific inflow for 30%, and net precipitation (P-E) for 30% (Haine et al., 2015; Carmack et al., 2016). Export of freshwater and sea ice, via the Canadian Archipelago and Fram Strait, plays an important role in the global thermohaline circulation. While roughly 85% of the Arctic Ocean total freshwater is in liquid form, only 73% leaves the polar basin as liquid. Most of the Arctic Ocean sea ice export occurs through Fram Strait (Jahn et al., 2012; Carmack et al., 2016).

GEOTRACES is an international research program designed to further our understanding of biogeochemical cycles by compiling a dataset of the distributions of key trace elements and isotopes in the global ocean. The 2015 U.S. GEOTRACES Arctic Transect (GN01) was part of a multi-national effort to sample trace elements and isotopes in the Arctic Ocean. The U.S. expedition covered the western Arctic Ocean in the boreal summer of 2015. The other coordinated international expeditions involved the deployment of ice-capable research ships from 5 nations (US, Canada, Germany, Sweden, UK) across different parts of the Arctic Ocean. The GN01 cruise proceeded as two sections, to and from the North Pole area, encompassing the Bering Sea, Bering Strait, Chukchi Borderlands, and the deep central Amerasian Basin. The two sections, northbound roughly along the International Date Line(180 ºW) and southbound roughly at 150 ºW, provide approximate repetitions of the previous Arctic Ocean Sections in 1994 and 2005 (AOS94 and AOS2005) respectively.

This contribution presents the stable isotope data collected during GN01 discusses the distribution and storage of liquid freshwater content of the upper water column and the decomposition of samples into fractions derived from Atlantic inflow, Pacific inflow, sea-ice meltwater, and meteoric waters (runoff and precipitation). The 2015 results are then compared to AOS94 and AOS2005 to estimate temporal and spatial changes in the freshwater distribution and composition in the Canadian Basin of the Arctic Ocean. The comparisons reveal information on how representative the GEOTRACES results are to examine the origin of the freshwater components and their role for trace element dynamics in the Arctic Ocean. They also provide information concerning the basic dynamics of the Arctic Ocean freshwater budget and its dynamics that underlies its variability and change.

3.2 Hydrography

Despite being geographically enclosed by the North American and Eurasian continents, the Arctic Ocean is connected and exchanges waters with the two largest oceans. The North Atlantic is the major source of Arctic intermediate depth waters (Rudels et al., 1994). Atlantic waters (AW) enter the eastern Arctic Ocean as two separate branches from the Greenland Sea via the Fram Strait and the Barents Sea through the Santa Anna Trough (e.g., Rudels et al., 1994; 1996; 2012). The former is the relatively warm and saline Fram Strait Branch Water, and the latter is the Barents Sea Branch Water. Atlantic Waters flow cyclonically along the continental slope and major submarine ridges of the Arctic Ocean as a persistent, topographically steered boundary current before flowing back south across Fram Strait (Timofeyev, 1957; Coachman and Barnes, 1963; Rudels et al., 1999; Woodgate et al., 2001). In this chapter, we constrain the definition of AW to the Fram Strait Branch Water, since the Barents Sea Branch Water is found at depths deeper than 500 m, which is outside the scope of our analysis. Pacific inflow into the Canadian

Basin occurs through Bering Strait and is driven by a persistent steric height gradient (ca. 0.7 m) assuming a level of no motion of 800 m (Aagaard et al., 2006). Pacific waters (PW) entering the Arctic Ocean are significantly fresher (PW: S ~ 32.5; AW: S ~ 34.92) than the Atlantic originated waters and are the major source of nutrients into the Arctic Ocean thus playing an important effect on its stratification and biological activity (e.g., Codispoti et al., 2013). The oceanic heat influx carried by the PW is ca.10 times than the Atlantic input but is much closer to the surface layer and the sea ice.

As is by now traditional, we calculate the 'freshwater content' of samples in the Arctic relative to a reference salinity. Some studies use a reference of 34.8, an estimate of the mean salinity of the Arctic (Aagaard & Carmack, 1989). We use 34.92, an estimate of the average salinity of Atlantic inflow, as a reference since a central concern in the upper water column is the climatic impact of freshwater exchange with the North Atlantic (Bauch et al., 1995; Newton et al. 2013). The Arctic Ocean receives and exports large volumes of freshwater both in liquid and solid phase (Carmack et al., 2016). On average 9400 ± 5% km^3 yr^{-1} of freshwater enter the Arctic Ocean annually and 8250 ± 7% km^3 yr^{-1} leaves via Fram Strait (as sea ice and liquid freshwater) and Davis Strait. River discharge is also an important source of dissolved and particulate matters, which impact ocean chemistry and biology (e.g., Bhatia et al., 2013). In order of importance, the largest freshwater inputs into the Arctic Ocean are river discharge, dominated by the large sub-arctic rivers on the Eurasian continent, the Pacific estuarine component from the Bering Strait inflow, and net precipitation over the basins (Aagaard & Carmack, 1989). The seasonal cycle of ice formation and melting also alters the saline and freshwater contents.

With a salinity of S = 0, meteoric waters (river runoff and net precipitation) account for the largest freshwater input to the Arctic Ocean, delivering 6400 ± 14% km^3 yr^{-1} combined

(Haine et al., 2015: based on data collected in 2000–2010). Of this, roughly one third (2200 ± 10% km^3 yr^{-1}) is from net precipitation over the ocean. Pacific inflow is second largest input of freshwater into the Arctic Ocean accounting for 2640 ± 4% km^3 yr^{-1} or 28% of the total input (Woodgate et al., 2006; Haine et al., 2015).

On average, a horizontal sea-level pressure (SLP) difference is observed between the western and eastern Arctic Ocean, with a region of high pressure centered over the Canadian Basin and low pressures over the Eurasian Basin. The resulting wind-driven average sea ice and surface layer flows are characterized by an anticyclonic circulation cell centered in the Canada Basin in correspondence of the pressure high (Beaufort Gyre), predominantly cyclonic currents in the Siberian Arctic, and a current directed from the Eastern Siberian Sea towards Greenland (the Trans-Polar Drift) (e.g., Steele et al., 2004).

Due to the extreme cold of the Arctic climate (which limits the impact of temperature) and large freshwater inputs, the density stratification in the Arctic Ocean water column is primarily defined by salinity, highly stable, and most pronounced in the upper water layers (50–500m). In this study we restrict our attention to the upper 500 m of the Canada and Makarov basins as observed during the 2015 GN01 transects. Using the 2015 dataset, we compute density horizons and average properties for each water mass based on the characteristic hydrographic properties as defined in the water mass classification by Anderson et al. (1994).

The topmost part of the water column is occupied by a wind-steered, well-mixed layer of relatively fresh, near-freezing waters, with densities within 0.1 kg m^{-3} of the density of the topmost CTD measurement (i.e. $\Delta\sigma_0 = 0.1\ kg\ m^{-3}\ where\ \Delta\sigma_0 = \sigma_0(z) - \sigma_0(surface)$) (Toole et al., 2010). This buoyant layer contains a large fraction of the total liquid freshwater and is found virtually everywhere in the surface of the Arctic Ocean. The mean thickness and salinity

of the mixed layer vary considerably on a seasonal timescale and across the Arctic Ocean basins and are influenced by local conditions such as wind forcing, sea ice cover, ice formation, and riverine discharge/river runoff signal. Typically, the surface mixed layer is twice as deep in ice-free regions compared to sea ice covered areas. Its depth is also correlated to the strong seasonality of the discharge of freshwater into the Arctic Ocean from the Russian and Northern American rivers.

Below the mixed layer, salinity increases along steep gradients to reach values above 34.2. This halocline is a fundamental feature of the Arctic Ocean stratification that insulates the cold surface from the warm Atlantic waters flowing underneath (e.g., Aagaard et al., 1981; Rudels et al., 1996). The halocline can span depths three times as thick as the surface mixed layer (Anderson et al., 1994; Rudels et al., 2004). The nature and sources of halocline waters differ between the Eurasian and Amerasian basins. In the Canadian Basin, a layer of upper halocline waters (UHW) is primarily fed by the inflow of Pacific waters from the Bering Strait and is characterized by a maximum in nutrient concentration, approximately aligned with the 33.1-isohaline. Its temperatures lie close to the freezing point, and it is sometimes referred to as the Cold Halocline Layer. In the Eurasian Basin where the Pacific Waters are virtually absent, the Atlantic layer is separated from the surface by Lower Halocline Waters (LHW), which are formed either from above by brine-rejection-driven convection or the horizontal injection of cold, saline shelf waters. The lower halocline layer (LHW) is centered at a salinity of about 34.2 ± 0.3 and is characterized by increasing temperature and salinity (Rudels et al., 1991; Anderson et al., 1994), temperatures above the freezing point, and minimum values in quasi-conservative nutrient-based tracers (Jones and Anderson, 1986; Wilson and Wallace, 1990; Rudels et al., 1991; Anderson et al., 1994). Below the LHW, Atlantic Waters (AW) can be identified by a

potential temperature maximum centered at depths between 250 and 500 m, and salinities well above 34.8. Waters below the Atlantic layer are colder and saltier than the layers above. They are remarkably homogeneous, largely isolated from contact with the surface, and hundreds of years old (Schlosser et al., 1999).

3.3 Sample Collection and Measurement

As part of the Arctic GEOTRACES program two oceanographic sections were completed in the Arctic Ocean between August 9th and October 12th 2015, aboard the U.S.C.G. icebreaker HEALY. The sections extend from the continental slope of the southern Canada Basin across the Canada and Makarov basins to the North Pole (Figure 1). The data from the first six hydrographic stations located in the Bering Sea and Bering Strait are not included in this contribution. The northbound track, comprising Stations 7 to 30, begins on the Chukchi Shelf, at 73.49ºN, 168.85ºW, in approximately 120 m water depth, and ends in the central Makarov Basin, at 88.18ºN,167.73ºW (water depth: ca. 4000 m). This cruise track roughly follows the 180ºW meridian and was designed to replicate/overlap with the 1994 Arctic Ocean Section (AOS94). The southbound track, including stations 32 to 66, starts at the North Pole (Station 32) and runs south along 150ºW to the continental slope. It spans roughly 2500 km and crosses the Lomonosov Ridge and the Alpha Mendeleyev Ridge. This latter section largely overlaps with the trans-Arctic section completed in 2005 aboard the Swedish icebreaker ODEN. In 2015, at Station 56 rough seas prevented the collection of samples in the upper 500m of the water column resulting in a data gap in the southern Canada/Beaufort Sea (Table 6).

At each station depth profiles for salinity, temperature, dissolved oxygen, fluorescence, and nutrients (silicate, phosphate, nitrate, and nitrite) were completed. The data collected during GN01 represent one of the most detailed section of stable isotopes ($\delta^{18}O$ and δD) for the Arctic

Ocean to date (Pasqualini et al., 2016). In this study we used salinity, $\delta^{18}O$, nitrate, and phosphate data collected on three separate oceanographic expeditions in the Canadian Basin between 1994 and 2015 to compute the fractions of meteoric (net precipitation + river runoff), sea ice meltwater, Pacific, and Atlantic water. Geographic locations of the hydrographic stations used by this contribution are shown in Figure 1.

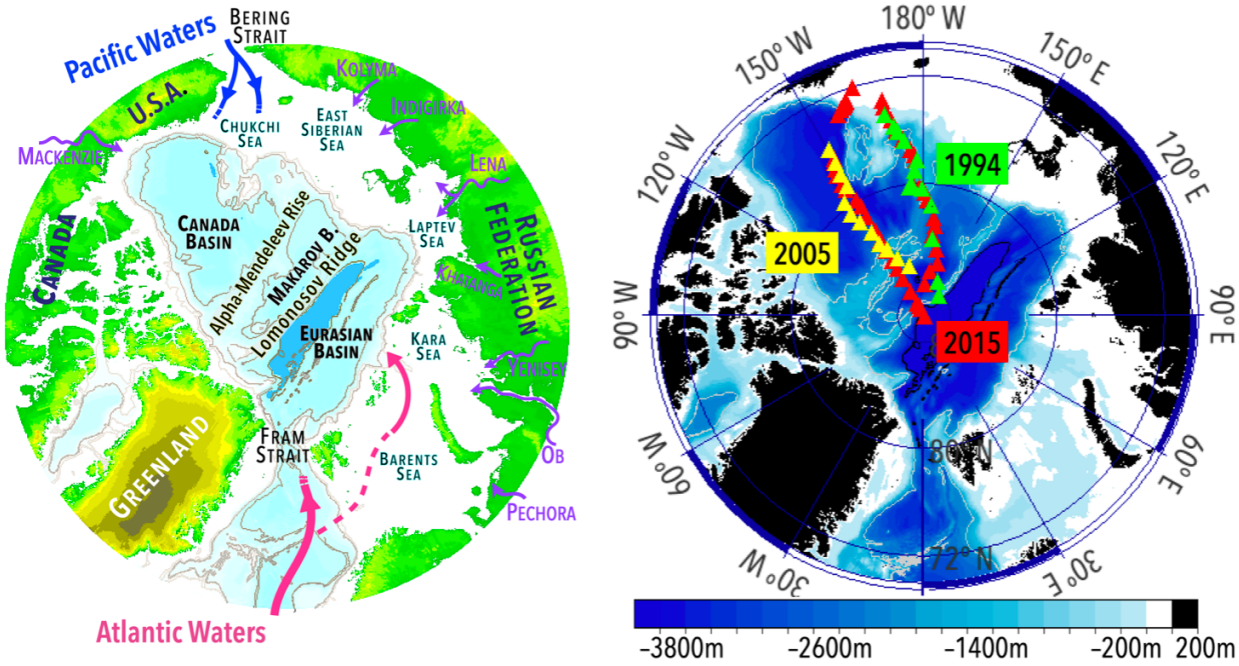

Figure 14. Left panel: Arctic Ocean map showing bathymetric features and geographical locations of the studied areas. Modified from Geology.com. Right panel: Map showing the oceanographic sections part of our analysis. GN01 2015 hydrographic stations are displayed as red triangles, AOS 1994 as green, and the Oden 2005 as yellow triangles.

Table 6. ***Oceanographic sections that have been used in this study.***

Section	Ship	Year	Date Range
Arctic Ocean Section (AOS 94)	*C.C.G.S. Louis S. St-Laurent*	1994	Jun 07–Sep 09
Arctic Ocean Section (ODEN 2005)	*I/B ODEN*	2005	Aug 19–Sep 25
U.S. Arctic GEOTRACES (GN01)	*U.S.C.G. Healy*	2015	Aug 09–Oct 12

Hydrographic data for Oden-2005 and AGT-2015 were produced by the Scripps Institution of Oceanography Data Facility (ODF), Shipboard Technical Support group. Salinity samples collected from the rosette were analyzed onboard using a Guildline 8400 salinometer (accuracy ca. ±0.002). Nutrient concentrations were measured aboard the icebreakers within 1-4 hours of sample collection to allow for all samples to reach room temperature. A Seal Analytical continuous-flow Auto-Analyzer-3 was used for the nutrient analyses following the WOCE (World Ocean Circulation Experiment) standard techniques (Gordon et a1., 1992). Hydrographic data from AOS 1994 were produced onboard following the methods described by Swift et al. (1997).

Stable isotope ratios ($H_2{}^{18}O/H_2{}^{16}O$; $^2H_2O/H_2O$) for the 2015 cruise were measured at Columbia University's Lamont Doherty Earth Observatory using a using a Cavity Ring-Down Spectroscopy (CRDS) technique (Picarro L2130-i Analyzer) with a vaporization module isotopic H_2O A0211 coupled to an HTC-xt Leap Pal Technologies auto-sampler following the methods and procedures described by (Walker et al., 2015). Stable isotope data ($\delta^{18}O$ and δD) are reported as the per mil deviations of the $H_2{}^{18}O/H_2{}^{16}O$ and $^2H_2O/H_2O$ ratios from those of Vienna Standard Mean Ocean Water (VSMOW-2) (Craig, 1961; Gonfiantini, 1981). A stainless-steel liner was placed in the vaporizer to reduce salt residue accumulation. Overall analytical precision for the dataset is ± 0.027 per mil (Pasqualini et al., 2016). The reported isotope ratios were computed as the average of the last three out of six injections. Data processing was performed to correct for memory and drift effects, and a linear regression was applied to normalize samples to the VSMOW2-SLAP2 isotope reference scale. Stable isotope analyses were performed on ca. 1000 water samples covering the entire water column at GEOTRACES stations and the upper 500m at U.S. Repeat Hydrography stations. Oxygen isotope ratios for samples collected during Oden-

2005 were measured at Rutgers University, following the methods described by Fairbanks (1982). Analytical precision for the 2005 data is ±0.025 per mil. Analyses of oxygen isotope ratios for AOS94 were performed at the Lamont Doherty Earth Observatory using mass-spectrometric analysis and were performed after sample equilibration with CO_2 (Roether, 1970; Fairbanks, 1982) with an analytical precision of ± 0.03 per mil.

3.4 Results

During the 2015 cruise, the mixed layer depth spread between 6 m and 30 m with the largest values observed in the Makarov Basin. On average, the mixed layer along the southbound track crossing the central Canadian Basin was 6 meters thicker than along the northbound section (150ºW mean depth = 18.2 m; 180ºW mean depth = 12.1 m). The salinity values measured in the mixed layer ranged between 20.8 and 30.7, with the lowest values observed in the southern Canada Basin, south of ca. 78ºN ($22.9 \leq S \leq 26.3$). North of 78ºN the mixed layer hydrographic properties were remarkably constant with potential temperature (θ) ranging between -1.53ºC and -1.35ºC and salinity between 27.3 and 28.5.

The UHW (defined by the silicate maximum between 60m and 200m and $S = 31 \pm 0.2$) was aligned with the $\sigma_0 = 26.48 \pm 0.2$ isopycnal surface. The depth of this isopycnal ranged from 50 m to 175m. The UHW core was centered at ca. 100 m for stations on the continental shelf, at 175 m in the central Canada Basin, and 75 m in the Makarov Basin. Stations 32 and 35, located over the Lomonosov Ridge, show hydrographic properties characteristic of the Eurasian Basin with a thinner, colder halocline layer, and shallower and warmer Atlantic layer. The core of the LHW ($S = 34.2 \pm 0.3$) was centered at the 27.51 ± 0.03 kg m^{-3} isopycnal corresponding to depths ranging from 125 to 275 meters. The LHW mean depth in the Makarov Basin was ca. 125 m and 250 meter in the Canada Basin.

During GN01, sub-surface potential temperature maxima delineating the presence of waters of Atlantic origin, were observed along the northbound and southbound transects. The maximum temperature ranged from 0.71 ºC to 0.95 ºC in the Canadian and Makarov Basins and 1.3 ºC to 1.6 ºC at the stations located over the western side and top of the Lomonosov Ridge (Stations 32–34). In the 2015 data set, the maximum temperature was centered along the density horizon of σ_0 = 27.93. In 2015 this isopycnal was found at depths ranging from 280m to 500m, with the deeper values found between 76ºN and 80ºN in the southern Canada Basin (180ºW) and the Beaufort Gyre (150ºW). Along the northbound section, the AW displayed relatively constant potential temperatures varying by ca. ± 0.1ºC around a mean value of 0.8ºC. The northernmost stations along the 150ºW track were sampled on top the Lomonosov Ridge or in the Amundsen Basin. Atlantic waters at these stations were significantly warmer than everywhere else in the section. The temperature in the AW increased from 0.7 ± 0.1 ºC (Makarov Basin) to 1.22 ± 0.1ºC (Amundsen Basin) over less than 50 km. This sharp temperature gradient across the Lomonosov Ridge was reflected as well in property changes at the level of the UHW (Figure 2b). With the exception of these stations, the Atlantic core layer temperatures were on average ca. 0.15ºC warmer than those in the basin interior (150 ºW track). The Atlantic layer temperature structure observed during GN01 was in line with the circulation of the Atlantic water which branches at the Siberian end of the Lomonosov Ridge with one branch continuing along the continental shelf slope into the Canadian Basin and the other following the topography of the Lomonosov Ridge towards Greenland (Rudels et al. 1994; Rudels et al., 2000; Woodgate et al., 2001).

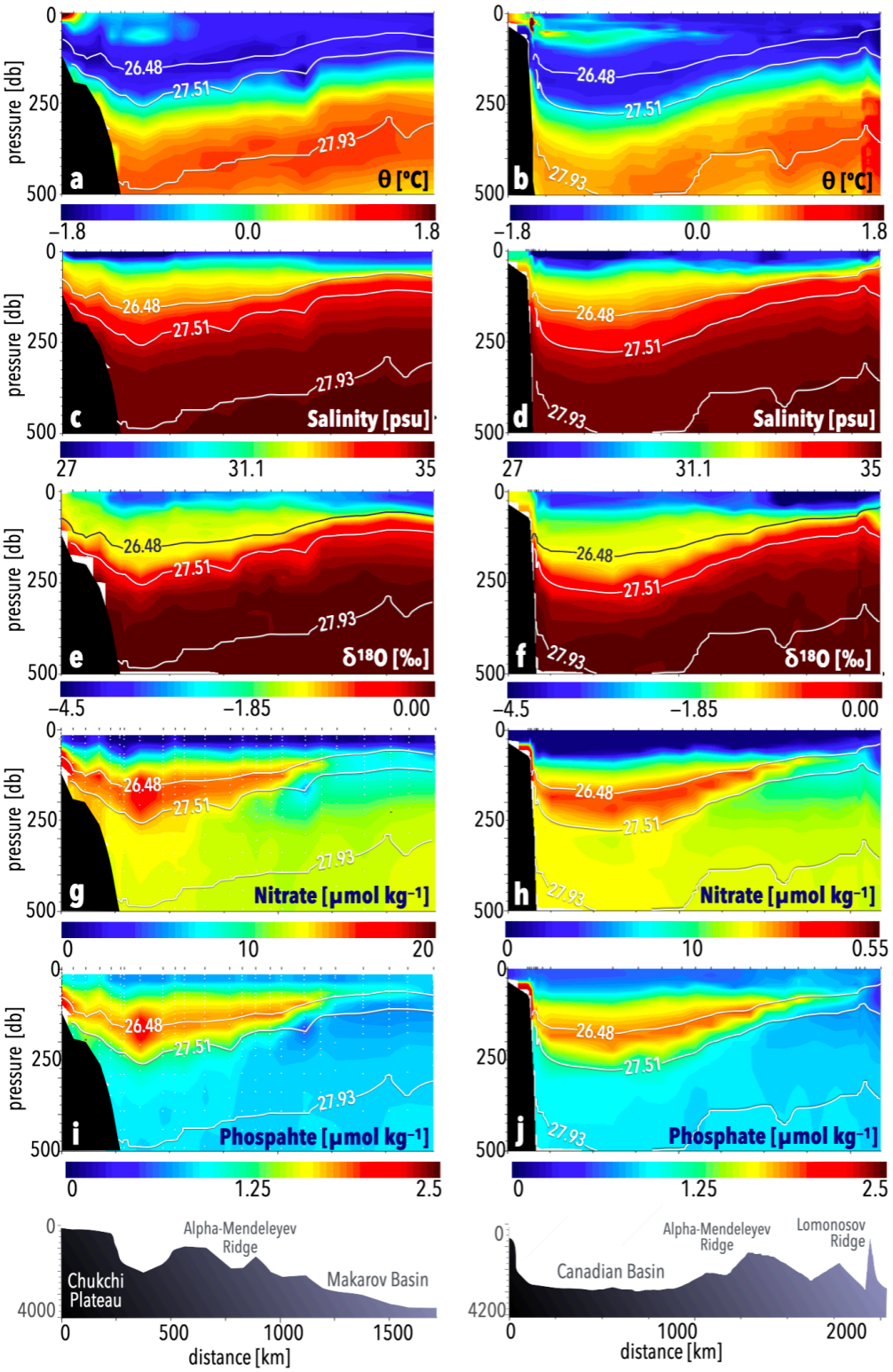

Figure 15. Hydrographic data and combined tracers along the upper 500 m of the GN01 2015 cruise tracks. Left panels: northbound section (180ºW). Right panels: southbound track (150ºW). The UHW, LHW, and AW isopycnals are also displayed.

Near surface temperature maxima caused by summer solar radiation were observed between 15m and 30m depth in the Canada Basin along both sections with more pronounced occurrences along 150ºW. At these locations temperature ranged from ca. -1 ºC to 2 ºC. This temperature profile typically signals the presence of Pacific Summer Water, marked by local temperature maxima between 40 and 100 meters. During GN01 along 150ºW, a warmer plume ($\Delta\theta$: ca. 0.6ºC centered at 60 m depth) was observed extending northwards from the continental shelf into the basin interior for ca. 600–700 km. The coldest water samples (-1.76ºC $\leq \theta \leq$ -1.60ºC) were observed in the UHW at the ice-free, shallow stations on the continental slope (60m – 140m).

Waters with high nitrate and phosphate concentrations (nitrate $\geq$ 15 μmol kg^{-1} and phosphate $\geq$ 1.8 μmol kg^{-1}) extended northward for 1000-1500 km from the southernmost stations as a horizontal plume delimited by the 26.48 and 27.51 isopycnals (Figures 15g–15j). This nutrient distribution identifies the nutrient-rich Pacific waters flowing into the Arctic Ocean from the Chukchi Shelf, is observed along both sections, and is present in historical data as a perennial feature of the Canada Basin. Progressing north, this nutrient enriched layer progressively thins and disappears into the background in the Makarov Basin (ca.1300 km distance from the entry point near station 7).

Surface waters are extremely depleted in nutrients due to biological consumption during summer. Along the 150ºW section, low nutrient concentrations (0 $\leq$ nitrate $\leq$ 2.2 μmol kg^{-1} and 0.25 $\leq$ phosphate $\leq$ 0.8 μmol kg^{-1}) form a homogeneous, continuous surface layer. South of the Lomonosov Ridge (Stations 66 to 35) this surface layer is ca. 30–40 m thick. At Station 32 in the Amundsen Basin, the only station on the Eurasian side of the Lomonosov Ridge, the nitrate-depleted layer extends down to 130m depth. Along this section, the maximum nitrate

concentrations (14–15.7 μmol kg^{-1}) are centered on the isohaline of 33.2 ± 0.2, and sits at depths between 130 and 220 m, with the shallower values observed north of the Alpha-Mendeleyev Ridge (Stations 47 to 44). Below this high-nutrient plume, concentrations are uniform and average 11-12 μmol kg^{-1}. The phosphate distribution closely resembles that of nitrate. The lowest values (0.5 μmol kg^{-1}) are found in the uppermost waters. The surface layer is ca. 40 m deep on the Canadian side and increases to 130 m depth across the Lomonosov Ridge. The maximum concentration follows the 32.95 ± 0.2 isohaline surface and sits between 230 and 130m depth. From this layer downward, the mean background value is 0.8 μmol kg^{-1}. The presence of small amounts of phosphate alongside total nitrate depletion in the surface waters suggests a nitrate-limited system.

Oxygen isotope ratios in surface waters are depleted in the heavier isotope, which reflects a high concentration of meteoric water there. Phase changes, such as freezing and melting, impact the oxygen isotope ratios due to fractionation. For instance, during freezing, seawater molecules bearing the heavier isotope are preferentially incorporated into the sea ice matrix, with a fractionation of ca. 2.09–2.58 per mil (Melling & Moore, 1995; Mcdonald et al., 1999; Song et al., unpublished data). The fractionation factor depends on conditions during freezing, in particular the crystallization rate. Following Ekwurzel et al. (2001) we assume a mean freezing fractionation factor of 2.6 per mil. The horizontal and vertical gradients of oxygen isotope ratios are similar to those of observed in the salinity field. Along GN01, the lowest values (-5.1 ‰ ≤ $\delta^{18}O$ ≤ -3.5 ‰) were observed in the uppermost 25–30m of the water column at stations located in the deep Canada and Makarov Basins. The lowest $\delta^{18}O$ values were not found directly over the Alpha-Mendeleev Ridge - as observed in previous cruises - but slightly off its western flank. Values on top of the submarine ridge ranged from -3.9 to -2.8 ‰. Moving northward away from

the continental slope, $\delta^{18}O$ in the top 30m displayed a sharp horizontal gradient of approximately 2 per mil over 60–80 km along the northbound 180ºW section between stations 10 and 11. Along the southbound section, the horizontal gradient was -1.4–2.1‰. Measured $\delta^{18}O$ values in the UHW and LHW ranged between -1.4‰ and 1.4 ‰, and -0.4 to -0.5 ‰ respectively. The $\delta^{18}O$ = 0.0 isoline was observed at depths between 200 and 350 m, with the largest depth observed in the southern central Canada Basin and the shallowest in the Makarov Basin. Below this level, the AW displayed a remarkably homogeneous oxygen isotope ratio distribution (0.18 ± 0.02‰).

3.5 Discussion

Freshwater content is defined as the percentage deviation from a reference salinity and is proportional to the amount of zero-salinity water necessary for the measured sample salinity to match the reference value.

The Arctic Ocean is primarily composed of relatively warm, saline waters from the North Atlantic (Aagaard et al., 1989) to which fresher waters are added in form of river runoff, excess Precipitation over Evaporation (P-E), and low-salinity Pacific water entering through Bering Strait. Following Newton et al. (2013) we assume the Atlantic waters as the basic component of the Arctic Ocean ($S_{AW} = S_{ref} = 34.92$), and Pacific waters, river runoff and net precipitation as freshwater sources (Aagaard et al., 1989). Thus, we use the reference salinity (S_{ref}) of 34.92 to calculate the freshwater content of each water sample as expressed in Equation 3.a:

$$FW = \frac{(S_{ref} - S_{obs})}{S_{ref}} \% \qquad (3a)$$

Where (S_{obs}) is the measured salinity from CTD data and FW is the freshwater content in percent of the total volume (i.e, pure fresh water has a FW fraction of 100%, and Atlantic waters at the entry point to the Arctic in Fram Strait have a FW fraction of 0%). During GN01 20 ± 9% (range 9% to 38%) of the total FW inventory was contained in the mixed layer.

Our analysis of freshwater components requires information only available from bottle data, so it is important to compare FW fraction as computed with CTD salinities with that computed from the bottle samples. Since bottle data are often missing the top 5-7m of the water column, we computed the total FW content from both CTD and bottle data to quantify the average difference in the two methods (i.e., CTD salinity minus bottle salinities in Eq. 1). The total FW content from bottle data is on average 5% lower than that obtained from CTD data.

To estimate the total freshwater inventory per surface unit (m^2) at each hydrographic station, we vertically integrate the total freshwater content as a function of depth over the upper 500 meters of the water column (Eq. 3b). We first interpolate the FW data onto a 1-meter vertical grid applying a Piecewise Cubic Interpolation method, and then calculate the integrated freshwater content per surface unit, i.e., $m^2\ m^{-3}$ (Newton et al., 2013).

$$\mathrm{FWI}_{\mathrm{i}} = \int_{-500}^{0} \mathrm{FW}_{\mathrm{i}}\, \mathrm{dz} \qquad (3b)$$

Where the index *i* corresponds to the hydrographic station at which the integral is calculated. In other words, the FW inventory (FWI) at each station is equivalent to the height of a column of pure freshwater contained in the upper 500 meters at that location. The integral quantities provide a useful measure to discuss the total freshwater distribution in the Canadian Basin as well as its temporal variability.

3.5.1 Total Freshwater Content: GN01

The freshwater distribution in the Arctic Ocean is strongly related to the wind-driven horizontal gradients and steric height differences between the central basins and the shelf/marginal seas (Hunkins & Whitehead, 1992; Proshutinsky et al., 2002; Newton, et al. 2006). The stratification of the upper waters in the Canadian Basin is largely determined by the strength and location of the Beaufort Gyre, an anti-cyclonic circulation cell driven by the

atmospheric Beaufort High. The prevalent anti-cyclonic wind stresses over the Canadian Basin result in Ekman transport into the Beaufort Gyre, that in turn drives pooling of freshwater rich in meteoric water content.

The GN01 oceanographic survey includes two stations sampled in Eurasian Basin: stations 32 and 34, close to the North Pole, across the Lomonosov Ridge in the Amundsen Basin along the 150W section. Here, the upper halocline layer almost disappeared, and a sharp increase in the freshwater inventories by ca. 5m is observed. The latter is linked to the presence of the Transpolar Drift, a surface circulation branch flowing roughly along the Lomonosov Ridge from Siberia towards Greenland. Freshwater concentrations and inventories measured during the 2015 northbound (along 180ºW) and southbound (along 150ºW) transects are presented in Figure 16. As expected, the highest freshwater concentrations are found in the uppermost 10–20 meters of the water column and the largest freshwater inventories are observed at stations close to the Beaufort Gyre, between roughly 73.98ºN and 74.45ºN, independent of the longitude. Overall, the freshwater concentrations in the upper 20 meters along ranges from 10% to 35% with an average value of 20% (Figure 16). The same parameter ranges from 12 to 35 % and averages about 22% when only samples from the topmost 10 meters are included, largely corresponding to the mixed layer depth, with no significant difference between the two depth intervals. The maximum freshwater fractions (30–35%) were observed in the Chukchi Borderland (stations 8 to 11) along the 180ºW-track at depths shallower than 7 m. Along the 150ºW section, the largest freshwater concentrations (26–28%) were observed at stations 56 to 60 in the central Canada Basin. The timing of the sampling is an important variable to be considered when discussing the freshwater content and distribution as the surface stratification and the depth and properties of the mixed layer vary on seasonal cycle that is strongly correlated with that and melting/freezing of sea ice

(Morison and Smith, 1981; Toole et al., 2010; Polyakov et al., 2013). During the summer months, the mixed layer on average is shallower and fresher than it is during the winter, during and soon after sea ice formation. When new sea ice starts forming, brine rejection drives convection and causes the mixed layer to deepen (up to 30 m) and to become significantly more saline. The hydrographic stations along the northbound (180ºW) and southbound (150ºW) tracks were occupied between August 18th and August 31st, and September 8th and October 7th, respectively. Thus, a time span of approximately 40–45 days (1 to 1.5 month) separates the sampling dates of stations 8–11 and 56–60 during a crucial time for the dynamical and thermo-dynamical processes of the surface Canadian Basin.

The integrated freshwater values range from 9 to 23 meters (mean 17.2 ± 3.2 m) along the northbound section (180ºW), and between 4 and 29 meters (mean 17.2 ± 6.1 m) along the southbound track (150ºW). The maximal inventories were observed along 150 ºW in the central Canada Basin approximately between 73.0 ºN and 77.4 ºN, where the integrated height ranged between 25 and 30 meters.

Within this region, the 150 ºW freshwater inventories were 5 to 10 meters greater than along 180 ºW. The mean difference between the two transect was 3.4 ± 1.8 m. This offset reflects the typical freshwater distribution observed in the Western Arctic Ocean, the highest concentrations found in the central Canada Basin in correspondence of the Beaufort Gyre.

A large but highly variable percentage of total freshwater content is found in the mixed layer. In 2015 this percentage ranged from 5% to 80% and averaged to 16 ± 8% along 180ºW and 25 ± 14% along 150ºW.

The maximal freshwater inventories are observed along 150 ºW between stations 52 and 57, with values between 25 and 30 meters. In 2015 the freshwater inventories difference across sections of at roughly the same latitude ranged from 5 to 15 meters and was maximal at 74.8ºN.

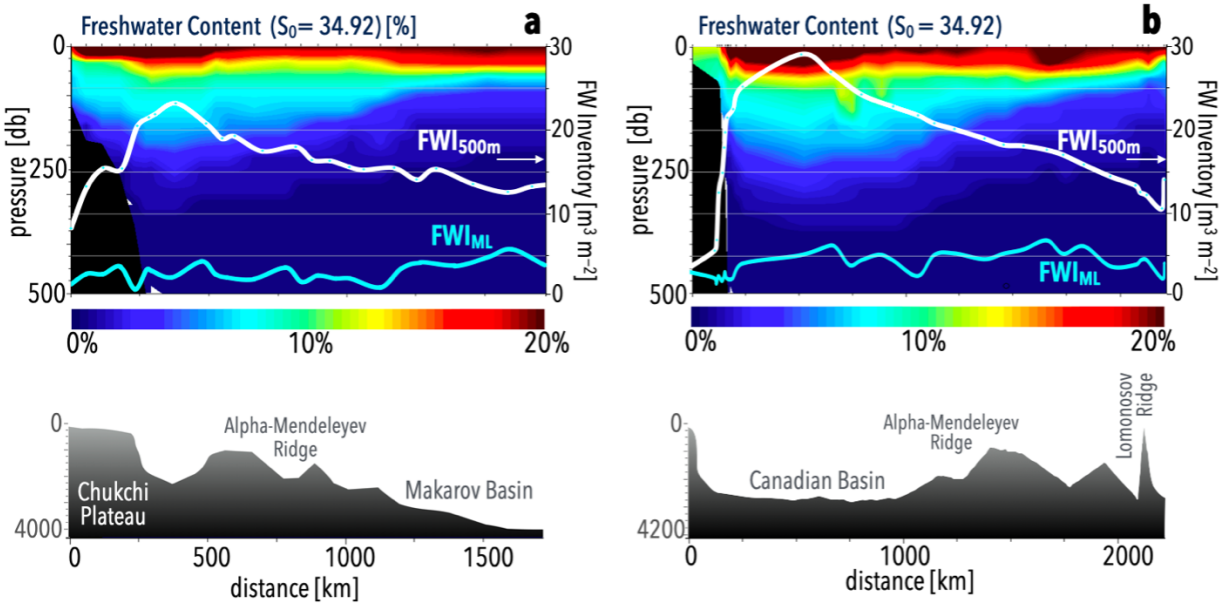

Figure 16. Freshwater (FW, relative to S_0 = 34.92) content from CTD data and vertical inventories in the upper 500 m and mixed layer for the 2015 cruise tracks. The northbound section (180ºW) is displayed in 3a is plotted along the distance from station 7 (north is shown on the right); the southbound section (150ºW) is displayed in Fig. 3b, plotted along distance from station 66. The integrated heights (FWI) in the upper 500m (mixed layer) are represented by white (cyan) line.

3.5.2 Water Component Distributions: GN01

To better capture the nature and the dynamics of the variability in the spatial and temporal distribution of freshwater, we have decomposed the freshwater content into its components: meteoric water (River Runoff plus net precipitation), sea-ice meltwater, and Pacific Water (Oestlund and Hut, 1984; Bauch et al., 1995; Jones et al., 1998; 2008; Ekwurzel et al. 2001; Yamamoto-Kawai et al., 2008; Newton et al., 2013).

The fractions of Atlantic Water, Pacific Water, meteoric water, and sea ice meltwater in each sample are calculated as follows:

$$
\begin{aligned}
&f_{\mathrm{Atl}}\mathrm{S}_{\mathrm{Atl}} + f_{\mathrm{Pac}}\mathrm{S}_{\mathrm{Pac}} + f_{\mathrm{Met}}\mathrm{S}_{\mathrm{Met}} + f_{\mathrm{SIM}}\mathrm{S}_{\mathrm{SIM}} = \mathrm{S}_{\mathrm{Obs}} \\
&f_{\mathrm{Atl}}\delta^{18}\mathrm{O}_{\mathrm{Atl}} + f_{\mathrm{Pac}}\delta^{18}\mathrm{O}_{\mathrm{Pac}} + f_{\mathrm{Met}}\delta^{18}\mathrm{O}_{\mathrm{Met}} + f_{\mathrm{SIM}}\delta^{18}\mathrm{O}_{\mathrm{SIM}} = \delta^{18}\mathrm{O}_{\mathrm{Obs}} \\
&f_{\mathrm{Atl}}\mathrm{ANP}_{\mathrm{Atl}} + f_{\mathrm{Pac}}\mathrm{ANP}_{\mathrm{Pac}} + f_{\mathrm{Met}}\mathrm{ANP}_{\mathrm{Met}} + f_{\mathrm{SIM}}\mathrm{ANP}_{\mathrm{SIM}} = \mathrm{ANP}_{\mathrm{Obs}} \\
&f_{\mathrm{Atl}} + f_{\mathrm{Pac}} + f_{\mathrm{Met}} + f_{\mathrm{SIM}} = 1
\end{aligned}
\qquad \text{(3c-3f)}
$$

Where f_{Atl}, f_{Pac}, f_{SIM}, and f_{Met} are the derived fractions of Atlantic Water, Pacific Water, sea ice meltwater, and meteoric water, respectively. $\mathrm{S}_{\mathrm{Atl}}$, $\mathrm{S}_{\mathrm{Pac}}$, $\mathrm{S}_{\mathrm{SIM}}$, and $\mathrm{S}_{\mathrm{Met}}$ are the assigned salinities of Atlantic Water, Pacific Water, sea ice meltwater, and meteoric water. $\delta^{18}\mathrm{O}_{\mathrm{Atl}}$, $\delta^{18}\mathrm{O}_{\mathrm{Pac}}$, $\delta^{18}\mathrm{O}_{\mathrm{SIM}}$, and $\delta^{18}\mathrm{O}_{\mathrm{Met}}$ are the chosen oxygen isotope ratios for the same water masses. $\mathrm{ANP}_{\mathrm{Atl}}$, $\mathrm{ANPO}_{\mathrm{Pac}}$, $\mathrm{ANP}_{\mathrm{SIM}}$, and $\mathrm{ANP}_{\mathrm{Met}}$ are the estimated values of for each water mass. $\mathrm{S}_{\mathrm{Obs}}$, $\delta^{18}\mathrm{O}_{\mathrm{Obs}}$, and $\mathrm{ANP}_{\mathrm{Obs}}$ are the measured values for each water sample. The end member choices used in our calculations are listed in Table 7 and have discussed in Ekwurzel et al. (2001), Newton et al. 2013 and references therein.

The uncertainties affecting the f_{Atl}, f_{Pac}, f_{SIM}, and f_{Met} concentrations estimates are ±0.14, 0.14, 0.02, and 0.02 respectively, and are the results of the end-member choices and the analytical error. The error on freshwater inventories, due to the fraction uncertainties and the added error from the vertical interpolation is less than 3m for the Pacific freshwater, 1 m for the meteoric water, and 0.5 for the sea ice meltwater.

Table 7. ***End Member Parameter Values.***

Water Mass	Salinity (g kg^{-1})	δ18O (‰)	Arctic N:P [a]
Atlantic Water	34.92 ± 0.03	0.3 ± 0.05	0
Pacific Water	32.50 ± 0.20	-1.1 ± 0.20	1
Meteoric Water	0	-20 ± 1	0
Sea-Ice Meltwater	4 ± 1	Surf. + 2.6 ‰	Surface

[a] Pacific Water: slope =14; intercept = -11; Atlantic Water: slope = 17; intercept = -2.

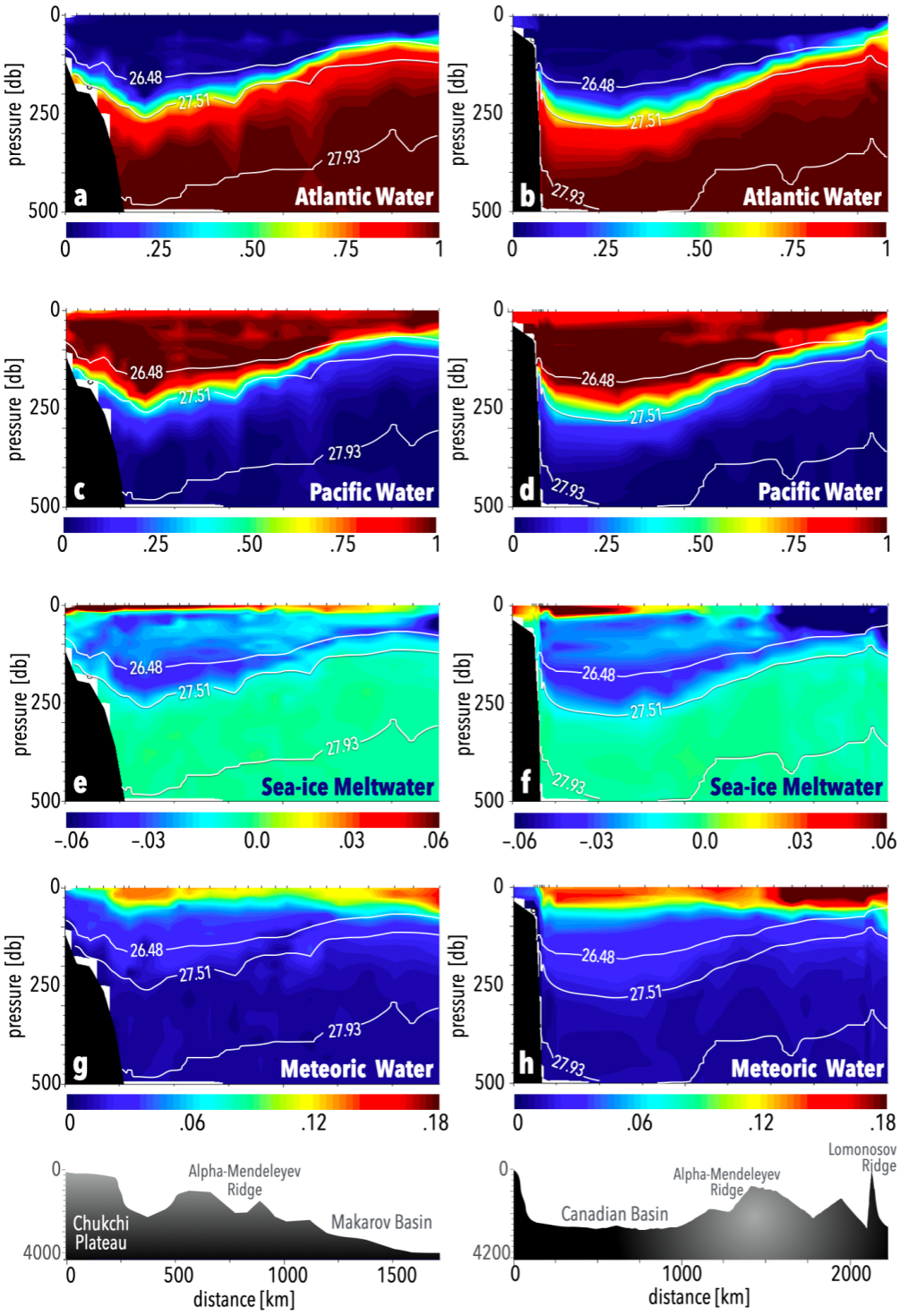

Figure 17. Water-mass fractions for GN01 2015 calculated using the Arctic N:P as tracer of Pacific inflow. Left panels show the water components along the northbound section following 180ºW. Right panels show upper 500m water components along the southbound track following 150ºW.

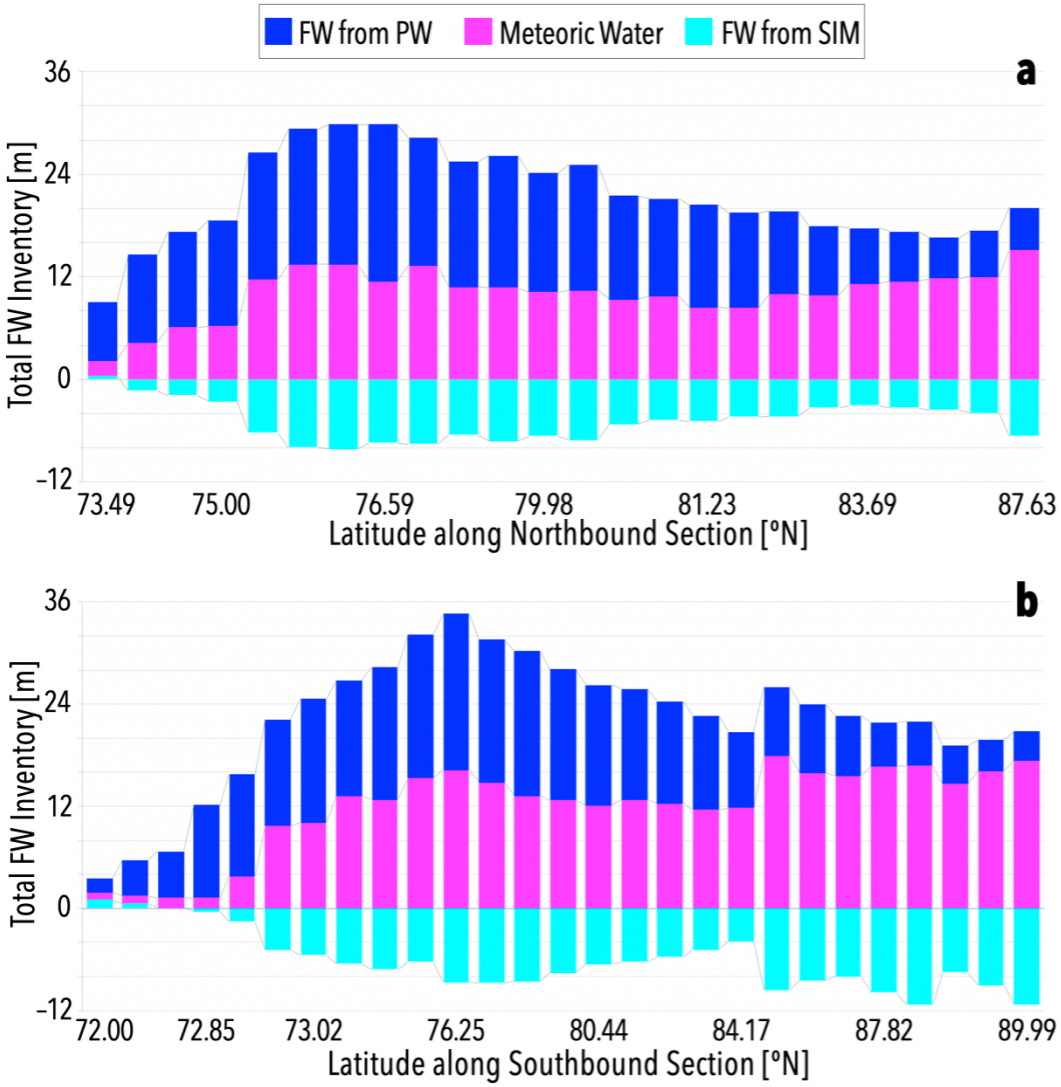

Figure 18. Freshwater component inventories calculated for the upper 500 m and plotted along latitude (south to north) along the GN01 sections. Freshwater from Pacific Water (blue), Meteoric Water (magenta), and Sea Ice Meltwater (cyan).

3.5.2.1 Atlantic Water

The vertical distributions of Pacific and Atlantic seawater fractions in the upper 500m are anticorrelated with the former predominantly occupying the upper 100–250m and the latter the bottom 150-500m (Figures 4a and 4b). The boundary between Pacific and Atlantic Waters approximately coincided with the lower boundary of the LHW ($\sigma_0 = 27.51$).

In 2015, the AW layer core was aligned with the $\sigma_0 = 27.93$ horizon. The Atlantic fraction was 85–100% in the portion of water column from this surface down to 500 m. At depths

shallower than the UHW (σ_0= 26.48), the content of AW is null within the method error (± 10%). Between these two isopycnals, the Atlantic component ranges between 20% and 65% (Figures 4a and 4b). The mean fraction of AW in the LHW was larger in the Makarov Basin (ca. 75%) than that observed in Canada Basin (60%), indicating a stronger interaction/ mixing between the two water masses.

Moving northward and toward the Lomonosov Ridge along the cruise tracks, the top of the layer of high AW fraction progressively shallowed from ca. 300 m to 100 m at the northernmost points in the Makarov Basin, and to 75 m at the North Pole. The AW integrated heights for the upper 500m (not shown) increased monotonically moving northward along both sections. Along the 180ºW, the AW inventory increases from 9 m at the Chukchi Shelf to 388–420 m in the northern Makarov Basin close to the Lomonosov Ridge. Along the 150ºW, the Atlantic layer was virtually absent at southernmost shallow stations (bottom ≤ 170 m) on the continental slope (distance ≤ 150 km) (Figures 16a, 16b).

3.5.2.2 Pacific Water

The distribution and pathways of Pacific Waters (PW) in the Canadian Basin are influenced by changes in the basin-wide atmospheric circulation, which can be viewed through the lens of large-scale climate modes (e.g., Proshutinsky and Johnson, 1997; McLaughlin et al., 2002; Steele et al., 2004, Newton, et al., 2006). A higher-than-normal sea-level pressure over the Canada Basin results in stronger Ekman convergence and Ekman pumping in the center of the Beaufort Gyre. Under these conditions, (anti-cyclonic years, low to neutral Arctic Ocean (AO) Index), PW recirculates and accumulates due to a spun-up and expanded Beaufort Gyre. Under a lower-than-normal pressure, (cyclonic years, high AO index), PW spreads laterally to the outer regions of the Canadian Basin, eventually exiting the Arctic Ocean via Fram Strait or the Canadian Archipelago (Steele et al., 2004; Jahn et al., 2010; Dodd et al., 2012). Whereas these

variations occur on timescales of years to decades, the PW storage in the Canadian Basin also displays a seasonal pattern, with stronger accumulation observed during winter months (McLaughlin et al., 2002; Bauch et al., 2011).

During 2015, upper halocline and surface waters were largely (85-100%) composed of PW. This Pacific layer (we defined the base of the layer as the depth of the 15% PW fraction isoline) exhibited the same pattern along both tracks: gradually increasing in depth from 100 ± 25 m at the continental slope to its maxima (225-250 m) at the center of the Beaufort Gyre before shallowing to 65 ± 10 m at the northernmost stations in the Makarov Basin. At Station 32, located at the North Pole in the Amundsen Basin, the layer of water containing high PW fractions (70-80%) was less than 10 meters deep. This finding agrees with previously established circulation patterns where the Transpolar Drift marks the easternmost lateral extent of PW across the Arctic Ocean (e.g., Jones, 2001; McLaughlin et al., 2002; Schlosser, et al., 2002, Steele et al., 2004). Over the Alpha-Mendeleev Ridge the PW isolines were more tightly spaced than in the inner basins and at the continental slope.

The PW distribution emerging from GN01 data is consistent with strengthened anticyclonic winds over the Canadian Basin, enhanced Ekman pumping, and PW accumulation (neutral to negative AO). Under these forcing conditions, the Beaufort Gyre expands towards the north and encompasses the Chukchi Abyssal Plain (Steele et al., 2004; Regan et al., 2019). While the Pacific layer progressively shoaled moving northwards along both section, waters with PW above 0.8 occupied the upper 75-100 m over the central Makarov Basin.

Researchers have identified a horizontal front between an “Western” and “Eastern” water-mass assemblage, with the Western stack containing an UHW layer. This front has been shown to move between the Lomonosov Ridge and the Makarov. (Morison et al., 2000;

Polyakov et al., 2004). While the Pacific layer progressively shoaled moving northwards along both sections, its base was found at depths between 75m and 100m well into the Makarov Basin. This feature suggests that during summer 2015 the Atlantic/Pacific front was located at an intermediate position between its natural alignment with the Lomonosov Ridge and the Alpha-Mendeleev Ridge consistent with the circulation regime described above.

In the Canada Basin, waters between the UHW and LHW isopycnals contained 30-40% of PW, while in the Makarov Basin these waters were almost largely depleted of PW (≤10%). A possible explanation is that the stronger-than-average downwelling at Beaufort Gyre center creates upwelling at gyre margins forcing AW to be entrained in the halocline layer.

3.5.2.3 Sea-Ice Meltwater

Along the northbound track, a thin lens of high sea-ice meltwater (SIM) fractions extended from the Chukchi Abyssal Plain to the western side of the Alpha-Mendeleev Ridge. The largest SIM concentrations (17% to 22%) were observed in the uppermost samples between stations 8 and 11. This high-SIM layer was still visible further north between station 12 and 17 but with lower fractions (7-8%) (Figure 16e). Along the southbound track a thin layer of SIM (6.5-9%) was present over the Alaskan continental shelf (Stations 57-64). These SIM peaks were the results of the summer melting and contained in a summer mixed layer ranging from 10 to 14 m thick (Figure 16f).

Below the surface layer, SIM fractions are everywhere negative, indicating a predominance of brines (sea-ice formation) over melt. Below the halocline, there is a slightly negative SIM signal, which varies little either horizontally or with depth. Over the Canada Basin, in the region impacted by the Beaufort Gyre and the Pacific Water plume, the halocline can be seen to have two local maxima of brine influence, separated by a region of less-negative SIM concentrations. The secondary minimum, at the base of the halocline, has valued reaching 3

to 6.5% brine, and is likely fed by spreading along isopycnals from the continental shelf. Water in the upper maximum, near the top of the upper halocline, is likely fed by isopycnal spreading (there are high concentrations of PW inflow there), but may also be enhanced from above, by diapycnal convection due to local sea-ice formation.

In the surface waters over the Lomonosov Ridge and the northern part of the Makarov Basin, along 150W, there is a very high brine formation signal (SIM -13% to -10%) between the surface and about 50m. These brine-enriched waters also had high meteoric water concentrations indicating that the sea ice formation had occurred in regions where the concentration of river discharge peaks. This signal is in the Trans-Polar Drift (TPD), and it is likely that the brine was formed in the Laptev and East Siberian seas and is being carried across the Arctic Ocean by the TPD.

3.5.2.4 Meteoric Water

The top 30-50 m of the water column contained most of the meteoric water with concentrations ranging between 10% and 19%. The typical meteoric water fraction profile displayed a steep decline from the surface to values of 2-3% at depths of 100 m followed by a gradual decline to values of 1-2% at 200 m and to less than 1% below 300 m (Figures 16g & 16h).

During the 2015 expedition hydrographic stations along 150ºW displayed larger concentrations of meteoric water extending to deeper depths than those along 180ºW at the same latitudes. The highest meteoric water concentrations (17-19%) were observed along the southbound track near the Lomonosov Ridge (Stations 32-38) which we interpret as the topographically trapped Trans-Polar Drift from Siberia toward Fram Straight. The discharge from the largest Eurasian Arctic rivers first flows eastward over the continental slope. It is deflected north along the saddle nodes where major submarine ridges connect with the

continental shelf (Anderson et al., 2004; Bauch et al., 1995, 2011; Newton et al., 2008). Near the Lomonosov Ridge, the 10% isoline was located at approximately 60 m. Data from Station 32 showed a unique profile with a gradual decline in meteoric water fraction and a deeper layer of high meteoric water concentration (100 m is still 8%). Thus, the TPD carries both a stronger and a deeper river runoff signal than the surrounding areas.

Over the Beaufort Gyre (Stations 46-64) the meteoric water fractions in the surface mixed layer ranged from 13% to 15%. The high meteoric water fraction layer was as deep as 50 m in the center of the gyre and gradually shoaled to 30 m approaching the continental slope. On the slope, the two shallow stations 62 and 63 (170-300 m) still carried a significant meteoric water signal (7-10%) at the surface.

Many different processes play a role in organizing the meteoric water sources and distribution and its seasonal and interannual variability: large-scale wind patterns, surface stress gradients in the marginal ice zones, changes PW inflow strength and properties, changes in river runoff or ice freeze/melt cycles, etc. The water mass inversion technique we used does not allow to separate the freshwater signal from Siberian rivers from that Northern American origin (Newton et al., 2013). Tracer-based studies used oxygen isotope ratios in combination with barium concentrations and found the meteoric water in central and southern Canada Basin to be predominantly of North American origin (e.g., Guay & Falkner, 1997; McClelland et al., 2012; Whitmore et al, 2020). Numerical outputs (Newton et al., 2008) and dynamic ocean topography patterns (Kwok & Morison, 2011) show that the signal of Siberian rivers can become entrained in the Beaufort Gyre adding freshwater to the upper Beaufort Sea. In separate efforts, the authors are working with colleagues form the Arctic GEOTRACES program to explore novel

ways to get more detailed and more precise component information from samples, but that work is beyond the scope of this manuscript.

3.5.3 Freshwater Inventories: GN01

The total freshwater content derived from salinity can also be calculated as sum of component contributions: meteoric water, Pacific inflow, and sea ice meltwater. Each water mass contributes to the total freshwater content proportionally to the offset $(S_0\text{-}S)/S_0$ between its average salinity and that of the reference water mass, Atlantic waters ($S_0 = 34.92$). Meteoric waters are completely fresh (S = 0), 100% of meteoric water content contributes to freshwater. We assume that the sea ice meltwater mean salinity is $S = 4 \pm 1$, its freshwater contribution (SIM-FW) is equal to ca. 88.55% the SIM fraction in each sample. The freshwater contribution from PW, with a nominal salinity of 31.5, is 6.93% of the total PW content. In this study, the difference between the total freshwater inventory calculated directly from salinity values and as the sum of freshwater components was negligible and in the order of $O(10^{-10})$.

The largest sources of freshwater in the Canadian Basin are the meteoric water and the Pacific inflow, with the former dominating in Canada Basin and that latter in the Makarov Basin. Moving north and away from the continental slope the freshwater contribution from PW sharply increased from 2-7 m to its peak values of ca. 18 m at 76.25ºN-75.59ºN and then gradually decreased to 4-6m near the Lomonosov Ridge.

Along the 180º track and south of or over the Alpha-Mendeleev Ridge (Stations 7-22) the PW freshwater inventories exceed the meteoric water inventories by 3m to 7m. In the Makarov Basin the meteoric water inventories were 5m to 10m larger than those of freshwater from PW, with the maximum difference (10m) observed at Station 30. Over the southern Canada Basin along 150ºW the difference between PW freshwater and meteoric water inventories ranged from

3m to 10m, peaking at the continental slope. Note that for several stations the interannual difference was smaller than the uncertainty in PW fraction (mean difference 1.5 m; uncertainty: 1.8m). These findings show that in 2015 the two freshwater sources were about equal in the Beaufort Gyre the region where the total freshwater was maximal. Over the Makarov Basin (150ºW) the meteoric water inventories were 8 m to 10 m greater than the Pacific freshwater integrals. In the Amundsen Basin (station 32) this difference was 14 m.

Integrated vertically, the brine content largely exceeded sea ice meltwater everywhere except over the southernmost shallow coastal stations (7, 65, and 66) where the SIM-FW inventories were positive and ranged between 0.5 and 1.0 m. The sea ice formation signal peaked over the central Canada Basin and in the Makarov Basin, and was minimum over the Alpha-Mendeleev Ridge. In the Canada Basin the SIM-FW inventories progressively decreased to a local minimum of -7.4 ± 0.5 m (-6.7 m to -7.75 m) (i.e.: maximum sea ice formation signal). The largest brine signal in central Canada Basin was approximately centered at 76.4ºN along 180ºW, and 77.5 along 150ºW. In this region the freshwater removal from ice formation was equal to 20-30% of the total freshwater storage measured at the same locations. At the Alpha-Mendeleev Ridge, the integrated SIM-FW ranged from -2.7 m to -3.4 m. Over the Makarov Basin we measured the overall maxima in brines: 8 ± 2 m with the maximum of 10 m at stations 37 and 32. North of the Alpha-Mendeleev Ridge the brine signal was as large as 50-70% (90% at station 32 in the Amundsen Basin) of the total freshwater. During the GN01 northbound transect the effect of brine rejection over the total freshwater budget in the Makarov Basin and over the Lomonosov Ridge was twice as strong along the southbound 150ºW track.

In 2015 over the central Canada Basin the Pacific freshwater and the meteoric water on average contributed 12.5 ± 2.5 m and 13.3 ± 3.34 m to the total freshwater respectively; and sea

ice formation removed 6.1 ± 1.4 m from the total freshwater. These results are in agreements with findings from previous literature (e.g., Yamamoto-Kawai et al. 2008: 10.5 m and 11.7 m, and 6.5 m respectively). The measured total freshwater storage within the Central Canada Basin (area ca. 1.6 10^6 km^2) was 31.6 ± 5.2 10^3 km^3; the breakdown in its sources and sinks was as follow: the Pacific freshwater added 21.2 ± 5.4 10^3 km^3 to the total freshwater inventory, the meteoric water for 20 ± 4 10^3 km^3, and 9.7 ± 2.3 were removed from by sea ice formation.

3.5.4 Comparisons with AOS94 and AOS05

In our analyses we compared the water mass concentrations and the freshwater inventories along the two 2015 transects with those computed for the overlapping 1994 and 2005 oceanographic sections. The 2015 180º northbound track was similar to the AOS94 and the southbound 150ºW track to the AOS2005. We constrained our comparisons to the regions where the stations from the distance between tracks was 60 km or less. Along 180ºW we used data from stations between 74.5 ºN and 87.5ºN: which included stations 9 to 29 from GN01 and stations 6 to 29 from AOS94. The comparison along 150ºW extends between 76.5ºN and 86ºN and includes stations 55 to 40 for GN01 and stations 8 to 25 for AOS2005. Temporal changes are displayed (1) as changes in the vertical distribution of water-mass components and (2) variations of the freshwater inventories. Before differencing sections, the two datasets are interpolated to the same horizontal and vertical grid. Section calculations were performed using the Java OceanAtlas 5.4.0 Beta 1.0 (by J. Osborne, D. Denbo, & J. Swift). For the inventories comparison we interpolated the selected stations onto a 0.5-degree latitude grid and computed the difference between the gridded datasets. Results are show in Figures 19 and 20.

3.5.4.1 Distribution Variability

In 2015 there were significant changes in the upper water column stratification compared to 1994 and lesser differences compared to 2005, with the greatest shifts observed in the Canada Basin (Figure 6). During 2015 the halocline layer occupied a larger portion of the water column compared to 1994. The UHW was approximately 100 m deeper than observed during AOS94 in the Canada Basin, and 30 m in the Makarov Basin. The core of the LHW was found at depths 75m to 125m deeper than in 1994 in the Canada Basin, and 25 m in the Makarov Basin. The shifts in the core of the AW layer depth were more prominent between the Mendeleyev Ridge the Chukchi Plateau (100m) than elsewhere along the 180ºW sections (30m).

When comparing 2015 with 2005, we found changes in the same direction but of lesser amplitude. In the Canada Basin, the UHW was 30 m deeper in 2015 than in 2005, and the LHW was 50m –75 m deeper in 2015 than in 2005. No significant changes in the halocline layer depth were observed ta stations located over the Alpha-Mendeleev Ridge and in the Makarov Basin. Variability in the large-scale conditions that modulate the strength of the Beaufort Gyre is an important driver of the observed shifts in the water column stratification.

During AOS94 water with a fraction of AW of the 0.8-AW-fraction isoline was centered at 130-150m in Canada Basin compared to 250-285 m in 2015; and shallowed to 80-90 m over and north of the Alpha-Mendeleev Ridge compared 100 to 150m in 2015. A substantial fraction of the Atlantic waters interacts with the halocline layer and is modified into less dense waters (Rudels et al. 2004). The contribution of Atlantic water to the upper part of the Canadian Basin water column was substantially larger during 1994 than in 2015.

The water column stratification in 2015 showed significant changes compared to 1994 and minor compared to 2005, with the greatest shifts centered in the Canada Basin (Figure 19). During 2015 the halocline layer occupied a larger portion of the water column compared to 1994.

The UHW was approximately 100 m deeper than observed during AOS94 in the Canada Basin, and 30 m in the Makarov Basin. The core of the LHW was found at depths 75m to 125m deeper than in 1994 in the Canada Basin, and 25 m in the Makarov Basin. The shifts in the core of the AW layer depth were more prominent between the Mendeleyev Ridge the Chukchi Plateau (100m) than elsewhere along the 180ºW sections (30m).

When comparing 2015 with 2005, we found changes in the same direction but of lesser amplitude. In the Canada Basin, the UHW was 30 m deeper in 2015 than in 2005, and the LHW was 50m –75 m deeper in 2015 than in 2005. No significant changes in the halocline layer depth were observed ta stations located over the Alpha-Mendeleev Ridge and in the Makarov Basin. Changes in the process of Ekman pumping due to the Arctic High anticyclonic circulation centered in the central Canada Basin are the major drivers of these stratification differences. Variability in the strength and position of Arctic High is correlated with the total freshwater content in the BG as well as with the mean pathways of the Pacific inflow in the Canadian Basin and the position of the transpolar drift.

During AOS94 water with a fraction of AW of the 0.8-AW-fraction isoline was centered at 130-150m in Canada Basin compared to 250-285 m in 2015; and shallowed to 80-90 m over and north of the Alpha-Mendeleev Ridge compared 100 to 150m in 2015. A substantial fraction of the Atlantic waters interacts the above layer and is modified into less dense waters (Rudels et al. 2004). Atlantic waters cross the Lomonosov Ridge and contribute to the lower Atlantic derived halocline in the Canadian Basin. The concentration of Atlantic to the upper part of the Canadian Basin water column was substantially larger during 1994 than in 2015.

3.5.5 Freshwater Inventory Variability

The 2015 total freshwater content in the central Canada and Makarov Basins was significantly greater than what measured during the 1994 and 2005 expeditions (Figure 20).

Along the 180ºW section, the GN01 data show an integrated freshwater column 5 to 11 m higher than that observed in AOS94, representing an average percentage change of 80%. The differences observed over the Canada Basin were approximately 2 m larger than those in the Makarov Basin. The freshwater integrated column variation along 150ºW was slightly smaller (3 to 7 m), equal to an average 27% change over 2005. The vertical changes in salinity (not shown) along 180ºW displayed 5-6% percentage decrease over the Canada Basin extending to roughly 200 m, and a stronger freshening (7 to 10%) in the Makarov Basin down to 75 m.

Compared with the 1994 and 2005 Arctic Ocean sections, the two GN01 transects displayed a significant increase in meteoric water both in the Canada and Makarov Basin (error: ± 1m). Meteoric water inventories along 180ºW were on average 4 m higher than the values observed in 1994, a 67% increase over 1994 (meteoric inventory average 6 m). The difference between these two periods peaked to 12 m in the southern Canada Basin, off the Chucky Shelf close to the continental shelf in correspondence of GN01 stations 11-16, was negligible over the Alpha-Mendeleev Ridge, and averaged 3 m over the Makarov Basin. When comparing the 2015 with 2005 along 150ºW we found an average increase of 5m with maximum values (10m) over the northern part of the section in the Makarov Basin. In 2005, the mean meteoric inventory in the studied region was 9 m compared to 14 m in 2015, corresponding to a percentage change of 50%.

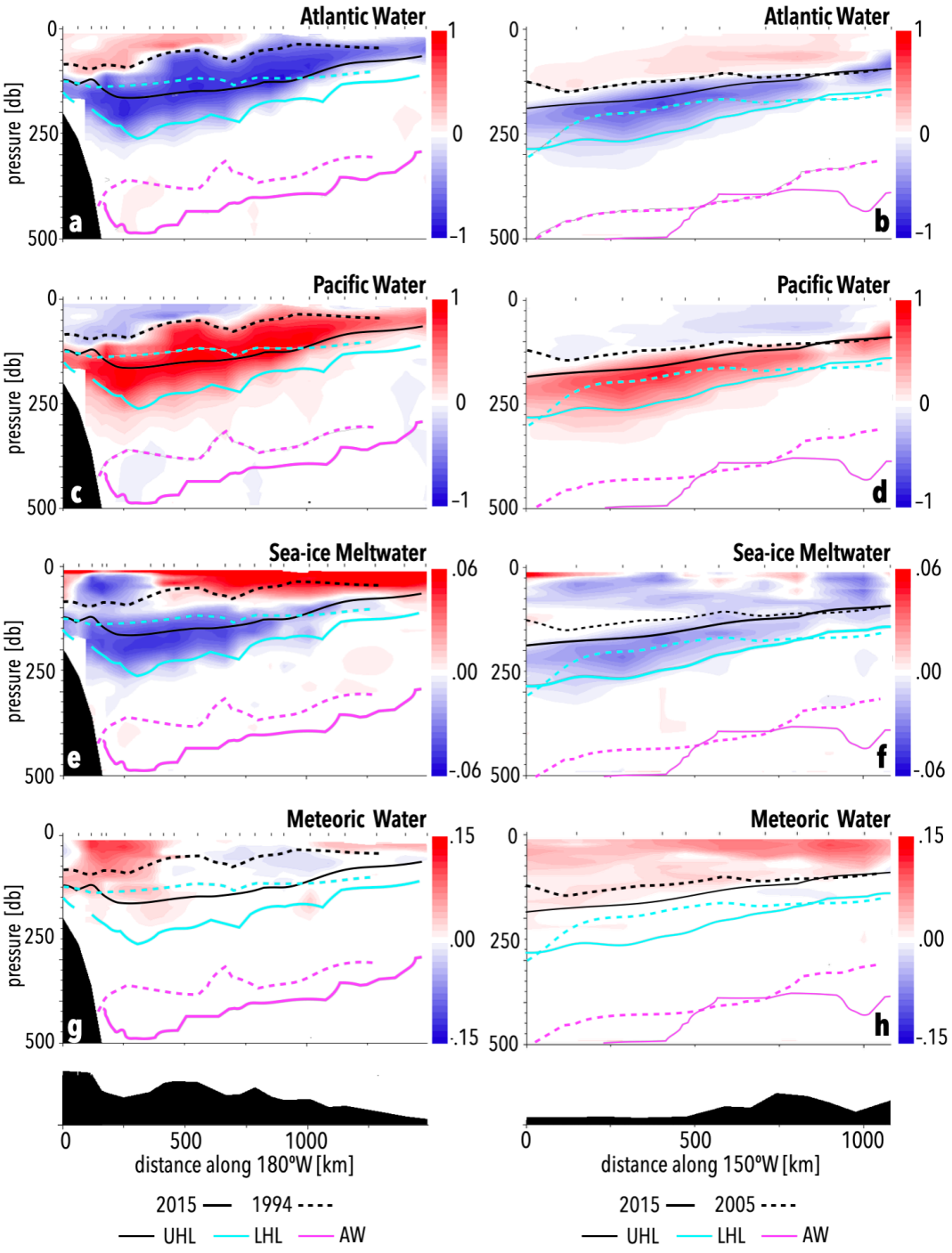

Figure 19. Water mass component variability in the upper 500 m. Left panels display the changes along 150ºW obtained by subtracting the 1994 results from the 2015 ones at overlapping stations (GN01: 8 to 30; AOS94: 6 to 29). Left panels show the differences between 2015 and 2005 (GN01: 55 to 40; Oden05: 8 to 25).

The river discharge into the Arctic Ocean is highly seasonal, with a July peak, and varies on an interannual time scale. Changes in this freshwater source are critical to the Arctic Ocean biology, circulation, and sea ice dynamics. Models and observations have found that an increased river runoff is positively correlated to enhanced summer melt and earlier freezing (Whitefield et al., 2015). Thus, to monitor and understand the dynamics of large changes in meteoric water storage and its distribution is of great importance especially as the global hydrological cycle accelerates.

The combined discharge from the largest Eurasian and North American rivers in 2015 was approximately 2,500 km^3; and 2,200 km^3 in 1994 (Holmes et al., 2018). An increase in river runoff of 300 km^3 approximately correspond to 1 m increase in meteoric water over the entire Canadian Basin. Newton et al. 2013 suggest that changes of this order of magnitude can only be partly explained by enhanced river discharge and that the variability in surface circulation features is the primary explaining cause. Indeed, changes in the local wind patterns can generate shifts in freshwater distribution that are 20 to 30 times larger than those from river influx variability (Dmitrenko et al., 2008).

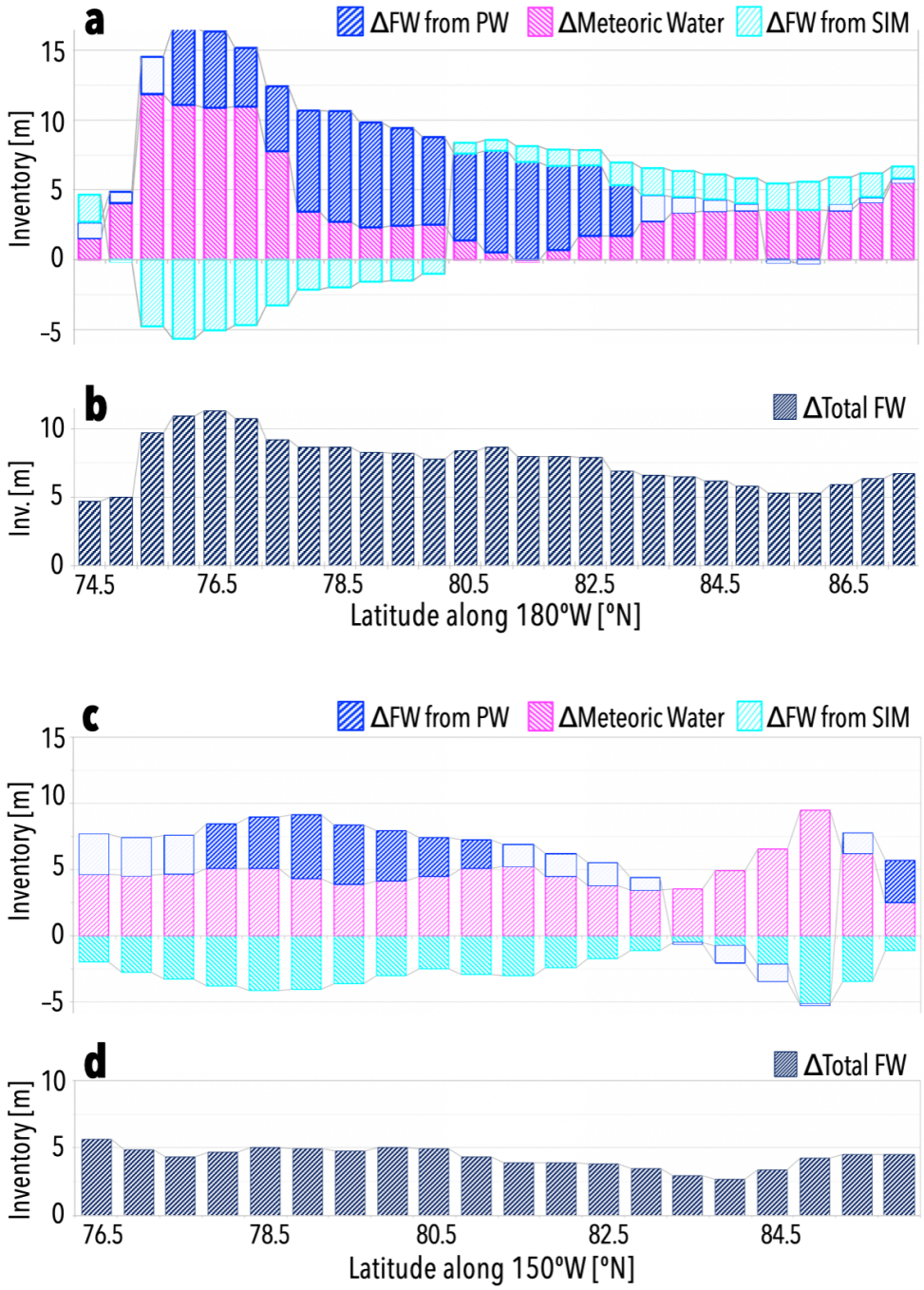

Figure 20. Temporal changes in the inventories of total freshwater and its components. Variations along 180ºW between GN01 and AOS94 are displayed in Figures 7a and 7b. Variations along 150ºW between GN01 and Oden05 are displayed in Figures 7c and 7d. Data have been interpolated on a horizontal grid of 0.5-degree latitude. Differences that are not statistically significant / smaller than the uncertainty level are displayed as white boxes (not sure how to describe it).

The distribution and stratification of PW was remarkably different in 2015 compared to 1994. The Pacific Layer was notably thinner and shallower in 1994 compared to 2015 and did not extend north of the Alpha-Mendeleev Ridge but remained primarily constrained to the Canada Basin. During AOS94 waters with PW fraction above 0.8 occupied the upper 200 m off the Chukchi Plateau slope and less than 50 m over the Makarov Basin compared to 150 m in 2015. The disappearance of PW in the Makarov Basin and a shoaling of the boundary between the Pacific and Atlantic-derived halocline waters during the mid 1990s has been reported in several previous studies (McLaughlin et al., 1996; Rudels et al., 2004).

Along 180ºW the difference in Pacific freshwater inventories and 1994 were on average 5 m and ranged between 2m and 8m. Changes in Pacific freshwater storages were not significant at the southernmost stations on the continental slope and over the northern Makarov Basin, north of 84ºN. The greatest shifts (6m-8m) were along the 500-km long region overlapping the Alpha-Mendeleev Ridge and accounted for a 120% fractional change over 1994 values. There were not significant variations in the PW freshwater inventories from 2005 to 2015 except for stations locates in the central Canada Basin. In this region, 2015 inventories were 3 m to 5 m higher than 2005 results, corresponding to a 20% to 40% increase over the 2005 mean of 12 m.

At the southernmost stations along 180ºW sections the 2015 SIM freshwater inventories were less negative compared to 1994, corresponding to a positive SIM freshwater inventory shift ranging from 1 m to 2.43 m. Note that negative values in SIM freshwater inventory indicate an increased brine injection (Figure 20). This offset can result from the fact that the high melting signal (SIM: 17%–22%) observed at the continental slope during GN01 was that absent in 1994. We also need to consider that the positive SIM values were constrained to the upper 5m-10m of the water column where AOS94 samples are significantly sparser than in 2015. Elsewhere in the

Canada Basin the In the Makarov Basin the 1994 brine inventories were 0.8 m to 2.2 m larger than in 2015 representing a 40% change. In this region the freshwater removal from sea ice formation was equal to ca. 60% of the total freshwater inventory in 1994 and only 20% in 2015.

The 2015 upper-500-m total freshwater inventory was on average 8.2 ± 0.37 m greater than it was observed in 1994, corresponding to a volumetric change of 12.5 ± 0.57 10^3 km^3 over the Canada Basin (area: ~ 1.5 10^6 km^2) and percentage change of 80%. The meteoric component accounted for 5.8 ± 0.52 (8.8 ± 0.80 10^3 km^3) equivalent to a 95% increase over the 1994 values. The Pacific freshwater component inventory increased on average by 4.6 ± 2.09 m (7.0 ± 3.18 10^3 km^3, a 56% increase over the 1994 values. Significant shifts in the Pacific freshwater component were only observed between from approximately 75ºN to 82.5ºN.

The accumulation of meteoric water was significantly stronger within the Beaufort Gyre region (station between 7; area: ~ 0.5 10^6 km^2) than along the entire 180ºW section (Figure 20a).

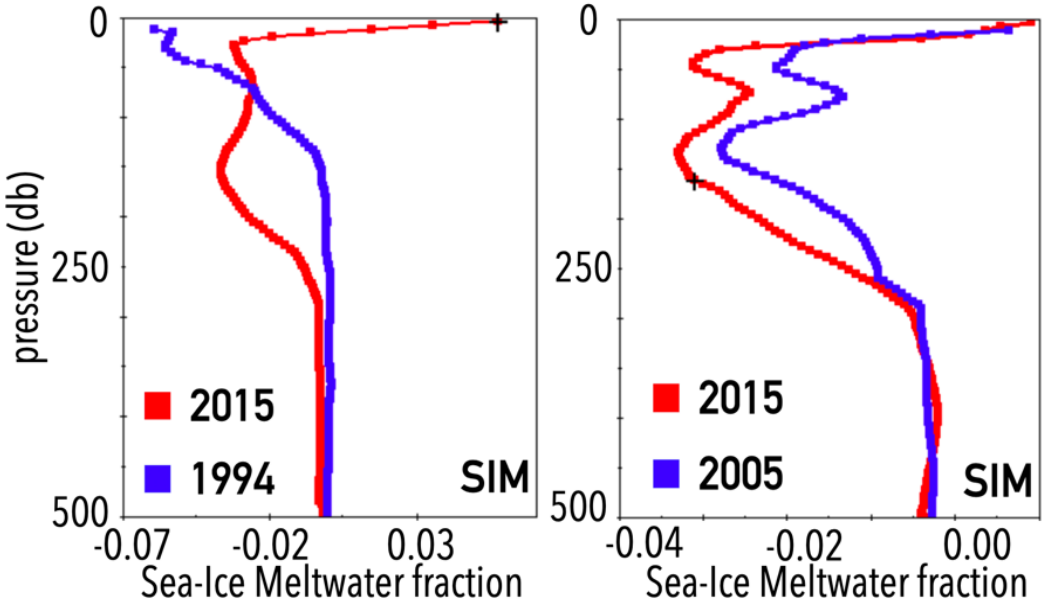

Figure 21. Mean SIM vertical profiles in the Canada Basin. Left panel: GN01 in red and AOS94 in blue. Right panel: GN01 in red and AOS05 in blue

In this area the average meteoric water accumulation was 7.3 ± 0.57 m equal to a 160% increase over the 1994 inventory in the same geographical region.

Averaging over the entire section (from 74.5ºN to 87ºN) the brine injection signal was 2.2 ± 0.26 m larger in 2015 than in 1994 (3.3 ± 0.40 10^3 km^3) in 2015 compared to 1994. The SIM inventory temporal changes assumed different signs over the 180ºW section. Below ca. 80ºN, in the sea ice formation signal was a stronger during GN01 than during AOS94, with additional 3.4 ± 0.26 m of freshwater removed from the water column. North of ca. 80ºN, the increase in meltwater was dominant with 0.8m to 1.5m added to freshwater inventory.

Typically, the sea ice meltwater is constrained to uppermost 20-40 meters of the water column. It is useful to break down the integral interval: from surface to 40m; and from 40m to 500m. The 2015 SIM inventory was 1.5 ± 0.10 m larger than the AOS94 integrated height. Brine accumulation dominated depths from 40 m to 500 m, with a mean inventory increase of 3.4 ± 0.37 m. These results are consistent with an enhanced annual sea ice cycle and the observed decline multiyear ice.

The 10-year shifts along 150ºW were consistently lesser than those observed along 180ºW between 1994 and 2015 and did not display enhanced variability in the Beaufort Gyre region. On average the total freshwater inventory increased by 4.2 ± 0.82 m corresponding to 6.4 ± 1.25 10^3 km^3 when integrated over the central Canada Basin; a 25 % increase over the inventory calculated from AOS05 data. The meteoric component increased by 53%, with a mean increase of 4.9 ± 0.55 m over the 2005 average integrated height (7.4 ± 0.84 10^3 km^3). When averaging over the entire section changes in Pacific freshwater were smaller than the uncertainty level. Freshwater removal from freezing was 2.6 ± 0.25 m greater in 2015 than during AOS05, corresponding to a volumetric increment of 4.0 ± 0.38 10^3 km^3 (+61%).

Along 150ºW the 2015 brine inventories were consistently larger than what observed in 2005 in the comparison region. The greatest increases in brine injection were over the central Canada and Makarov Basins ranging from 2.5 m to 4.7 m equal to a 100% percentage change. In correspondence of the Alpha-Mendeleev Ridge the difference was minimal (0.6 m). No significant variations in SIM (Figure 21).

Table 8. Summary of freshwater inventory changes in the Canada Basin[a].

180 ºW: 2015 minus 1994	**TFW**	**Met**	**Pac FW**	**SIM FW**
Inventory change (m)	8.2	5.8	4.6	-2.2
err (m)	0.37	0.52	2.09	0.26
Volume E03 km^3	12.5	8.8	7.0	-3.3
err (E03 km^3)	0.57	0.80	3.18	0.40
% change	80%	95%	56%	-54%

150 ºW: 2015 minus 2005	**TFW**	**Met**	**Pac FW**	**SIM FW**
Inventory change (m)	4.2	4.9	2.0	-2.6
err (m)	0.82	0.55	2.90	0.25
Volume E03 km^3	6.4	7.4	3.0	-4.0
err (E03 km^3)	1.25	0.84	4.42	0.38
% change	25%	53%	17%	-61%

3.6 Conclusions

Our analysis shows a significant freshening of the Canadian Basin, where the total freshwater reservoir increased by ca. 12,500 km^3 from 1994 to 2015, of which ca. 5,000 km^3 are within the Beaufort Gyre. This accumulation rate is consistent with the findings from independent studies (Haine et al., 2015; Carmack et al., 2016; Giles et al. 2012).

Increases in the meteoric water inventory were observed along both sections and can be attributed to changes in the wind-driven Ekman converge and in freshwater availability. Our calculations show that between 1994 and 2015 the meteoric water inventory increased on average by 5.8 m over the Canada Basin, and by 7.3 m in the Beaufort Gyre region. The 10-year

increment between GN01 and AOS05 was ca. 4.2 m. River runoff and net precipitation over the Arctic Ocean increased by ca. 8–10% between 1980 and 2010 (Haine et al., 2015; Holmes et al., 2016). Integrated over the central Canada Basin area this increment in inflows is equal to a 1 to 3-m increase and explains approximately 50% of the variability in meteoric water we found.

Pacific freshwater was the dominant component of the freshwater inventory observed during GN01. The 2015 Pacific freshwater inventory along 180 ºW was on average 2.5 ± 2.1 m higher than observed in 1994. Increments in the Beaufort Gyre region were ca. 11 m and significantly larger than elsewhere along the section. Independent studies indicate an increase in the Pacific inflow and Pacific freshwater inventory. Pacific inflow increased from 0.7 Sv to 1.2 Sv from 2001 to 2014, approximately a 70% increase (Woodgate et al., 2017). Haine et al. (2015) find an increase of 28% in the Pacific freshwater inventory between 2000 and 2010.

The melting signal in the upper 25 meters of the water column was significantly stronger in 2015 than in 1994. Variations were observed across the entire transect up to the northernmost stations in the Makarov Basin. We also observed an amplified brine injection from 50 to 300 meters compared to both 1994 and 2005. These changes are consistent with an enhanced sea ice cycle and expanded seasonal ice zones, trends recognized in previous studies (e.g., Newton et al., 2013).

The variability in freshwater distribution produced by shifts in the horizontal gradients of wind stress curl is potentially 20-30 times greater than variations from increases in the influxes (Dmitrenko et al., 2008). Newton et al. 2013 hypothesize that amplified freshwater availability can only partly explain variations in the freshwater component inventories of this scale and that shifts in surface circulation is the primary driver. Within the limits of our method, it is not possible to assert which process was the most important in driving the observed changes.

However, the water-mass decomposition analysis provides valuable information on the horizontal and vertical distribution of each freshwater component in the Arctic surface layer. The Arctic Ocean freshening is projected to continue during the 21st century, with an accumulation of ca. 50,000 km^3 by 2100 (Haine et al., 2015; Carmack et al., 2016).

Recent studies critique the method of computing freshwater budgets from a constant reference salinity (Treguier et al. 2014; Bauch and Losch, 2019) as intrinsically arbitrary and ambiguous, and argue that salt budget is a superior parameter as it is based on an absolutely quantity, is uniquely defined, and allows for more direct oceanographic interpretations and definite temporal and spatial comparisons. In this contribution we follow the geochemical approach, using nutrients and oxygen isotope ratios in combination with salinity to calculate the individual freshwater components. The geochemical approach has limitations from the inherent uncertainty in the end member choices and the non-conservative nature of nutrients. The total freshwater content values from the freshwater anomaly calculations and from the fraction calculations are the same within the analytical error (this study, Forryan et al, 2019). Although not absolute in nature, the presents tracer-based results offer insights on the variability and distribution of freshwater of different origin in the Canadian Basin. In combination with numerical simulations and salt budget calculations, freshwater components datasets can improve the understanding of the mechanisms driving freshwater accumulation and release in the western Arctic Ocean. The seasonal cycle of the Arctic freshwater budget is successfully reproduced by numerical simulations (e.g., Newton et al., 2006; Newton et al., 2008; Jahn et al., 2010; 2012; Karcher et al., 2012). Yet, the interannual variability of the liquid freshwater storage and its component distribution have proved more difficult to simulate and would benefit from repeated occupations of oceanographic sections and ideally quasi-synoptic surveys.

Conclusion or Epilogue

Our tracer-based analysis suggests that there is a significant variability in the freshwater components and UHL distribution while the major features of the circulation patterns and spreading velocities of the AW and the LHW have remained largely stable over the past decades. Future research should address whether in a fast changing Arctic, the dynamics of the surface layer will expand to the halocline and Atlantic layer substantially destabilizing the current Arctic Ocean water column with potentially dramatic consequences.

References

Aagaard, K., Coachman, L., & Carmack, E. (1981). On the halocline of the Arctic Ocean. Deep Sea Res., 28, 529–547.

Aagaard, K., Swift, J. H., & Carmack, E. C. (1985). Thermocline Circulation in the Arctic Mediterranean Seas. J. Geophys. Res., 90(C3), 4833–4846.

Aagaard, K., & Carmack, E. C. (1989). The Role of Sea Ice and Other Fresh Water in the Arctic Circulation. J. Geophys. Res., 94 (14), 485–498.

Aagaard, K., Weingartner, T., Danielson, S. L., Woodgate, R. A., Johnson, G. C., & Whitledge. T. E. (2006). Some controls on flow and salinity in Bering Strait. Geophys. Res. Lett., 33, L19602. https://doi.org/10.1029/2006GL026612

Aksenov, Y., Ivanov, V. V., Nurser, A. J. G., Bacon, S., Polyakov, I. V., Coward, A. C., Naveira-Garabato, A. C., & Beszczynska-Moeller, A. (2011). The Arctic Circumpolar Boundary Current. J. Geophys. Res., 116(C09017). https://doi.org/10.1029/2010JC006637

Aksenov, Y., Karcher, M., Proshutinsky, A., Gerdes, R., de Cuevas, B., Golubeva, E., & al. (2016). Arctic pathways of Pacific Water: Arctic Ocean Model Intercomparison experiments. Journal of Geophysical Research: Oceans, 121, 27–59. https://doi.org/10.1002/2015JC011299

Anderson, L. G., Bjork, G., Holby, O., Jones, E. P., Kattner, G., Koltermann, K. P., Liljeblad, B., Lindegren, R., Rudels, B. and Swift, J. (1994). Water masses and circulation in the Eurasian Basin: Results from the Oden 91 Expedition. Journal of Geophysical Research, 99, 3273-3283.

Bhatia, M. P., Kujawinski, E. B., Das, C. F. Breier, S. B., Henderson, P. B., & Charette, M. A. (2013). Greenland meltwater as a significant and potentially bioavailable source of iron to the ocean, Nat. Geosci., 6, 274–278. https://doi.org/10.1038/ngeo1746

Bauch, D., Schlosser, P., & Fairbanks, R. G. (1995), Freshwater balance and the sources of deep and bottom waters in the Arctic Ocean inferred from the distribution of $H_2{}^{18}O$, Prog. Oceanogr., 35, 53–80. https://doi.org/10.1016/0079-6611(95)00005-2

Bauch, D., Rutgers van der Loeff, M., Andersen, N., Torres-Valdes, S., Bakker, K., & Abrahamsen, E. P. (2011). Origin of Freshwater and polynyas water in the arctic Ocean halocline in summer 2007. Prog. Oceanogr., 482–495, https://doi.org/10.1016/j.pocean.2011.07.017

Bayer, R., Schlosser, P., Boenisch, P., Rupp, H., Zaucker, F., & Zimmek, G. (1989), Performance and blank components of a mass spectrometric system for routine measurement of helium isotopes and tritium by ^{3}He ingrowth method, Sitzungsber. Heidelb. Akad. Wiss. Math.-Naturwiss. Kl., 5, 241–279.

Bekryaev, R. V., Polyakov, I. V. & Alexeev, V. A. (2010). Role of polar amplification in long-term surface air temperature variations and modern Arctic warming. J. Clim. 23, 3888–3906.

Beszczynska-Möller, A., Fahrbach, E., Schauer, U., & Hansen, E. (2012). Variability in Atlantic water temperature and transport at the entrance to the Arctic Ocean, 1997–2010. ICES Journal of Marine Science, 69, 852–863.

Bluhm, B. A., Kosobokoba, K. N., & Carmack, E. C. (2015). A tale of two basins: An integrated physical and biological perspective of the deep Arctic Ocean. Prog. Oceanogr. https://doi.org/ 10.1016/j.pocean.2015.07.011

Broecker, W. S. (1974). "NO": A conservative water mass tracer. Earth Planet. Sci. Lett., 23, 100–107.

Carmack, E. C. (1990). Large-scale physical oceanography of Polar oceansi. In W.O. Smith, Jr., (Eds.), Polar Oceanography Part A (pp.171–212). San Diego, CA: Academic.

Carmack, E. C., Yamamoto-Kawai, M., Haine, T. W. N., Bacon, S., Bluhm, B. A., Lique, et al. (2016). Freshwater and its role in the Arctic Marine System: Sources, disposition, storage, export, and physical and biogeochemical consequences in the Arctic and global oceans. J. Geophys. Res. Biogeosci., 121, 675–717. https://doi.org/10.1002/2015JG003140

Clarke, W. B., Jenkins, W. J., & Top Z. (1976). Determination of Tritium by mass spectrometric measurements of 3He. International Journal of Applied Radiation and Isotopes, 27, 515–522.

Craig, H. (1961). Isotopic variations in meteoric waters, Science, 1, 33, 1702-1703.

Coachman, L. K., & Aagaard K. (1974). Physical oceanography of Arctic and sub-Arctic seas. Y. Herman (Eds.), Marine Geology and Oceanography of the Arctic Seas (pp. 1–72). Berlin: Springer-Verlag.

Coachman, L. K., & Barnes, C. A. (1963). The movement of Atlantic water in the Arctic Ocean. Arctic, 16, 8–16.

Codispoti, A., Kelly, V., Thessen, A., Matrai, P., Suttles, S., Hill, V., & Light, B. (2013), Synthesis of primary production in the Arctic Ocean: III. Nitrate and phosphate-based estimates of net community production, Prog. Oceanogr., 110, 126–150. https://doi.org/10.1016/j.pocean.2012.11.006

Comiso, J. C. (2012), The rapid decline of multiyear ice cover, J. Clim., 25, doi:10.1175/JCLI-D11-00113.1.

Comiso, J.C., & Hall, D.K. (2014). Climate trends in the Arctic as observed from space. Wiley Interdiscip. Rev. Clim. Chang., 5, 389–409.

Dai, A., & Trenberth, K. E. (2002). Estimates of freshwater discharge from continents: Latitudinal and seasonal variations, J. Hydrometeorol., 3, 660–687, https://doi.org/10.1175/1525-7541(2002)003<0660:EOFDFC>2.0.CO;2

de Steur, L., Hansen, E., Mauritzen, C., Beszczynska-Möller, A., & Fahrbach, E. (2014). Impact of recirculation on the East Greenland Current in Fram Strait: Results from moored current meter measurements between 1997 and 2009. Deep-Sea Research I, 92, 26–40. https://doi.org/10.1016/j.dsr.2014.05.018

Dmitrenko, I. A., I. V. Polyakov, S. A. Kirillov, L. A. Timokhov, I. E. Frolov, V. T. Sokolov, H. L. Simmons, V. V. Ivanov, and D. Walsh (2008). Toward a warmer Arctic Ocean: Spreading of the early 21st century Atlantic Water warm anomaly along the Eurasian Basin margins. J. Geophys. Res., 113(C05023). https://doi.org/10.1029/2007JC004158

Dmitrenko, I. A., B. Rudels, S. A. Kirillov, Y. O. Aksenov, V. S. Lien, V. V. Ivanov, U. Schauer, I. V. Polyakov, A. Coward, and D. G. Barber (2015). Atlantic water flow into the Arctic Ocean through the St. Anna Trough in the northern Kara Sea. Journal of Geophysical Research: Oceans, 120(5158–5178). https://doi.org/10.1002/2015JC010804

Dodd, P. A., Rabe, B., Hansen, E., Falck, E., Mackensen, A, Rohling, E., Stedmon, C., & Kristiansen, S. (2012). The freshwater composition of the Fram Strait outflow derived from a decade of tracer measurements, J. Geophys. Res., 117(C11005). https://doi.org/10.1029/2012JC008011

Ekwurzel, B., Schlosser, P., Mortlock, R. A., & Fairbanks, R. (2001). River runoff, sea ice meltwater, and Pacific water distribution and mean residence times in the Arctic Ocean. J. Geophys. Res., 106(5), 9075–9092.

Fairbanks, R. G. (1982). The origin of continental shelf and slope water in the New York Bight and Gulf of Maine: Evidence from $H_2/^{18}O/H_2{}^{16}O$ ratio measurements, J. Geophys. Res., 87, 5796–5808.

Falck, E., G. Kattner, G., & Budéus, G. (2005). Disappearance of Pacific Water in northwestern Fram Strait. Geophys. Res. Lett., 32, L14619. https://doi.org/10.1029/2005GL023400

Forryan, A., Bacon, S., Tsubouchi, T., Torres-Valdés, S., & Naveira Garabato, A. C. (2019). Arctic freshwater fluxes: sources, tracer budgets and inconsistencies. The Cryosphere, 13, 2111–2131. https://doi.org/10.5194/tc-13-2111-2019

Frank, M., Smethie Jr., W. M., & Bayer, R. (1998). Investigation of subsurface water flow along the continental margin of the Eurasian Basin using the transient tracers tritium, ^{3}He, and CFCs. J. Geophys. Res., 103, 773–792.

Giles, K., Laxon, S., Ridout, A., Wingham, D. J., & Bacon, S. (2012). Western Arctic Ocean freshwater storage increased by wind-driven spin-up of the Beaufort Gyre. Nature Geosci., 5: 194–197. https://doi.org/10.1038/ngeo1379

Gordon, L. I., Jennings Jr., J. C., Ross, A. A., & Krest, J. M. (1992). A suggested protocol for continuous flow automated analysis of seawater nutrients in the WOCE Hydrographic Program and the Joint Global Ocean Fluxes Study, Group Technical Report 92–1, OSU College of Oceanography Descriptive Chemical Oceanography.

Gonfiantini, R. (1978). Standards for stable isotope measurements in natural compounds, Nature, 271, 534-536, 1978.

Grotefendt, K., Logemann, K., Quadfasel, D., & Ronski, S. (1998). Is the Arctic Ocean warming?. Journal of Geophysical Research, 103(27), 679–687. https://doi.org/10.1029/98JC02097

Guay, C. K., & Falkner K. K. (1997). Barium as a tracer of Arctic halocline and river waters. Deep Sea Research Part II: Topical Studies in Oceanography, 44, 8, 1543–1569, https://doi.org/10.1016/S0967-0645(97)00066-0.

Haine, T. W. N., Curry, B., Gerdes, R., Hansen, E., Karcher, M., Lee, C., et al. (2015). Arctic freshwater export: Status, mechanisms, and prospects. Global and Planetary Change, 125, 13–35. https://doi.org/10.1016/j.gloplacha.2014.11.013.

Hallberg, R. (2013). Using a resolution function to regulate parameterizations of oceanic mesoscale eddy effects. Ocean Model, 72, 92–103. https://doi.org/10.1016/j.ocemod.2013.08.007

Hecht, M. W., & Smith, R. D. (2008). Toward a physical understanding of the North Atlantic: a review of model studies in an eddying regime. In M. W. Hecht, H. Hasumi (Eds.), Ocean Modeling in an Eddying Regime, Geophys. Monog. Series, Vol. 177, pp. 231–239).

Helland-Hansen, B., & Nansen, F. (1912). The sea west of Spitsbergen. Skr. Nor. Vidensk. Akad., Kl. 1 Mat. Naturvidensk. Kl., Vol. 12, pp. 89.

Holloway, G., (1987). Systematic forcing of large-scale geophysical flows by eddy-topography interaction. J. Fluid Mech., 184, 463–476.2

Holland, D. M., Mysak, L. A., & Oberhuber, J. M. (1996). An investigation of the general circulation of the Arctic Ocean using an isopycnal model. Tellus, Ser. A, 138–157.

Holloway, G. (1996). Neptune effect: statistical mechanical forcing of ocean circulation. In R. J. Adler, P. Müller, B. L. Rozovskii (Eds.), Stochastic Modelling in Physical Oceanography. Progress in Probability (Vol. 39). Boston, MA: Birkhäuser.

Holloway, G. (2004). From classical to statistical ocean dynamics. Surv. Geophys., 25, 203–219.

Holloway, G., Dupont, F., Golubeva, E., Hakkinen, S, Hunke, E., Jin, M., & al. (2007). Water properties and circulation in Arctic Ocean models. J. Geophys. Res., 112. https://doi.org/10.1029/2006JC003642

Holloway, G., & Wang, Z. (2009). Representing eddy stress in an Arctic Ocean model. J. Geophys. Res., 114. https://doi.org/ 10.1029/2008JC005169

Holmes, R. M., Shiklomanov, A. I., Suslova, A., Tretiakov, M., McClelland, J. W., Spencer, R. G. M., & Tank, S. E. (2018) River Discharge. In Arctic Report Card 2018. https://arctic.noaa.gov/Report-Card/Report-Card-2018

Hunkins, K. (1966). Ekman drift currents in the Arctic Ocean. Deep Sea Research and Oceanographic Abstr., 13, 607–620.

Hunkins, K., & Whitehead, J., A. (1992). Laboratory simulation of exchange through Fram Strait, J. Geophys. Res., 97(C7), 11,299–11,321. https://doi.org/ 10.1029/92JC00735

Ivanov, V. V., Polyakov, I. V., Dmitrenko, I. A., Hansen, E., Repina, I.A., Kirillov, S.A., & al. (2009). Seasonal variability in Atlantic Water off Spitsbergen. Deep Sea Research Part I: Oceanographic Research Papers, 56(1), 1–14. https://doi.org/10.1016/j.dsr.2008.07.013

Jahn, A., Tremblay, B., Newton, R., Holland, M. M., Mysak, L. A., & Dmitrenko, I. A. (2010). A tracer study of the Arctic Ocean's liquid freshwater export variability. J. Geophys. Res., 115(C07015). https://doi.org/10.1029/2009JC005873

Jahn, A., Aksenov, Y., de Cuevas, B. A., de Steur, L., Häkkinen, S., Hansen, E., et al. (2012). Arctic Ocean freshwater: How robust are model simulations?. Journal of Geophysical Research, 117, C00D16. https://doi.org/10.1029/2012JC007907

Jakobsson, M., Mayer, L. A., Coakley, B., Dowdeswell, J. A., Forbes, S., Fridman, B. et al. (2012). The International Bathymetric Chart of the Arctic Ocean (IBCAO) Version 3.0. Geophys. Res. Lett., 39(L12609). https://doi.org/ 10.1029/ 2012GL052219

Jenkins, W. J., & Clarke, W. B. (1976). The distribution of 3He in the Western Atlantic Ocean. Deep Sea Res., 23, 481–494.

Jones, E. P., & Anderson, L. G. (1986). On the origin of the chemical properties of the Arctic Ocean halocline. J. Geophys. Res., 91(C9), 10759–10767.

Jones, E. P., Anderson, L. G., & Swift, J. H. (1998). Distribution of Atlantic and Pacific waters in the upper Arctic Ocean: Implications for circulation. Geophys. Res. Lett., 25(6), 765–768.

Jones, E. P. (2001). Circulation in the Arctic Ocean. Polar Res., 20, 139–146. https://doi.org/10.1111/j.1751-8369.2001.tb00049.x

Jones, E. P., Swift, J. H., Anderson, L. G., Lipizer, M., Civitarese, G., Falkner, K. K., Kattner, G., & McLaughlin, F. A. (2003). Tracing Pacific water in the North Atlantic Ocean. J. Geophys. Res. 108(C4). https://doi.org/10.1029/2001JC001141

Jones, E. P., Anderson, L. G., Jutterstrom, S., Mintrop, L., & Swift, J. H. (2008). Pacific freshwater, river water and sea ice meltwater across Arctic Ocean basins: Results from

the 2005 Beringia Expedition. J. Geophys. Res., 113(CO8012). https://doi.org/10.1029/2007JC004124

Karcher, M. J., Oberhuber, J. M. (2002). Pathways and modification of the upper and intermediate waters of the Arctic Ocean. J. Geophys. Res, 107(3049). https://doi.org/ 10.1029/2000JC000530

Karcher, M. J., Gerdes, R., Kauker, F., & Köberle, C. (2003). Arctic warming – evolution and spreading of the 1990s warm event in the Nordic seas and in the Arctic Ocean. J. Geophys. Res., 108(3034). https://doi.org/10.1029/2001JC001265

Karcher, M., Kauker, F., Gerdes, R., Hunke, E., & Zhang, J. (2007). On the dynamics of Atlantic Water circulation in the Arctic Ocean. J. Geophys. Res., 112. https://doi.org/10.1029/2006JC003630

Karcher, M., I. Harms, W. J. F. Standring, M. Dowdall, and P. Strand (2010), On the potential for climate change impacts on marine anthropogenic and M. P. B. radioactivity in the Arctic regions, 60(8), 1151–1159, https://doi:10.1016/j.marpolbul.2010.05.003

Karcher, M., Smith, J. N., Kauker, F, Gerdes, R., & Smethie Jr., W. M. (2012). Recent changes in Arctic Ocean circulation revealed by iodine-129 observations and modeling. J. Geophys. Res., 117. https://doi.org/ 10.1029/2011JC007513

Kelly, S., Popova, E., Aksenov, Y., Marsh, R., & Yool, A. (2018). Lagrangian modeling of Arctic Ocean circulation pathways: Impact of advection on spread of pollutants. Journal of Geophysical Research: Oceans, 123. https://doi.org/ 10.1002/2017JC013460

Killworth, P. D., Stainforth, D., Webb, D. J., & Paterson S. M. (1991). The development of a free surface Bryan Cox Semtner ocean model. J. Phys. Oceanogr., 21, 1333–1348. https://doi.org/ 10.1175/1520-0485

Kwok, R., & Rothrock, D. A. (2009). Decline in Arctic sea ice thickness from submarine and ICES at records: 1958-2008. Geophys. Res. Lett., 36. https://doi.org/10.1029/2009GL039035

Loeng, H., V., Ozhigin, & Ådlandsvik, B. (1997). Water fluxes through the Barents Sea ICES. Journal of Marine Science, 54, 310–317.

Lucas, L. L., & Unterweger, M. P. (2000). Comprehensive Review and Critical Evaluation of the Half-Life of Tritium. Journal of Research of the National Institute of Standards and Technology, 105.

Ludin, Andrea; Weppernig, R., Boenisch, G., & Schlosser, P. (1997), Mass Spectrometric Measurement of Helium Isotopes and Tritium in Water Samples. Interdisciplinary Earth Data Alliance (IEDA). https://doi.org/10.1594/IEDA/100661

Madec, G. (2014). ‘‘NEMO Ocean Engine’’ Note du Pôle de modelisation (No. 27, ISSN: 1288–1619.). Paris: Institut Pierre-Simon Laplace.

Mahlstein, I., & Knutti R. (2012). September Arctic sea ice predicted to disappear near 2ºC global warming above present. J. Geophys. Res., 117, DO6014. https://doi.org/10.1029/2011JD016709

Marnela, M., Rudels, B., Houssais, M. N., Beszczynska-Möller, A., & Eriksson, P. (2013). Recirculation in the Fram Strait and transports of water in and north of the Fram Strait derived from CTD data. Ocean Sci., 9.

Maslowski, W., Clement Kinney, J. D., Marble, C., & Jakacki, J. (2008). Towards eddy resolving models of the Arctic Ocean. In M. W. Hecht, H. Hasumi (Eds.), Ocean Modeling in an Eddying Regime, Geophys. Monogr. Ser. (Vol. 177, pp. 241–264). Washington, DC: AGU.

Maslowski, W., Newton, R., Schlosser, P., Semtner, A., & Martinson, D. (2000). Modeling recent climate variability in the Arctic Ocean. Geophysical Research Letters, 27(22), 3743–3746. https://doi.org/10.1029/1999GL011227

Mauldin, A., Schlosser, P., Newton, R., Smethie Jr., W. M., Bayer, R., Rhein, M., & Jones, E. P. (2010). The velocity and mixing time scale of the Arctic Ocean Boundary Current estimated with transient tracers. J. Geophys. Res., 115(C08002), https://doi.org/10.1029/2009JC005965

Mauritzen, C., Hansen, E., Andersson, M., Berx, B., Beszczynska-Möller, A., Burud, I., et al. (2011). Closing the loop-approaches to monitoring the state of the Arctic Mediterranean during the International Polar Year 2007–2008. Progress in Oceanography, 90, 62–89. https://doi.org/10.1016/j.pocean.2011.02.010

McClelland, J. W., Holmes, R. M., Dunton, K. H., & Macdonald, R. W. (2012). The Arctic Ocean Estuary. Estuaries and Coasts 35, 353–368. https://doi.org/10.1007/s12237-010-9357-3

Macdonald, R. W., Carmack, E. C., McLaughlin, F. A., Falkner, K. K., Swift, J.H. (1999). Connections among ice, runoff, and atmospheric forcing in the Beaufort Gyre. Geophys. Res. Lett., 26, 2223–2226.

Macdonald, R.W., Kuzyk, Z.A., & Johannessen, S.C. (2015). It is not just about the ice: a geochemical perspective on the changing Arctic Ocean. J. Environ. Stud. Sci., 5, 288–301. https://doi.org/10.1007/s13412-015-0302-4

McLaughlin, F., Carmack, E. C., & Macdonald, R. (2002). The Canada Basin, 1989–1995: Upstream events and far-field effects of the Barents Sea. J. Geophys. Res., 107(C7), 3082.

McLaughlin, F. A., Carmack, E. C., Macdonald, R. W., Melling, H., Swift, J. A., Wheeler, P. A., Sherr, B. F. & Sherr, E. B. (2004). The joint roles of Pacific and Atlantic-origin waters in the Canada Basin, 1997–1998. Deep Sea Res., Part I, 107–128. https://doi.org/10.1016/j.dsr.2003.09.010

McPhee, M. G., Kikuchi, T., Morison, J. H., & Stanton, T. P. (2003). Geophys. Res. Lett. 30, 2274.

McPhee, M. G., Proshutinsky, A., Morison, J. H., Steele, M., & Alkire, M. B. (2009). Rapid change in freshwater content of the Arctic Ocean." Geophys. Res. Lett., 36.

Meredith, M.M., Sommerkorn, S., Cassotta, C., Derksen, A., Ekaykin, A., Hollowed, & al. (2019) In: Pörtner, H.-O., Roberts, D.C., Masson-Delmotte, V., Zhai, P., Tignor, M., Poloczanska, E., Mintenbeck, K., Alegría, A., Nicolai, M., Okem, A., Petzold, J., Rama, B., & Weyer, N. M., (eds.) Polar Regions. IPCC Special Report on the Ocean and Cryosphere in a Changing Climate. https://www.ipcc.ch/srocc/chapter/chapter-3-2/

Merryfield, W. J., and R. B. Scott (2007). Bathymetric influence on mean currents in two high-resolution near-global ocean models. Ocean Modell., 16, 76– 94. https://doi.org/10.1016/j.ocemod.2006.07.005

Morison, J., & Smith, J. D. (1981). Seasonal variations in the upper Arctic Ocean as observed at T-3, Geophys. Res. Lett., 8(7), 753– 756, https://doi.org/10.1029/GL008i007p00753

Morison, J., Steele, M., & Andersen, R. (1998). Hydrography of the upper Arctic Ocean measured from the nuclear submarine U.S.S. Pargo. Deep-Sea Research I, 45, 15–38.

Morison, J., K. Aagaard, and M. Steele (2000). Recent environmental changes in the Arctic: a review. Arctic, 53 (4), 359–371.

Morison, J., Kwok, R., Peralta-Ferriz, C., Alkire, M., Rigor, I., R. Andersen, & Steele, M. (2012). Changing Arctic Ocean freshwater pathways. Nature, 481.

Münchow, A., Falkner, K., & Melling H. (2007). Spatial continuity of measured seawater and tracer fluxes through Nares Strait, a dynamically wide channel bordering the Canadian Archipelago. Journal of Marine Research, 65, 759–788. https://doi.org/10.1357/002224007784219048

Murray, M. S., Anderson, L., Cherkashov, G., Cuyler, C., Forbes, B., Gascard, et al. (2010). International Study of Arctic Change (ISAC): Science Plan. Stockholm: ISAC International Program Office.

Nansen, F. (1902). Oceanography of the North Polar Basin, The Norwegian North Polar Expedition 1893–1896. Scientific Results, 427 pp.

Nazarenko, L., Holloway, G., & Tausnev, N. (1998). Dynamics of transport of 'Atlantic signature' in the Arctic Ocean. J. Geophys. Res., 103, 31003–31015. https://doi.org/10.1029/1998JC900017

Newton, J. L., & Sotirin B. J. (1997). Boundary undercurrent and water mass changes in the Lincoln Sea. J. Geophys. Res., 102, 3393–3403. https://doi.org/10.1029/96JC03441

Newton, B., Tremblay, L. B., Cane, M. A., & Schlosser, P. (2006). A simple model of the Arctic Ocean response to annular atmospheric modes. J. Geophys. Res., 111, C09019. https://doi.org/10.1029/2004JC002622

Newton, R., Schlosser, P., Martinson, D. G., & Maslowski, W. (2008). Freshwater distribution in the Arctic Ocean: Simulation with a high- resolution model and model-data comparison. J. Geophys. Res., 113(C05024). https://doi.org/10.1029/2007JC004111

Newton, R., Schlosser, P., Mortlock, R., Swift, J. A., & MacDonald, R. W. (2013). Canadian Basin freshwater sources and changes: Results from the 2005 Arctic Ocean Section. J. Geophys. Res. Oceans, 118, 2133–2154. https://doi.org/10.1002/jgrc.20101

Nikolopoulos, A., Pickart, R. S., Fratantoni, P. S., Shimada, K., Torres, D. J., & Jones, E. P. (2009). The western Arctic boundary current at 152 °W: Structure, variability, and transport. Deep Sea Res. Part II, 56, 1164–1181. https://doi.org/10.1016/j.dsr2.2008.10.014

Nurser, A. J. G., & Bacon, S. (2014). The Rossby radius in the Arctic Ocean. Ocean Sci., 10, 967–975. https://doi.org/10.5194/os-10-967-2014

Östlund, H. G. (1982). The residence time of the freshwater component in the Arctic Ocean. J. Geophys. Res., 87, 2035–2043.

Overland, J., Francis, J., Hall, R., Hanna, E., Kim, S.-J., & Vihma, T. (2015). The melting Arctic, the polar vortex and mid-latitude weird weather: Are they connected?. J. Climate. https://doi.org/doi:10.1175/JCLI-D-14-00822.1

Overpeck, J. T., & al. (2005). Arctic system on trajectory to new, seasonally ice free state, EOS Trans. Am. Geophys. Union, 86(34), 309–316. https://doi.org/oi:10.1029/2005EO340001

Pasqualini, A., Schlosser, P., Newton, R., Koffman, T. N. (2017). U.S. GEOTRACES Arctic Section Ocean Water Hydrogen and Oxygen Stable Isotope Analyses, Version 1.0. Interdisciplinary Earth Data Alliance (IEDA). https://doi.org/10.1594/IEDA/100633

Perovich, D., Meier, W., Tschudi, M., Farrell, S., Hendricks, S., Gerland, S., Kaleschke, L., Ricker, R., Tian-Kunze, X., Webster, M., & Woods, K. (2019). Sea ice. 2019 Arctic Report Card. Retrieved from: https://arctic.noaa.gov/Report-Card/Report-Card-2019

Pfirman, S. L., Bauch, D., & Gammelsrod, T. (1994). The northern Barents Sea: Water mass distribution and modification. In The Polar Oceans and Their Role in Shaping the Global Environment: The Nansen Centennial Volume. Geophys. Monogr. Ser. 85.

Pnyushkov, A. V., Polyakov, I.V., Ivanov, V.V., Aksenov, Y., Coward, A. C., Janout, M., & Rabe, B. (2015). Structure and variability of the boundary current in the Eurasian Basin of the Arctic Ocean. Deep-Sea Research, I, 80–97. https://doi.org/10.1016/j.dsr.2015.03.001

Pnyushkov, A., Polyakov, I.V., & Kikuchi T. (2013). Structure of the Fram Strait branch of the boundary current in the Eurasian Basin of the Arctic Ocean. Polar Sci. 7(2),53–71. http://dx.doi.org/10.1016/j.polar.2013.02.001

Polyakov, I. V., Alekseev, G. V., Bekryaev, R. V., Bhatt, U., Colony, R. L., Johnson, M. A., et al. (2002). Observationally based assessment of polar amplication of global warming. Geophys. Res. Lett., 29(18), 1878. https://doi.org/10.1029/2001GL011111

Polyakov, I. V., Alekseev, G. V., Timokhov, L. a., Bhatt, U. S., Colony, R. L., Simmons, H. L., et al. (2004). Variability of the intermediate Atlantic Water of the Arctic Ocean over the last 100 years. Journal of Climate, 17, 4485– 4497. https://doi.org/10.1175/JCLI-3224.1

Polyakov, I. V., Beszczynska, A., Carmack, E. C., Dmitrenko, I. A., Fahrbach, E., Frolov, I. E. (2005). One more step toward a warmer Arctic. Geophys. Res. Lett., 32(L17605). https://doi.org/10.1029/2005GL023740

Polyakov, I. V., Timokhov, L. A., Alexeev, V. A., Bacon, S., Dmitrenko, I. A., Fortier, L., et al. (2010). Arctic Ocean Warming Contributes to Reduced Polar Ice Cap. J Phys. Oceanogr., 40. https://doi.org/ 10.1175/2010JPO4339.1

Polyakov, I. V., Pnyushkov, A. V., & Timokhov, L. A. (2012). Warming of the Intermediate Atlantic Water of the Arctic Ocean in the 2000s. J. Climate, 25, 8362–8370. https://doi.org/10.1175/JCLI-D-12-00266.1

Polyakov, I. V., Bhatt, U. S., Walsh, J. E., Abrahamsen, E. P., Pnyushkov, A. V., & Wassmann, P. F. (2013). Recent oceanic changes in the Arctic in the context of long-term observations. Ecol. Appl., 23, 1745–1764.

Polyakov, I. V., Pnyushkov, A. V., Alkire, M. B., Ashik, I. M., Baumann, T. M., Carmack, E. C., et al. (2017). Greater role for Atlantic inflows on sea-ice loss in the Eurasian Basin of the Arctic Ocean. Science, 356(6335), 285–291. https://doi.org/\10.1126/science.aai8204

Polyakov, I. V., Rippeth, T. P., Fer, I., Alkire, M. B., Baumann, T. M., Carmack, E. C., Ingvaldsen, R., Ivanov, V. V., Janout, M., Lind, S., and Padman, L. (2020). Weakening of cold halocline layer exposes sea ice to oceanic heat in the eastern Arctic Ocean. J. Clim., 33, 8107–8123.

Pond, S., & Pickard, G. L. (1983) Introductory dynamical oceanography. 3rd Edition, Pergamon Press, Oxford.

Proshutinsky, A. Y., & Johnson, M. A. (1997), Two circulation regimes of the wind-driven Arctic Ocean, J. Geophys. Res., 102(C6), 12, https://doi.org/10.1029/97JC00738

Proshutinsky, A., Bourke, R. H., & McLaughlin, F. A. (2002), The role of the Beaufort Gyre in Arctic climate variability: Seasonal to decadal climate scales. Geophys. Res. Lett., 29(23), 2100, https://doi.org/10.1029/2002GL015847

Proshutinsky, A., Krishfield, R., Timmermans, M. -L., Toole, J., Carmack, E. C., McLaughlin, F., & al. (2009). The Beaufort Gyre Fresh Water Reservoir: State and variability from observations. J. Geophys. Res. https://doi.org/10.1029/2008JC005104

Proshutinsky, A., Dukhovskoy, D., Timmermans, M.-L., Krishfeld, R., & Bamber, J. L. (2015). Arctic circulation regimes. Philosophical Transactions of the Royal Society A, 373, 20140160. https://doi.org/10.1098/rsta.2014.0160

Proshutinsky, A., Krishfield, R., Toole, J. M., Timmermans, M.-L., Williams, W., Zimmermann, S., M. Yamamoto-Kawai, & al. (2019). Analysis of the Beaufort Gyre freshwater content in 2003–2018. J. Geophys. Res.: Oceans, 124, 9658–9689. https://doi.org/10.1029/2019JC015281

Quadfasel, D., Sy, A., Wells, A. D., & Tunik, A. (1991). Warming in the Arctic. Nature, 350–385.

Regan, H. C., Lique, C., & Armitage, T. W. K. (2019). The Beaufort Gyre extent, shape, and location between 2003 and 2014 from satellite observations. Journal of Geophysical Research: Oceans, 124, 844–862. https://doi.org/10.1029/2018JC014379

Roether, W. (1970). Water-CO2 exchange set-up for the routine ^{18}O assay of natural waters, Int. J. Appl. Rad. Isotopes, 21, 379–387.

Rudels, B., Larsson, A. M., & Sehlstedt, P. I. (1991). Stratification and water mass formation in the Arctic Ocean: Some implications for the nutrient distribution. Polar Res., 10, 19–32.

Rudels, B., Jones, E. P., Anderson, L. G., & Kattner, G. (1994). On the intermediate depth waters of the Arctic Ocean, In O. M. Johannessen, R. D. Muench, J. E. Overland (Eds.), The Polar Oceans and Their Role in Shaping the Global Environment: The Nansen Centennial Volume. The Polar Oceans and Their Role in Shaping the Global Environment, Geophysical Monograph, 85 (pp. 33–46). Washington, DC: AGU.

Rudels, B., Anderson, L. G., & Jones E. P. (1995). Formation and evolution of the surface mixed layer and halocline of the Arctic Ocean. J. Geophys. Res., 101, 8807–8821. https://doi.org/10.1029/96JC00143

Rudels, B., Friedrich, H. J., & Quadfasel, D. (1999). The Arctic circumpolar boundary current. Deep Sea Res., Part II, 46, 1023–1062. https://doi.org/10.1016/S0967-0645(99)00015-6

Rudels, B., Meyer, R., Fahrbach, E., Ivanov, V. V., Østerhus, S., & Quadfasel, D. (2000). Water mass distribution in Fram Strait and over the Yermak Plateau in summer 1997. Annales Geophysicae, European Geosciences Union (EGU), 18(6), 687–705. https://doi.org/ https://hal.archives-ouvertes.fr/hal-00316683

Rudels, B., Muench, R. D., & Gunn, J. (2000). Evolution of the Arctic Ocean boundary current north of the Siberian shelves. J. Mar. Syst., 25(1), 77–99. https://doi.org/10.1016/S09247963(00)00009-9

Rudels, B., Jones, E. P., Schauer, U., & Eriksson, P. (2004). Atlantic sources of the Arctic Ocean surface and halocline waters, Polar Res., 23, 181–208.

Rudels, B. (2009). Arctic Ocean Circulation. In Encyclopedia of Ocean Sciences (Second Edition, pp. 211–225). https://doi.org/ 10.1016/B978-012374473-9.00601-9

Rudels, B., Anderson, L., Eriksson, P., Fahrbach, E., Jokobsson, M., Jones, E. P. (2011). Observation in the Ocean. In P. Lemke, H.-W Jacobi (Eds.), Arctic Climate Change: The ACSYS decade and beyond (Ch. 4, pp. 117–198). Heidelberg: Springer.

Rudels, B. (2012). Arctic Ocean circulation and variability – advection and external forcing encounter constraints and local processes. Ocean Sci., 8, 261–286. https://doi.org/10.5194/os-9-147-2013

Rudels, B., Schauer, U., Björk, G., Korhonen, M., Pisarev, S., Rabe, B., & Wisotzki A. (2013). Observations of water masses and circulation with focus on the Eurasian Basin of the Arctic Ocean from the 1990s to the late 2000s. Ocean Sci., 9, 147–169. https://doi.org/https://doi.org/10.5194/os-9-147-2013

Ryan, W. B. F., Carbotte, S. M., Coplan, J., O'Hara, S., Melkonian, A., Arko, R., Weissel, R. A., et al. (2009). Global Multi-Resolution Topography (GMRT) synthesis data set, Geochem. Geophys. Geosyst., 10, Q03014, https://doi.org/10.1029/2008GC002332

Schauer, U., Muench, R. D., Rudels, B., & Timokhov, L. (1997). Impact of eastern Arctic shelf waters on the Nansen Basin in intermediate layers. J. Geophys. Res., 102, 3371–3382. https://doi.org/10.1029/96JC03366

Schauer, U., Rudels, Jones, E. P., Anderson, L. G., Muench, R. D., Björk, G., et al. (2002). Confluence and redistribution of Atlantic water in the Nansen, Amundsen and Makarov basins. Ann. Geophys., 20(2), 257–273.

Schauer, U., Fahrbach, E., Osterhus, S., & Rohardt, G. (2004). Arctic warming through the Fram Strait: Oceanic heat transport from 3 years of measurements. J. Geophys. Res., 109(C06026). https://doi.org/10.1029/ 2003JC001823

Schauer, U., & Beszczynska-Möller, A. (2009). Problems with estimation and interpretation of oceanic heat transport - conceptual remarks for the case of Fram Strait in the Arctic Ocean. Ocean Sci., 5, 487–494. https://doi.org/10.5194/os-5-487-2009

Schauer, U., & Losch, M. (2019). "Freshwater" in the Ocean is Not a Useful Parameter in Climate Research. J. Phys. Oceanogr. 49, 2309–2321. https://doi.org/10.1175/JPO-D-19-0102.1

Schlosser, P., Bauch, D., Fairbanks, R., & Bönisch, G. (1994). Arctic riverrunoff: Mean residence time on the shelves and in the halocline. Deep Sea Res., Part I, 41, 1053–1068. https://doi.org/10.1016/0967-0637(94)90018-3

Schlosser, P., Bonisch, G., Kromer, B., Loosli, H. H., Bühler, R., Bayer, R., Bonani,G., & Koltermann, K. P. (1995). Mid-1980s distribution of tritium, 3He, I4C and 39Ar in the Greenland/Norwegian Seas and the Nansen Basin of the Arctic Ocean. Prog. Oceanog., 35, 1–28.

Schlosser, P., Bayer, R., Bönisch, G., Cooper, L.W., Ekwurzel, B., Jenkins, W.J., S. Khatiwala, S., Pfirman, S., & Smethie Jr., W.M. (1999). Pathways and mean residence times of dissolved pollutants in the ocean derived from transient tracers and stable isotopes. Science of the Total Environment, 237/238, 15–30.

Schlosser, P., Newton, R., Ekwurzel, B., Fairbanks, R., & Mortlock, R. (2002). Decrease of river runoff in the upper waters of the Eurasian Basin,Arctic Ocean, between 1991 and 1996: Evidence from delta O-18 data. Geophys. Res. Lett., 29(15), Article 1289. https://doi.org/10.1029/2001GL013135

Serreze, M. C., Walsh, J. E., Chapin III, F. S., Osterkamp, T., Dyurgerov, M., Romanovsky, V., & al. (2000). Observational evidence of recent change in the northern high-latitude environment. Clim. Change, 46(159–207). https://doi.org/10.1023/A:1005504031923

Serreze, M. C., Maslanik, J. A., Scambos, T. A., Fetterer, F., Stroeve, J., Knowles, K., et al. (2003). A record minimum Arctic sea-ice extent and area in 2002. Geophys. Res. Lett., 30(3). https://doi.org/10.1029/2002GL016406

Serreze, M., and Francis, J. (2006). The Arctic amplification debate. Clim. Change, 76, 241–264. https://doi.org/10.1007/s10584-005-9017/y

Serreze, M. C., Barrett, A. P., Slater, A. G., Steele, M., Zhang, J., & Trenberth, K. E. (2007). The large-scale energy budget of the Arctic. J. Geophys. Res., 112. https://doi.org/10.1029/2006JD008230

Serreze, M. C., Holland, M. M., & Stroeve, J. (2007). Perspectives on the Arctic's shrinking sea-ice cover. Science, 315, 1533-1536.

Serreze, M. C., Barrett, A. P., Stroeve, J. C., Knidig, D. N., & Holland, M. M. (2009). The emergence of surface-based Arctic amplification. Cryosphere, 3, 11–19.

Serreze, M. C., & Barry, R. G. (2011). Processes and impacts of Arctic amplification: A research synthesis. Global Planet. Change, 77(1–2), 85–96.

Shimada, K., McLaughlin, F., Carmack, E., Proshutinsky, A., Nishino, S., & Itoh, M. (2004). Penetration of the 1990s warm temperature anomaly of Atlantic Water in the Canada Basin. Geophys. Res. Lett., 31(L20301). https://doi.org/10.1029/2004GL020860

Skagseth, Ø., Drinkwater, K. F., & Terrile E. (2011). Wind- and buoyancy-induced transport of the Norwegian Coastal Current in the Barents Sea. J. Geophys. Res., 116. https://doi.org/10.1029/2011JC006996

Smedsrud, L. H., Ingvaldsen, R., Nilsen, J. E. Ø., & Skagseth, Ø. (2010). Heat in the Barents Sea: transport, storage, and surface fluxes. Ocean Science, 6, 219–234.

Smethie Jr., W. M., Schlosser, P., & Bönisch, G. (2000). Renewal and circulation of intermediate waters in the Canadian Basin observed on the SCICEX 96 cruise. J. Geophys. Res., 105, 1105–1121.

Solomon, A., Heuzé, C., Rabe, B., Bacon, S., Bertino, L., Heimbach, P., Inoue, J., Iovino, D., Mottram, R., Zhang, X., Aksenov, Y., McAdam, R., Nguyen, A., Raj, R. P., & Tang, H. (2021). Freshwater in the Arctic Ocean 2010–2019. Ocean Sci. 17: 1081–1102. https://doi.org/10.5194/os-17-1081-2021

Spall, M. A. (2013). On the Circulation of Atlantic Water in the Arctic Ocean. J. Phys. Oceanogr., 43. https://doi.org/10.1175/JPO-D-13-079.1

Steele, M., Morison, J. H., & Curtin, T. (1995). Halocline water formation in the Barents Sea. J. Geophys. Res., 100, 881-894.

Steele, M., & Boyd, T. (1998). Retreat of the cold halocline layer in the Arctic Ocean. J. Geophys. Res., 103, 10,419–10,435.

Steele, M., Morison, J., Ermold, W., Rigor, I., Ortmeyer, M., & Shimada, K. (2004). Circulation of summer Pacific halocline water in the Arctic Ocean, J. Geophys. Res., 109, C02027, https://doi.org/10.1029/2003JC002009

Stigebrandt, A. (1984). The North Pacific: A global-scale estuary. J. Phys. Oceanogr., 14, 464–470.

Stroeve, J. C., Serreze, M. C., Holland, M. M., Kay, J. E., Masklanik, J., & Barrett, A. P. (2012). The Arctic's rapidly shrinking sea ice cover: A research synthesis. Clim. Change, 110, 1005–1027.

Stroeve, J. C., Markus, T., Boisvert, L., Miller, J. & Barrett, A. (2014). Changes in Arctic melt season and implications for sea ice loss. Geophys. Res. Lett., 41, 1216–1225.

Stroeve, J., & Notz, D. (2015). Insights on past and future sea-ice evolution from combining observations and models. Glob. Planet. Chang., 135, 119–132.

Swift, J. H., & Aagaard, K. (1981). Seasonal transitions and water mass formation in the Iceland and Greenland seas. Deep Sea Res., 28, 1107–1129.

Swift, J. H., Jones, E. P., Aagaard, K., Carmack, E. C., Hingston, M., MacDonald, R. W., F. A. McLaughlin, F. A., & Perkin, R. G. (1997). Waters of the Makarov and Canada basins. Deep Sea Res. Part II, 44(8), 1503–1529. https://doi.org/10.1016/S0967-0645(97)00055-6

Timmermans, M. L., Proshutinsky, A., Krishfield, R. A., Perovich, D. K., Richter-Menge, J. A., Stanton, T. P., & Toole, J. (2011). Surface freshening in the Arctic Ocean's Eurasian

Basin: An apparent consequence of recent change in the wind-driven circulation. J. Geophys. Res., 116.

Timmermans, M.-L., Proshutinsky, A., Golubeva, E., Jackson, J. M., Krishfield, R., McCall, M., & Platov, G. (2014). Mechanisms of Pacific summer water variability in the Arctic's central Canada Basin. Journal of Geophysical Research: Oceans, 119, 7523–7548. https://doi.org/10.1002/2014JC010273

Timofeyev, V. T. (1961). The movement of Atlantic Water and heat into the Arctic Basin. Okeanologia, 1, 407–411.

Toole, J. M., Timmermans, M.-L., Perovich, D. K., Krishfield, R. A., A. Proshutinsky, A., & J. A. Richter-Menge, J. A. (2010). Influences of the ocean surface mixed layer and thermohaline stratification on Arctic Sea ice in the central Canada Basin. J. Geophys. Res 115(C10), https://doi.org/10.1029/2009JC005660

Treguier, A. M., Deshayes, J., Le Sommer, J., Lique, C., Madec, G., Penduff, T., Molines, J.-M., Barnier, B., Bourdalle-Badie, R., & Talandier, C. (2014). Meridional transport of salt in the global ocean from an eddy-resolving model. Ocean Sci., 10, 243–255. https://doi.org/10.5194/os-10-243-2014

Wallace, D. W. R., Schlosser, P., Krysell, M., & Bönisch, G. (1992). Halocarbon ratio and tritium/3-He dating of water masses in the Nansen Basin, Arctic Ocean. Deep Sea Research Part A. Oceanographic Research Papers Part 1, 39(2), S435-S458. https://doi.org/10.1016/S0198-0149(06)80015-4

Whitefield, J., Winsor, P., McClelland, J., & Menemenlis, D. (2015). A new river discharge and river temperature climatology data set for the pan-Arctic region. Ocean Modelling, 88, 1–15, http://dx.doi.org/10.1016/j.ocemod.2014.12.012

Whitmore, L. M., Pasqualini, A., Newton, R., & Shiller, A. M. (2020). Gallium: A new tracer of Pacific water in the Arctic Ocean. Journal of Geophysical Research: Oceans, 125, e2019JC015842. https://doi.org/10.1029/2019JC015842

Wilson, C., & Wallace, D.W.R. (1990). Using the nutrient ratio NO/PO as a tracer of continental shelf water in the central Arctic Ocean. J. Geophys Res., 95, 193–203.

Woodgate, R. A., Aagaard, K., Muench, R. D., Gunn, J., Björk, G., Rudels, B., Roach, A. T, & Schauer, U. (2001). The Arctic Ocean Boundary Current along the Eurasian Slope and the adjacent Lomonosov Ridge: Water mass properties, transports, and transformations from moored instruments. Deep Sea Res. Part I, 48, 1757–1792. https://doi.org/10.1016/S0967-0637(00)00091-1

Woodgate, R. A., and K. Aagaard (2005). Revising the Bering Strait freshwater flux into the Arctic Ocean. Geophys. Res. Lett., 32 (L02602). https://doi.org/10.1029/. 2004GL021747

Woodgate, R. A., K. Aagaard, J. H. Swift, W. M. Smethie Jr., and K. K. Falkner (2007). Atlantic water circulation over the Mendeleev Ridge and Chukchi Borderland from thermohaline intrusions and water mass properties. J. Geophys. Res., 112 (C02005). https://doi.org/10.1029/2005JC003416

Woodgate, R. A., Weingartner, T. J., & Lindsay, R. (2012). Observed increases in Bering Strait oceanic fluxes from the Pacific to the Arctic from 2001 to 2011 and their impacts on the Arctic Ocean water column. Geophys. Res. Lett., 39. https://doi.org/10.1029/2012GL054092

Wust, G. (1935). Die Stratosphare des Atlantischen Ozeans. Deutsche Atlantische Exped. Meteor, 1925-1927. Wiss. Erg., Bd. VI, 1. Teil, 2. Lief., 288 pp.

Yang, J. (2005). The Arctic and Subarctic ocean flux of potential vorticity and the Arctic Ocean circulation. J. Phys. Oceanogr., 35, 2387–2407. https://doi.org/10.1175/JPO2819.1

Zhang, J., & Steele, M. (2007). Effect of vertical mixing on the Atlantic Water layer circulation in the Arctic Ocean. J. Geophys. Res., 112. https://doi.org/10.1029/2006JC003732

Zhang, X. H., J. Zhang, J., & Wu, P. (2013). Enhanced poleward moisture transport and amplified northern high latitude wetting trend. Nature Climate Change 3(1), 47-51. https://doi.org/10.1038/nclimate1631